Electronic Thesis and Dissertation Repository

7-15-2020 10:15 AM

Optimization of Indentation for the Material Characterization of Soft PVA-Cryogels

Md. Mansur ul Mulk, *The University of Western Ontario*

Follow this and additional works at: https://ir.lib.uwo.ca/etd

Part of the Biomechanics and Biotransport Commons

Abstract

Over the past few years, a variety of clinical procedures aiming at tissue repair and other relevant therapies have been under active investigation [1]. Success of procedures aimed at soft tissue repair depends on the combined response of biochemical and biomechanical properties of organs neighboring the tissue [2]. Using human or animal cadaveric tissue for this purpose is very challenging due to issues pertaining to biodegradability and infection or biohazard risk factors [3, 4]. As such, tissue mimicking materials (e.g. polyvinyl alcohol cryogel (PVA-C) have been investigated to satisfy the need for the said clinical applications. Advantages of using tissue-mimicking materials include (a) biocompatibility, (b) being not biodegradable and preserving shape in long-term and (c) having similar biomechanical properties to human tissue [5, 6].

To assess biomechanical compatibility of tissue-mimicking materials, various mechanical testing techniques have been proposed. Among them, indentation testing has shown great potential for this purpose, and it has been used broadly for tissue biomechanical characterization [7]. This method has become more popular because it allows for cost effective, non-destructive, quick, and quantitative assessment of soft tissue biomechanics [8, 9]. Soft tissue is idealized as nonlinear [10], isotropic [11] and incompressible [12] material. Given its interesting properties and biocompatibility, PVA-C has attracted a great deal of attention as a biocompatible material suitable for clinical applications such as tissue repair, tissue engineering etc. As such, many studies have been conducted to understand this material's mechanical properties and its suitability for fabricating artificial cornea replacement [5], heart valve [13], lung [14], breast [15], kidney [16], brain [17], bladder [18], prostate [19] and articular cartilage [20]. This stems from the material having similar characteristics to human soft tissue [21, 22].

Similar to biological tissues, the internal structure of PVA-C leads to nonlinear behavior [23, 24]. This nonlinearity becomes predominant while it undergoes large deformation [25]. Several analytical, semi-analytical and computational models have been proposed to understand tissue mechanical behavior, including its linear and nonlinear behavior, under indentation tests [26]. These include the methods proposed by Boussinesq [27], Sneddon [28], Hayes [29] and Cao [30]. This thesis aims at gaining in-depth insight into the mechanical behavior of PVA-C

specimens under indentation testing. To this end, it presents development of an inverse finite element (FE) technique solved using numerical optimization to characterize the mechanical properties of PVA-C specimens. The investigation reported in this thesis includes numerical analysis where displacement influence factor was employed in conjunction with linear elastic model of finite thickness. In the analysis, effects of Poisson's ratio, specimen aspect ratio and relative indentation depth were investigated, and a novel mathematical term was introduced to Sneddon's equation. Finally, a robust optimization algorithm was developed in MATLAB which utilized FE modeling for parameter estimation before it was rigorously validated.

Summary for Lay Audience

A variety of clinical procedures for assessing structural and functional damage of tissues and treating the effectiveness of tissue therapeutics are under active investigation. Therapeutics of soft tissues depends on the mechanical response of the organs and neighboring tissues. Indentation techniques can be used to probe the local mechanical properties of soft tissues and tissue mimics. Although there are some distinct advantages of using indentation testing, the interpretation of the force-displacement behavior of very soft materials is less straight-forwards. Non-linear, hyper-elastic models have been used previously to characterize sources of non-linearities (ie. material and geometrical) in this type of problem but have presented some problems. Indentation responses from cylindrical indenters are investigated in this study using numerical methods to develop and optimize new techniques for characterizing nonlinear material properties using an Ogden and Mooney Rivlin hyper-elastic models.

Acknowledgments

Dedications

To my Parents

Habibur Rahman and Monowara Begum

Statement of Originality

I hereby certify that, to the best of my knowledge, studies and tests used in this thesis were not performed by any other researcher and the results have not been published or submitted for publication. I declare that this thesis has not been previously submitted for a degree or diploma at any other higher education institution.

Table of Contents

List of Figures

List of Tables

Nomenclature

Acronyms

a	Indenter radius
B	Width of the specimen
C	Right Cauchy-Green deformation tensor
E	Young's Modulus
F	Global load vector
F	Deformation gradient Tensor
G	Bulk modulus
h	Soft tissue thickness
J	Jacobian
K	Global stiffness matrix
k	Non dimensional parameter
L	Axial length
M	Material matrix
$O(\boldsymbol{P})$	Object function
P	Concentrated force
$\boldsymbol{r}$	Residual vector
R	Radius of the spherical indenter
$\mathbb{R}$	Real numbers
S	Second Piola-Kiechhoff Stress tensor
t	Current time

Acronyms

U	Displacement vector
W	Strain energy function
w	Penetration depth
X	Initial position
x	Coordinate for arbitrary point
Y	Displaced position
Ω	Friction Coefficient
Φ	Relative indentation Depth
Ψ	Aspect ratio
Ξ	Natural co-ordinates
α	Strain hardening coefficient
μ	Shear modulus
λ	Lame´ constant
υ	Poisson's Ratio
$\Lambda \ \& \ \tau$	Data value
χ	Function of deformation
ξ	Natural coordinates

Superscripts

$\delta^e \vartheta$ Arbitrary virtual velocities

F^T Transpose of deformation gradient vector

Symbols with Subscripts

$\lambda_1, \lambda_2, \lambda_3$ Principle strains

σ_{ij} Stress tensor

ε_{ij} Strain tensor

B_{ij} Left Cauchy deformation tensor

C_{10}, C_{01} Temperature dependent material parameter

C_{ijkl} Tensor of elastic constant

C_{ij} Right Cauchy deformation tensor

D_i Material constant

I_1, I_2, I_3 Invariant of Cauchy Green deformation tensor

t_0 Initial time

t_n Time step

$X_a t$ Motion of the body

P_0 Initial pressure

Chapter 1

Introduction

Indentation testing is a widely used method to characterize diverse mechanical properties, e.g. stiffness, plastic deformation and hardness. This technique is applied to a wide range of material types, such as natural biological tissues, plastics, wood, metals, and food [40]. It is predominantly used for the determination of the strength of the materials [41]. Many previous researchers have used analytical models to understand indentation mechanics, including the effect of indenter geometry on the indentation process [4]. The geometries investigated include cylindrical, spherical, and conical indenters that are applicable to these common tests.

Flat-ended cylindrical indentation is one of the most popular techniques used to assess the mechanical response of materials [25, 29]. For cylindrical indentation, the contact region between the indenter and test sample is fixed. The contact pressure increases linearly upon activating the concentrated indentation load [40].

Spherical indenters can be used to investigate the limit of the elastic stress in brittle materials [42]. The main advantage of using a spherical indenter is that it does not create any stress singularity. The contact radius of the spherical indenter increases proportionately with the indentation load. During the indentation process, the contact stresses are initially small and produce only elastic deformation [19]. As the depth of penetration increases, a conical crack can occur in brittle materials outside the contact area [19, 31]. Interpreting the interaction problem of such non-conforming elastic bodies requires fundamental understanding of the

1

contact. Such contact problems can be categorized using (i) the shape of the indenter: circular, flat or curved, (ii) the type of indentation: rotation or translation about one or other axis (iii) the type of contact: friction or frictionless [43]. Load-depth relationship for axisymmetric punch has been the subject of numerous investigations previously. Elastic analysis of contact problems of two spherical bodies was first developed by Hertz [44] as the basis for his indentation technique for material characterization [31, 45]. In 1904 Huber provided analytical solutions for the stress field associated with indentation of a flat surface with a spherical indenter [46]. In 1913 Fischer [47] and in 1914 Huber and Fuchs [46] also provided analytical solutions pertaining to contact mechanics.

An elastic half-space is a mathematical concept in which only one boundary exists, all others being infinitely far away. For elastic materials, Boussinesq established other theoretical solutions for elastic half-spaces, known as Boussinesq's solutions. A classic point-load analysis for pressure distribution of an elastic half-space acting on a closed surface was described by Boussinesq [27]. He used the potential theory method to solve the computational problem and therefore was unable to use this solution for practical interest [27, 40]. The solutions for stresses and deformations in an elastic half-space was partially resolved by Carothers and Love [40, 48], but their solution was only valid for cylindrical and conical indenters.

To find a complete solution of Boussinesq's problem, in 1945, Harding and Sneddon used Hankel transformations of dual integral equations to reduce this problem [43]. In 1962, Ahlvin and Ulery solved Love's equations and presented influence value and tables of coefficients. Using the equation together with the coefficients from the tables shown in Appendix, stresses and deformations can be calculated [27, 37, 49, 50]. In 1946, Sneddon developed the integral transform method for a variety of indenters [49] and derived load-displacement relations for an axisymmetric cylindrical punch [49]. In 1958, Lebedev and Ufland studied the axisymmetric contact problem for an elastic layer on a rigid smooth base [29, 51]. The vertical compressive stress σ_z at any depth directly beneath the centerline of a circular area can also be obtained by integrating Boussinesq's equation, where, a is the radius of the loaded area:

$$\sigma_z = P \left[1 - \left(\frac{1}{1 + (\frac{a}{w})^2} \right)^{3/2} \right]$$

(1.1)

The equations for vertical deformation at any point of interest underneath the indenter surface can be calculated using Boussinesq's equation. The vertical deformation for the case of a uniform pressure p, influence factor, I_F applied over a circular area of radius a, is given by:

$$\Delta_Z = Pa\frac{2(1-\upsilon^2)}{E}I_F$$

(1.2)

The influence factor equals 1.00 beneath the center of the plate and 0.637 beneath the edge. The table of the influence factor is provided by Ahlvin and Ulery [37] as given in the Appendix.

In 1965, Sneddon introduced the integral transform method to obtain an analytical solution for an elastic half-space. He used cylindrical, spherical, parabolic and conical punches to conduct indentation tests, to obtain the relationship between the load and penetration depth [28, 52]. After an extensive mathematical treatment provided by Gladwell [43], Jonson introduced practical application-oriented stress field analysis [53]. Due to lack of appropriate constitutive models, computational accuracy from indentation responses for soft tissues have been constrained. In 1968, Burstein and his co-workers conducted spherical and cylindrical indentation under three-layered geometry and calculated stress distribution and displacements [54].

Previous studies reported that a frictionless punch causes two types of problem: (i) pressure caused by the complete contact between indenter and the specimen generates an algebraic singularity at the contact boundary and (ii) incomplete contact of the contact region causes a reduction of zero pressure at the contact boundary for spherical punch [32]. Hayes and his co-workers investigated an indentation of an infinite thick elastic layer bonded to a rigid half space [29]. They considered this case as a mixed boundary value problem and calculated displacements, shear modulus and friction [29]. Mesarovic and his co-workers reported that friction between the indenter and specimen has a significant effect on the contact size of the

indenter and is a function of indentation depth. They also stated that the friction coefficient strongly affects the strain field beneath the indenter [55].

The indentation of plastic materials has also been reported by many researchers for the determination of plasticity properties, yield strength and strain hardening [40, 56]. These properties can be obtained from force-deformation curves measured during indentation [57]. Badrick and his co-workers reported that the nature of the elastic-plastic material properties in solids de- pends both on the material and the type of indenter used during indentation [58]. In common with elastic materials, to test the robustness of the elasto-plastic properties, different geometries of indenters have been used such as cylindrical, spherical, conical, and uniaxial [57].

1.2 Soft Tissue and Artificial Materials

Biological soft tissue is a complex material composed of elastin, actin, resilin, abductin and collagen [36]. However, elastin and collagen are the most important structural components of biological soft tissues [36]. Soft biological tissues are often inhomogeneous, anisotropic and can be subjected to large deformations [30]. Many previous researchers have found that the mechanical properties of soft tissues can be highly nonlinear [11]. Hence, soft tissues can exhibit widely different stiffness under different physiological conditions.

The mechanical properties of soft tissues also vary depending on whether the measurement condition is *in vivo* or *in vitro* [29]. Due to this stiffness variation, it can be challenging to obtain the biomechanical properties of soft tissue [59]. To characterize the mechanical properties of soft biological tissues through standard compression or tensile test a significant problem arises. This is due to specimen geometrical irregularities and difficulties in cutting intact and appropriately sized test samples [60].

There are a number of nonlinearities that can have a significant impact on the deformation of soft tissues (i) nonlinear elasticity of the solid phase (ii) geometrical nonlinearity arising from finite deformation, and (iii) nonlinear material parameters such as permeability, and porosity [60–62]. Working with biological tissue in the engineering domain is very difficult. Firstly,

availability of human organ requires many protocols to fulfill [63]. Secondly, biological organ degenerates rapidly. Without personal protective equipment and maintaining occupational hygiene the risk of infections may increase. PVA hydrogel can be used in biomedical applications as it exhibits excellent biocompatibility and has similar mechanical properties as soft tissues [5].

From material characterization to surgical training, tissue-mimicking materials are widely reported to be an important tool in biomedical applications. These materials have been used for the development and performance testing of many diagnostic techniques [34, 64], material characterization through different indentation techniques [39], numerical modeling and validation exercises.

The mechanical properties of soft biological tissues and hydro-gels such as polyvinyl alcohol cryogel (PVA-C) [5, 6, 34], PVA hydrogel [65], polydimethylsiloxane (PDMS) [6], Bovine gelatin (BoGe10), porcine gelatin (PoGe-10X) [26], PEG hydrogel materials synthesized from polyethylene glycol, di-methacrylate (PEGDMA) and monomer [66], have been studied by many researchers using various test methods and established procedures for usage in biomedicine [67].

Polyvinyl alcohol (PVA) hydrogel is a promising biomaterial, which is a hydrophilic, biodegradable and biocompatible synthetic polymer appropriate as a tissue-mimicking construct. This material has been widely used already in biomedical applications [65]. The formation of PVA is through the combination of an appropriate ratio of PVA and water, which is then treated in various ways to create cross-linkage between the polymer filaments [65].

The mechanical properties of hydrogels are particularly well controlled by a freezing and a thawing process creating what is known as PVA-C (PVA cryogel) [13, 65]. This is due to the fact that PVA hydrogels have similarities with human soft tissue structure [10, 21, 22]. When a load is suddenly applied to a PVA-C hydrogel, free water inside the pores of the sample is unable to migrate immediately, this results in the volume of the hydrogel to remain essentially conserved and the Poisson's ratio to stay close to 0.5 [68]. This number has been found to be related to materials visco and poroelastic characteristics. The physical properties of PVA-C are very similar to those of a wide range of biological tissues [4, 69]. Many previous researchers

reported that, PVA hydrogels have a wide range of applications in tissue engineering [65, 70] including cornea [71], heart valve [13], lung [14], breast [15], kidney [16], brain [17], stomach [72], bladder [18], prostate [19] and articular cartilage [20].

Many previous researchers have reported difficulties involved in conducting in "vivo" measurements due to (i) setting proper instrument alignment on sizable specimens, (ii) fixing boundary conditions, (iii) small deformation, (iv) limited data sets, (v) complexities from physiological noise, and (vi) inability to control the internal condition of the organs makes it difficult to interpret the data. [59, 63, 82]. To avoid the complexity involved in in" vivo" measurement and the risk of using human organs in the engineering environment, material characterization of human tissue mimic through indentation experiment is essential [29, 39]. In order to overcome all the complexities listed above, there is an urgent requirement for the development of a new method including the use of PVA-C data set that can be used to evaluate non-linear soft materials.

1.3 Material Models

Many previous researchers reported that nonlinear materials undergo large deformation [83] that requires constitutive models and iterative solver such as Newton-Raphson or Quasi-Newton for the convergence of the numerical solution [29, 30]. For the robustness of the nonlinear solution, solution convergence is achieved through mesh refinement. Biological soft tissues and artificial materials are the present challenges that needs to be characterized and accurately interpreted through numerical validation and optimization for future biomedical applications.

1.3.1 Linear and Nonlinear Elasticity

Linear elasticity (LE) is a mathematical concept characterizing linearly Proportional deformation of materials due to external loading conditions. The constitutive law for LE related to applied force and resulting deformation is known as Hooke's Law, where, tensile stress σ is linearly proportional to its fractional axial deformation or strain ε by the modulus of elasticity E:

$$\sigma = E\varepsilon \tag{1.3}$$

Some materials including biological tissues, do not obey Hook's law as they exhibit nonlinear behavior specially under loading causing large deformation. In such materials, mathematical models need to be considered that incorporate sources of nonlinearity into the mechanical behavior. Nonlinearities can be explained in two ways. First, type of nonlinearity called geometric nonlinearity caused by significant change in the geometry. As a result of this change in geometry, forces are redistributed leading to alteration in the force equilibrium equations. The second type of nonlinearity is called intrinsic nonlinearity, which is a manifestation of changes in the internal structure of the material [84]. A typical indentation load-displacement relationship for non-linear elastic and linear elastic model are shown in Figure: 1.1 and Figure: 1.2.
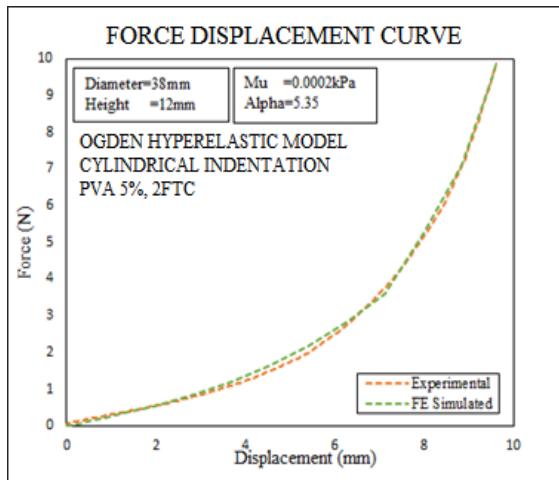
Figure 1.1: Nonlinear force displace relationship of an indentation test plotted using experimental and simulated data of PVA-C 5%, 2FTC.
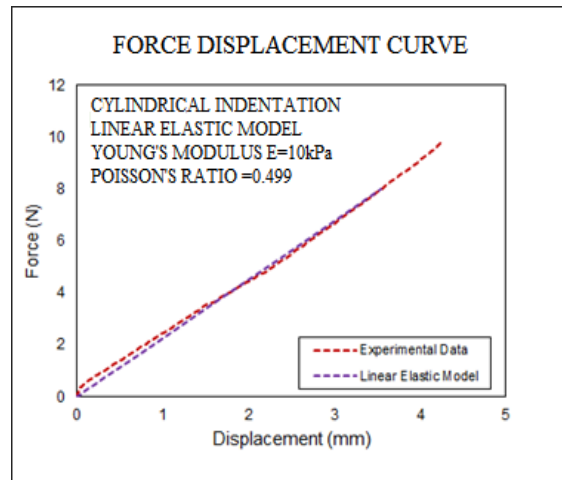
Figure 1.2: Linear force displacement relationship of indentation test plotted using experimental and simulated data PVA-C 5%, 2FTC.

Many mathematical models have been developed [27, 28] to characterize soft tissues. Unfortunately, it is not possible to describe the mathematical model for nonlinear soft biological tissue without numerical verification [89]. Indentation is not only used for characterizing solids [40] but also employed as an ideal candidate for investigating various biological tissues [96, 97]. The effect of various parameters, including relative indentation

depth, aspect ratio, Poisson's ratio and dimensionless parameter (k) on the indentation response of soft tissues needs to be investigated.

1.3.2   Hyperelastic Models

A hyperelastic or Green type elastic material [85] is a type of material that follows constitutive models where the stress-strain behavior is defined by a strain energy density function [86]. They are considered to be truly elastic as they store energy during loading and dissipate equal amounts of energy during the unloading process. These materials experience large strains which are mostly recoverable [87, 88]. To define hyperelasticity many mathematical models have been developed and different aspects of non-linear elastic material behavior explained [11, 89]. These types of model have been very successfully applied to soft materials and tissues.

In 1948 Ronald Rivlin and Melvin Mooney introduced the first hyper-elastic relationship named the" Neo-Hookean" and" Mooney-Rivlin" model. To date, a number of other hyper-elastic models have been developed. Based on observed mechanical responses of tissue behavior among others, Ogden shows improved behavior [90].

A considerable amount of work has been carried out using finite element method (FEM) to investigate the linear and nonlinear behavior of soft tissues. In recent years, characterizing hyperelastic material properties of soft tissues using indentation tests has attracted considerable attention. For the development and characterization of soft tissue with the inverse analysis, optimization algorithm plays an important role in developing a physical model for biomedical application [93].

Many previous researchers have reported on the accuracy of the extracted hyperelastic parameters from indentation data [95]. Instead of extracting unknown material properties Namani and Simha extracted elastic modulus from the indentation [31, 95]. Despite of all the development in this domain, still there is no gold standard for characterizing the material properties of soft tissues. Therefore, there is an urgent need for inverse analysis to extract the hyperelastic material properties of soft tissues from in dentation responses.

Inverse analysis is used to extract unknown material properties. But there is no straight forward method to extract material properties from experimental data. To overcome this issue, we introduced a technique that requires no external data to validate the extracted parameter. The technique utilizes the Ogden and Mooney-Rivlin hyperelastic model, where Ogden and Mooney-Rivlin parameters are determined using an inverse problem framework.

The motivation of this dissertation work is to provide more detailed understanding of indentation testing of soft tissues and to develop methods for interpretation of the results of this test for biomedical application. The specific objectives are stated below:

1.4 Objectives

1. To investigate the mechanical properties of finite and infinite thickness soft tissue samples in a simulated environment and compare the results with analytical and numerical published results.

2. To improve understanding of the contribution of interface friction, Poisson's ratio and elastic stiffness on the observed load-deformation indentation response of a soft tissue for linear and non-linear behavior.

3. To develop a novel analytical model for nonlinear elastic solution to investigate the effect of friction coefficient, Poisson's ratio and thickness on geometric parameters such as relative indention depth and aspect ratios.

4. To develop and optimize new methods of determining the non-linear material parameters of an Ogden and Mooney-Rivlin hyper-elastic model capable of describing a variety of PVA-C material.

1.5 Methods

The calibration and validation of the numerical approaches in this study have been accomplished using a robust dataset of experimental stress-strain tests on PVA cryogel conducted by Zakeri [61]. The finite element method has been used successfully to model biomechanical problems previously, and it is used in this study to simulate the indentation tests in soft materials. To achieve the above-mentioned objectives, the following methods have been undertaken:

1. The experimental force-displacement results for PVA-C 5%, 10%, 15% and 20%   (w/w) obtained from indentation test [98] have been compared with analytical and simulated results [25, 29, 30].

2.   An axisymmetric indentation model was developed with the finite element method (Abaqus). Materials with finite and infinite thickness were considered in the simulation. A rigid, flat ended, cylindrical indenter modeled. Simulated displacement values were compared with Hayes', Zhang's and Cao's models [25, 30].

3. A novel analytical solution was developed by modifying Zhang's solution. The simulated results were used in the newly developed analytical solution. The novel solution provided a new way of understanding the thickness effect of soft biological tissues.

4. An axisymmetric finite element model was developed to calculate the influence factor; This factor is used to calculate stress at any point under the indenter using the linear elastic model.

5. An optimization algorithm was used in conjunction with MATLAB for obtaining un- known hyperelastic parameters based on minimizing the discrepancy between experimental and model predicted results. Unknown parameters for the constitutive models were determined. And sensitivity analysis was performed to validate the accuracy of the experimental data.

1.6   Novelty of the Current Research

The novelty of the current research is the numerical material model developed to characterize the biomechanical properties of soft tissue and mimics. It was found that the results obtained from this numerical model performed well with a novel analytical model developed by modifying Zhang's model [25]. Also, an optimization algorithm was developed in MATLAB in conjunction with FEA for error minimization and parameter estimation, which verifies and validates experimental hyperelastic results.

1.7   Contribution to the Knowledge

The research provides:

1. A literature review that can benefit research in the indentation and soft tissue mechanics field. Valuable information is presented and discussed.

2. Investigation of the fundamentals of indentation experiment on tissue-mimicking phantoms. Experimental results provide an important insight into the possibility of developing artificial organs based on material thickness and biomechanical properties.

3. Explanations of displacement influence factor on linear elastic model based on conducted numerical analysis on finite thickness structures. This new technique is suitable for thin samples.

4. Discussion of the impact of axisymmetric cylindrical, spherical indentation and uniaxial test on hyperelastic model.

5. Introduction of the newly developed analytical solution can potentially provide a new way of understanding the indentation response of soft tissues.

6. Improved inverse algorithm for Ogden and Mooney-Rivlin hyperelastic model using MATLAB which also compares FE predicted material properties with MATLAB optimized results. This robust technique is very effective for the determination of material properties of soft tissues or mimics. This novel technique is a potential candidate for use in the development of patient specific artificial organs.

1.8   Scope of the Study

The objectives of this research were to characterizes the material properties of polyvinyl alcohol cryogel (PVA-C) through indentation testing. In order to achieve that goal, three approaches were combined and used in this dissertation.

First, the indentation test responses from a range of PVA-C samples were simulated and results were compared with analytical solutions and numerical results available in the literature. These results confirmed the accuracy of the test material based on comparison of experimental and FE simulated force- displacement data.

Secondly, I developed an axisymmetric indentation model for cylindrical, spherical and uniaxial testing to investigate the mechanical responses of PVA-C. Models were meshed using proper finite elements before loading and boundary conditions were applied. Mesh convergence analysis was also performed to ensure numerical accuracy. A friction coefficient was introduced to an analytical solution introduced in the literature and its impact on observed indentation responses of PVA-C were evaluated.

Furthermore, a robust optimization algorithm was employed using Ogden and Mooney-Rivlin models for determining the non-linear material properties that minimized a cost function representing the difference between experimental and model predicted results.

Finally, the optimized material properties obtained using the present robust technique were cross validated with published results. This technique can be effectively used to characterize material properties where optimized materials can be considered as candidates for various biomedical applications.

1.9 Outline of the Dissertation

This thesis contains six chapters. All the chapters are written in the form of monograph.

Chapter 1: Introduction

Introduces the research topic, objectives, methods and scope of the research. It also states the contributions of the research to indentation experiment using finite element model and its application.

Chapter 2: Literature Review

Presents literature review, discusses Hertz, Sneddon, Cao's model, strain-strain theory for linear elastic model. Due to the soft tissues load bearing capacity of soft tissue, indentation of biological tissues is quite different than engineering materials. Non-linearity is a major consideration for materials undergoing large deformation This chapter discussed nonlinear elasticity for hyperelastic material. It also discusses the effect of influence factor, friction and frictionless contact region for non-linear material in the simulated environment with a rigid cylindrical indenter.

Chapter 3: Development and Validation of Numerical Model

This chapter describes the development and verification of finite element modeling of soft tissues. This chapter also discusses contact interaction, choice of element, methods of load applied, coefficient of friction and indenter size effect. A numerical model is verified and validated by Hertz, Boussinesq's and Sneddon's solutions as a proof of the principle. This chapter also incorporates constitutive relations from the above-mentioned models into numerical analysis for stress distribution of soft tissues.

Chapter 4: Characterization of PVA-C Material Behavior using FEM

This chapter discusses the indentation responses of non-linear transversely isotropic materials and presents a numerical analysis with FEM for soft tissue specimen with finite and infinite thickness. It examines the uniqueness of Sneddon's, Cao's, Zhang's models and presents FE simulated results through comparison with their published results. It also Investigates the association between relative indentation depth and aspect ratio. It further analyzes dimensionless functional "k" values from indentation force-depth curves that have sufficient influence on the friction and frictionless environment. Moreover, it employs displacement influence factor on linear elastic model and conducted numerical analysis on finite thin structures. It also introduces a newly developed novel analytical technique for linear elastic materials validated by numerical analysis and laboratory provided data. This chapter is concluded by presenting the effect of Poisson's ratio, aspect ratio and relative indentation depth on friction coefficient with a short summary.

Chapter 5: Soft Tissue Mechanical Characterization Using Finite Element

This chapter presents a hyperelastic model to conduct inverse analysis for the extraction of unknown material parameters. Experimental load displacement data is used as an input parameter for the hyperelastic model. During the parameter estimation process the simulated data is compared with the experimental deformation data. The sum of the squared differences between the two sets of data used to find an optimal set of material parameters. A trust region algorithm is used in MATLAB to extract optimized parameters from a set of guess values. A stability analysis is also presented by adding different noise levels to the input data to examine the robustness of the estimated parameter.

Chapter 6: Contribution and Conclusion

Presents a general discussion and concluding remarks.

Chapter 2

Literature Review

Understanding and measurement of the mechanical properties of soft tissues or tissue mimics is necessary for the development and improvement of medical devices. Conventional testing methods includes tensile, compressive and shear loading. While effective for materials that can be cut into reasonably large samples with regular geometry, conventional methods cannot be used with small specimens with irregular geometry (e.g. tissue excised surgically as a part of medical intervention procedures). In the latter case, indentation testing can be used as an effective technique for characterizing the mechanical properties. This mechanical testing method is similar to indentation hardness tests [99].

Indentation testing can offer accurate, nondestructive measurements of penetration depth from nanometer to macro-meter scale. Previously, numerous published literatures have discussed indentation testing methods on biological soft tissues and tissue mimics. However, influence of relative indentation depth, specimen aspect ratio, Poisson's ratio and friction coefficient in the mechanical response and how those parameters need to be incorporated in estimating tissue properties is not well understood.

Interpretation of experimental results from indentation based on empirical or semi-empirical formulas can be challenging [99]. Due to the complexity of using biological soft tissues in the engineering domain and to interpret mechanical testing results accurately, finite element method has been introduced for analysis of experimental data taking into account the simulated

Chapter 3: Development and Validation of Numerical Model

environment. Non-linear materials cannot be explained by the linear theory of elasticity where (Hooke's law) is applicable. For this reason, many articles have been reviewed to under- stand how experimental indentation testing of nonlinear materials is simulated using continuum mechanics [99]. To characterize material properties accurately choosing the appropriate model is essential. After an extensive review, it can be concluded that Ogden hyperelastic model is the best fit for nonlinear biological soft tissues or tissue mimics [26, 100]. This review aims at better understand of indentation testing used for characterization of soft tissues forwards biomedical applications. In this chapter an extensive literature review related to the current study will be presented.

2.1   Indentation Testing

2.2.1 General

For over a century, indentation tests have been a common practice for the characterization of materials in many areas of engineering. Nowadays, biomedical engineering and health-care industries has benefited greatly from the vast applications of indentation technology. Indentation testing is a widely used procedure to characterize diverse mechanical properties, e.g. stiffness, plastic deformation and hardness for a range of material, such as natural and artificial tissues, steels and food [101]. It is also a quantitative method used to determine the strength of the materials [102, 103].

There are various indentation test methods such as Hertzian, Vickers, Rockwell and Brinell that have been routinely used to measure material properties including elastic modulus and hardness using various standard indenter geometries such as cylindrical, spherical, conical and pyramid [30, 101, 104–106]. There are two ways of predicting the uniaxial mechanical properties of material in FEM, these include (i) load control where indenter is pushed into the test specimen at a constant rate and (ii) displacement control where an indenter is allowed to

Chapter 3: Development and Validation of Numerical Model

move into the test specimen under some constant force [24]. In conjunction with these tests, instruments have developed to obtain force displacement measurements instantaneously [104].

2.1.2   Hertzian Model for Elastic Contact

Indentation on an elastic body is one of the problems of contact mechanics [107]. Linear small strain theory of elasticity is used for non-conforming elastic bodies whose dimensions are small compared to the radius of curvature of the deformed surface [108]. Near the contact region the contact stresses are highly concentrated, and the stresses decrease rapidly from the contact point towards the distance it travels. The stress can be calculated as a semi-infinite solid, bounded by a plane surface know as elastic-half space [31].

Interpreting indentation testing of two non-conforming elastic bodies requires fundamental understanding of the contact problem which was first developed and introduced by Hertz [40]. Such contact problems can be categorized by (i) type of the punch: circular, flat or curved, (ii)   type of the indentation: rotation or translation about one or other of the axis, and (iii) type of contact: frictionless complete or incomplete contact, adhesive or in limiting friction [43]. Gladwell reported that the mathematical tool of, Hankel transforms of the, dual integral equation can be used to solve these contact problems [43].

In the early 1880, Hertz introduced "theory of elastic deformation" that works with the geometrical effects on local elastic deformation properties in contact mechanics. In 1882, Hertz introduced a solution to the elastic contact problem for a flat-ended cylindrical punch and elastic half space made of a homogeneous, isotropic, linearly elastic material. A rigid sphere in contact with an elastic half-space shown in Figure: 2.1

Chapter 3: Development and Validation of Numerical Model
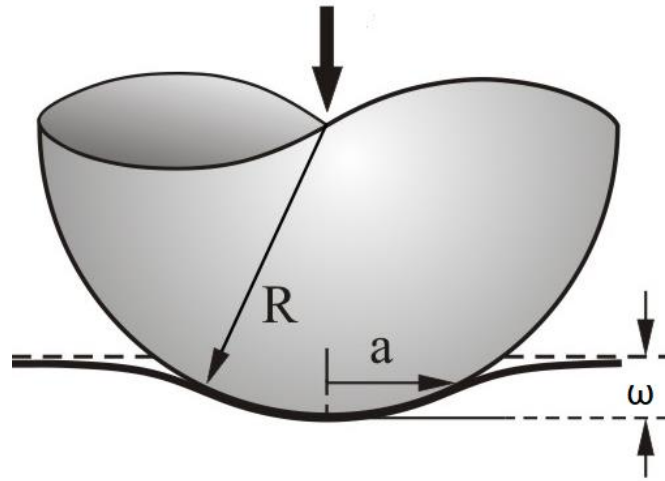
Figure 2.1: A rigid sphere in contact with an elastic half space modified from [31].

He made the following assumptions:

1. Strains are small, and within elastic limit a ≤ R.
2. The surfaces are continuous and non-conforming: a ≤ R.
3. Each solid can be considered as an elastic half space a ≤ R.
4. The surface is frictionless.

The distribution of pressure P, P_0, contact radius "a" and $\mathbf{U_z}$, vertical displacement proposed by Hertz are given by:

$$P = P_0[1-(r/a)^2]^{1/2} \tag{2.1}$$

$$\mathbf{U_z} = \left(\frac{1-\gamma^2}{E}\right)\pi P_0 \ (2a^2 - r^2), r \leq a \tag{2.2}$$

Based on Hertz's theory, flat surface indentation responses from spherical indenter produces compressive stress underneath the indenter and tensile stress at the edge of the contact circle

Chapter 3: Development and Validation of Numerical Model

that creates cone-shaped, fractures [31, 45, 109]. The maximum tensile stress of the material at the contact circle is given by:

$$\sigma_y = (1 - 2v) \frac{P}{2\pi a^2} \qquad (2.3)$$

Where, a is the contact radius, P is the normal load and v is the Poisson's ratio of the specimen. Many previous researchers have used analytical models to understand the effect of indenter geometry on indentation [25]. Typical geometries include cylindrical, spherical and conical indenters. Spherical and cylindrical indentation have been discussed below:

2.2 Boussinesq's Solution

In 1885, Boussinesq first considered "The problem of determining the distribution of stress within an elastic half space when it is deformed by normal pressure against its boundary of a rigid punch" [27, 28]. This problem is known as Boussinesq's problem discussed in Chapter 1.

2.3 Sneddon's Solution

The Boussinesq limitation for the arbitrary shaped axisymmetric punch was resolved by Sneddon analytically. A solution was derived from the top of the flat-ended cylindrical punch where the total load is applied to achieve displacement [28, 40, 110]. In 1929, Love [110] used constant pressure, constant displacement and Hertzian pressure to solve Boussinesq's problem. Due to the complexity of potential theory method, Boussinesq's solution was difficult to implement for the problem of interest, hence it was partially solved by Love [40] for cylindrical and conical indenters. To reduce the mixed boundary problem of Boussinesq's solution, Sneddon uses the theory of Hankel transforms to define the axisymmetric solution of the

Chapter 3: Development and Validation of Numerical Model

equation of elastic equilibrium [28]. He introduced cylindrical coordinates at the tip of the punch, and the solution is suitable for frictionless cylindrical, spherical or conical indentation on an elastic-half space [28, 49]. The relationship between load and deformation for an axisymmetric punch has been subject to numerous investigations [43].

2.3.1   Cylindrical Indentation

Cylindrical indentation offers an attractive candidate for investigating material properties. For cylindrical indentation, the contact region between the indenter and test sample is fixed. Contact pressure linearly increases upon applying concentrated indentation load [40].

Consider a flat-ended cylindrical profile of radius a indented on an elastic solid of thickness h. A concentrated force P is applied through the top of the indenter and creates a deformation D. Where μ and ν are the shear modulus and the Poisson's ratio of the material. Cylindrical polar coordinates (r, θ, z) are used where the indenter axis coincides with the z-axis, r is perpendicular to z, and θ represents the angular distance between a reference line and r.

The analysis is carried out without the influence of any friction on elastic half space [28, 40]. The analytical solutions are derived by using the resources of [28, 29, 52]. A new function f defined to solve Boussinesq's problem by the systemic use of Hankel transform and the theory of dual integral equation, then using Sneddon's formula for total depth of penetration:

$$w = \int_0^1 \frac{(x)dx}{\sqrt{1-x^2}}$$

(2.4)

The total load required to calculate the penetration is given by the equation where χ

$$P = -2\pi \int_0^a \chi \sigma_{zz}(\chi, 0)d\chi$$

(2.5)

For isotropic elastic half-space, the axisymmetric displacement field w(r) in the region r ≤ a and stress σ_{zz} corresponding to (r, θ, z) satisfies the following equations [107, 111]. In this solution, the test sample is bounded on equipment surface and shear traction between the

Chapter 3: Development and Validation of Numerical Model

indenter and test sample are assumed to be negligible. A typical rigid flat ended cylindrical indentation of radius "a" and soft tissue with thickness h is shown in Figure:2.2.
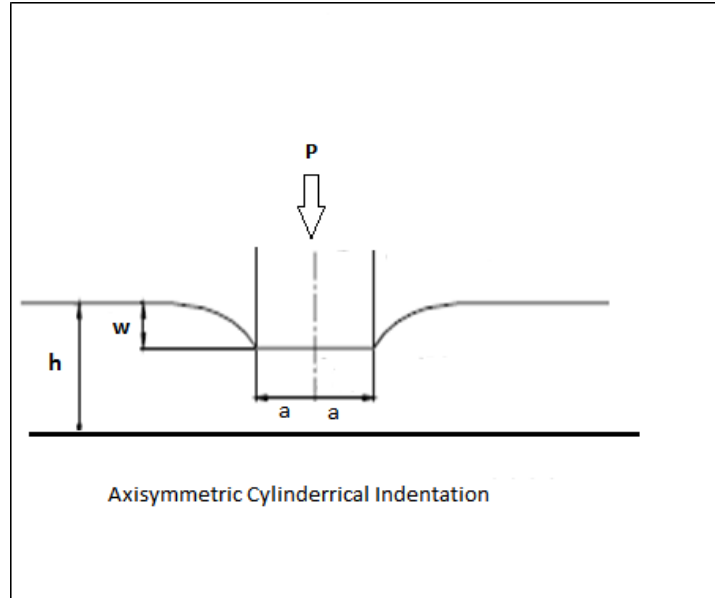
Figure 2.2: Rigid flat cylindrical indentation of radius "a" and thickness h modified from [25].

The boundary conditions underneath the indenter in z direction at the test specimen:

Case 1: There is no normal stress acting on the free surface outside the contact region σ_z.

$$\sigma_{\chi z} = 0 \tag{2.6}$$

$$w(\chi) = f(\chi/a) \tag{2.7}$$

$$\sigma_z(\chi, 0) = 0; \ r \leq \chi \leq a \tag{2.8}$$

Case 2: The contact region between the indenter and the elastic half space (test specimen) are frictionless [12, 107].

$$\sigma_{zz}(\chi, 0) = 0; \ r > a \tag{2.9}$$

Chapter 3: Development and Validation of Numerical Model

Case 3: The force should be consistent for displacement in the z direction Uz. Due to sharp edge of the cylindrical indenter σz → ∞; when r = a

$$\sigma_{rz}(r,0) = 0; \ r \leq a \tag{2.10}$$

By solving the integral [28], the total load P required for deformation w of a cylindrical punch is   given below:

$$P = \frac{2Eaw}{1-v^2} \tag{2.12}$$

The distribution of stress under the punch is given by:

$$\sigma_{zz}(\chi,0) = \frac{2\mu aw}{\pi(1-v)}(a^2 - \chi^2), 0 \leq \chi \leq a \tag{2.13}$$

And deformation is given by:

$$U_z(\chi,0) = \frac{2w}{\pi}\sin^{-1}(a/\chi), \ \chi > a \tag{2.14}$$

Where, μ is shear modulus, E is Young's modulus and χ is a function of deformation w.

2.3.2 Spherical Indentation

A spherical indenter solution was first developed in 1900 and Brinell hardness test was used for indentation.

Chapter 3: Development and Validation of Numerical Model

Spherical indentation
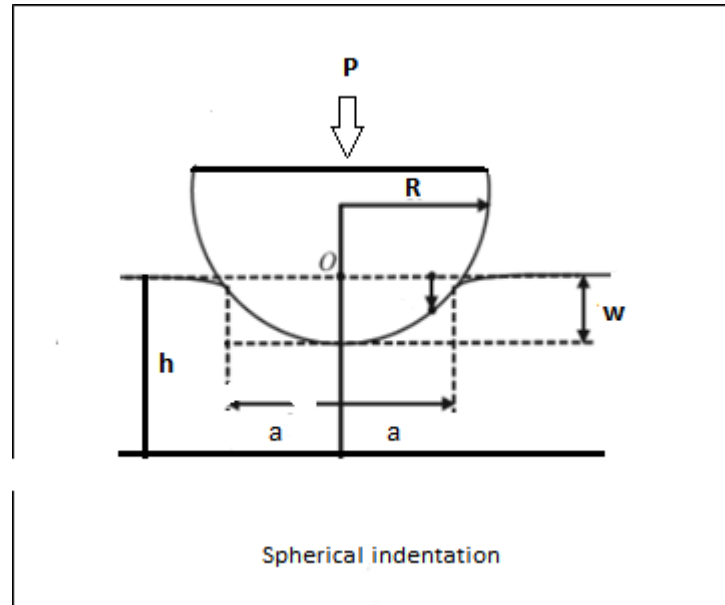
Figure 2.3: Schematic of spherical indentation of radius "a" and specimen of thickness h modified from [32].

Let us consider a sphere of radius R pressing upon an elastic solid and reaching equilibrium over a circle of radius a such as shown in Figure 2.3. Under such conditions, the displacement w is given by the equation

$$w = \frac{1}{2} log \frac{R+a}{R-a} \tag{2.15}$$

$$P = \frac{\mu}{1-\mu}(a^2 + +R^2)log \frac{R+a}{R-a} aR \tag{2.16}$$

Where, μ and v are the shear modulus and Poisson's ratio.

The equations for stress and deformation in a half space can be derived from by Boussinesq's solution. In 1962, Ahlvin and Ulery [37] introduced an influence diagram and table of coefficients to solve Love's equation. There has been a great interest to use this solution in biomedical applications. The vertical compressive stress at any depth directly underneath the

Chapter 3: Development and Validation of Numerical Model

centerline of a circular area subjected to a radially symmetric distribution of stress for point load can be calculated by integrating Boussinesq's equations [27]. For a uniform pressure, the vertical compressive stress at a depth z beneath the centerline is stated below as follows:

$$\sigma_z = P \left[1 - \left(\frac{1}{1 + \left(\frac{R}{z}\right)^2} \right)^{3/2} \right] \qquad (2.17)$$

For the case of a uniform pressure, P, applied over a circular area of radius R, Boussinesq introduced the influence factor I to find the deformation at any point within a circular plate. Underneath the center of the plate, the influence factor (I_F) is 1.0 and decreases towards its edge, where it becomes 0.637 [27]. For a circulate plate, the Poisson's ratio is assumed to be 0.5.

$$U_z = PR \, \frac{2(1 - v^2)}{E} I_F \qquad (2.18)$$

In 1951, Timoshenko and Goodier reported that when a vertical force P is applied on an axisymmetric rigid circular plate, Boussinesq's stress distribution follows the equation below where R and r is the radius of the circular area and variable radial distance "a" respectively and P is the contact pressure.

$$P = \frac{P}{2\pi R \sqrt{R^2 - a^2}}$$

2.4 Biomechanics of Soft Tissues

Biomechanics seeks to understand the effects of forces that act on living tissues. Organs are composed of soft tissues that are combined to support biology and protect the human body and structure [24]. Soft tissues make up organs such as the heart, lung, kidney, and skin. The

Chapter 3: Development and Validation of Numerical Model

mechanical behavior of soft tissue is highly influenced by the concentration of collagen and elastin. Collagen is the main component of extracellular matrix of connective tissue which is a protein of about 280 nm in size that runs in parallel to form oriented fibers [24]. Soft tissue is approximated as non-linear [10], isotropic [11] and incompressible [12].

Biological tissues are soft and typically have large deformability, PVA a good candidate to mimic their mechanical behavior. PVA is a promising biomaterial suitable for tissue mimicking phantoms. Due to its hydrophilic, biodegradable and biocompatible characteristics PVA has been chosen as a number one candidate for biomedical research [65, 70]. PVA has com- mon mechanical properties with human soft tissue structure. As such many studies have been performed to understand the fundamentals of the indentation problem applied to biological soft tissue mimics with polyvinyl alcohol cryogel (PVA-C). They are constructed based on properties obtained through mechanical testing including indentation with different standard indenter geometries such as cylindrical, spherical, conical [40] and Nano indenter [112–114].

Table 2. 1 Mechanical properties of soft tissues [39] and their associated biochemical data [21, 24]

Material	Ultimate Tensile Strength(kPa)	Ultimate Tensile Strain (%)	Collagen (% dry weight)	Elastin (% dry weight)
Tendon	50-100	10-15	75-85	< 3
Ligament	50-100	10-15	70-80	10-15
Aorta	0.3-0.8	50-100	25-35	40-50
Skin	1-20	30-70	60-80	5-10
Articular Cartilage	9-40	60-120	40-70	0

Chapter 3: Development and Validation of Numerical Model

2.5   Continuum Mechanics of Soft Tissues

Continuum mechanics studies the mechanics of a class of materials referred to as continuum, which includes solids, and fluids. Continua are assumed to consist of continuously distributed material within its volume. While in general continua has a heterogenous microstructure, this heterogeneity is ignored. Continuum differential equations are developed to govern the material's forces and deformation. These equations are introduced in this thesis based on fundamental laws of continuum physics [115].

To understand the biomechanics of soft tissue subjected to different loads is crucial. As the biological material undergoes large deformation, it is important to characterize the soft tissue behavior using continuum mechanics theory [39, 116]. Let us consider a particle on the body which is initially located at $x = (x_1, x_2, x_3)$ and displaced to a position $y = (y_1, y_2, y_3)$ The displacement vector u is described by the equation:

$$\mathbf{u} = \mathbf{y} - \mathbf{x} \tag{2.20}$$
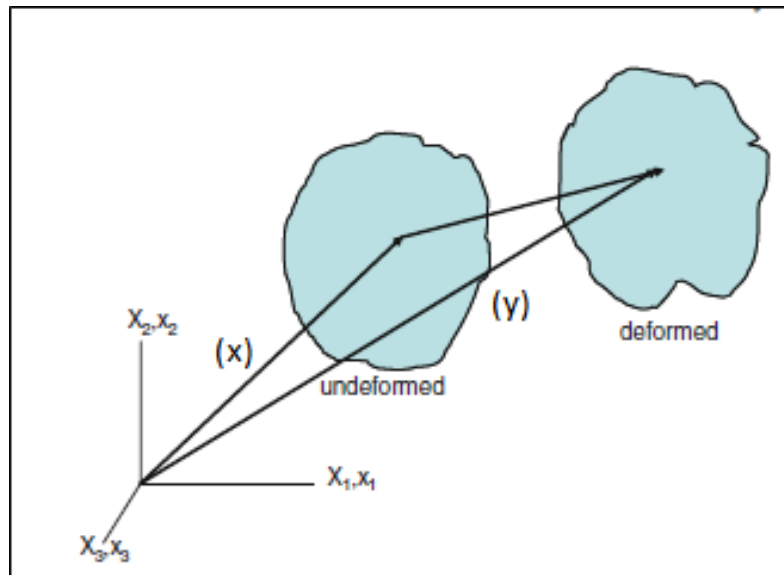
Figure 2.4: Schematics of the general motion in the neighborhood of a particle within a continuous deformable body. This image has been modified from [33].

Chapter 3: Development and Validation of Numerical Model

$$u_i\left(x_1,\ x_2,\ x_3,t\right) = y_i - x_i \tag{2.21}$$

2.5.1 Linear Elastic Model

The linear elastic model is used to approximate the indentation response of soft tissues characterization. The linear material exhibits a linear relationship between stress and strain. For an ideal linear elastic material under quasi-static conditions where the strain is less than 5%, Hooke's law which is given below, is valid:

$$\sigma_{ij} \quad = \quad C_{ijkl}\varepsilon_{kl} \tag{2.30}$$

Here, C_{ijkl} stands for tensor of elastic constants. For an isotropic solid the above equation is simplified to the following equation:

$$\sigma_{ij} \quad = \quad \frac{E}{(1+v)}\{\varepsilon_{ij}\ +\ \frac{v}{(1-2v)}\varepsilon_{kk}\delta_{ij} \tag{2.31}$$

Using a vector representation of the stress and strain tensors, they can be related via the following matrix equation.

$$\sigma \quad = \quad M\varepsilon \tag{2.32}$$

2.5.2 Hyperelasticity

Hyperelastic materials are explained in terms of a "strain energy potential" W, which describes the stored strain energy per unit volume as a function of the strain at that point in the material [16]. Hyperelastic materials are considered to be truly elastic as they store energy during loading and dissipate equal amount of energy during the unloading process. These materials experience large strain values as high as 500% for rubber, which are mostly recoverable. George Green (1793−1841), introduced the strain-energy function into elasticity for which such a function is referred to as Green elastic or hyperelastic [91, 117]. Incompressible material does not change their volume during deformation. This is described by their Poisson's ratio of

Chapter 3: Development and Validation of Numerical Model

0.4 or shear modulus (μ) approaching infinity. Hyperelastic material exhibits nonlinear stress-strain behavior. Such materials are widely used in many biomedical applications such as artificial organs, implantable surgical devices etc. [64].

Consider a hyperelastic material undergoing stress. The total work done during deformation in a continuum deformable body depends on the initial configuration at time t_0 and present configuration at time t. Deformation of a hyperelastic material does not depend on deformation history and path. A material is called Cauchy-elastic in which the stress in deformed configuration at each point is determined only by the current state of deformation relative to the undeformed configuration. Cauchy stress is independent of deformation history [85].

Stress is determined from the derivative of W with respect to the Lagrangian strain tensor and right Cauchy-Green deformation tensor. The internal strain of a body corresponds to elastic strain energy potential function is represented as a function of Green-Lagrange strain. The conjugated stress of Green-Lagrange strain and the second Pialo-Kirchhoff stress S, is expressed as the partial derivative of strain potential energy with respect to Green-Lagrange strain:

$$S = \frac{\partial w}{\partial E}(E) \tag{2.22}$$

where, W is the elastic strain energy potential. The Cauchy-Green deformation tensor is reformed by the following equation:

$$S = 2\frac{\partial w}{\partial C}(C) \tag{2.22}$$

Where,

S = Second Piola-Kirchhoff stress tensor   W = Strain energy function

E = Green Lagrangian strain

C = Right Cauchy-Green deformation tensor

Chapter 3: Development and Validation of Numerical Model

F = Deformation gradient tensor.

J = Jacobian matrix

The Jacobian is related to volume change of a material due to deformation. For an ideal incompressible material, $J = \det F = (\lambda_1 \lambda_2 \lambda_3) = 1$ given:

$$F = \begin{bmatrix} \lambda 1 & 0 & 0 \\ 0 & \lambda 2 & 0 \\ 0 & 0 & \lambda 3 \end{bmatrix} \tag{2.24}$$

The Right Cauchy Green deformation tensor C is given by the equation:

$$\mathbf{C} = \mathbf{F^T F} \tag{2.25}$$

The Left Cauchy Green deformation tensor C is given by the following equation:

$$\mathbf{B} = \mathbf{F^T F} \tag{2.26}$$

Cauchy stress σ can be calculated by inverse full Piola transformation as given below:

$$\sigma = J^{-1} FS\, F^T \tag{2.27}$$

The equation of Cauchy stress becomes:

$$\sigma = J^{-1} [\frac{\partial w}{\partial E}(E)\,] FS\, F^T \tag{2.28}$$

$$\sigma = 2J^{-1} [\frac{\partial w}{\partial C}(C)\,] FS\, F^T \tag{2.29}$$

2.6   Hyperelastic Model

In general, a hyperelastic material is an elastic material that returns to its original shape after releasing the force, and the stress strain relationship is calculated from strain energy density function. This strain energy density function is explained by materials hyperelastic behavior

Chapter 3: Development and Validation of Numerical Model

[118]. Based on mechanical responses of material behavior different constitutive laws are introduced [119]. Chagnon and his co-workers reported that an effective hyperelastic model will be explained by the following [89]:

- The model will be able to replicate the whole" S" shaped response.
- The deformation model will be simple. For example, if the model works in uniaxial tension, it must be the same with shear tension.
- They consider that, the number of fitting material parameters should be small.
- For numerical performance of the model, mathematical formulation should be simple.

To define hyperelasticity many mathematical models have been developed and different aspects of material behavior are explained [117]. Rivlin and Saunders introduced even powered series of the principal stresses to explain strain energy function [118, 120]. Later Ogden introduced a strain energy function which provides precise results expressed as a series of positive and negative real powered principal stresses [85, 121] The second invariant of the Cauchy-Green deformation tensors C is defined by ($I = I_1 I_2 I_3$) stated below:

$$I_1(C) = tr(C) \tag{2.33}$$

$$I_2(C) = \frac{1}{2}[\ (trC)^2 - tr(C)^2\ ] \tag{2.34}$$

$$I_3(C) = \det(C) \tag{2.35}$$

The strain-energy function of isotropic hyperelastic material in terms of invariants is denoted by:

$$W = \int (\ I_1 I_2 I_3) \tag{2.36}$$

where $I_1, I_2,$ and I_3 are the three invariants of each of the two Cauchy-Green deformation tensors. In terms of the principal extension ratios λ1, λ2, and λ3 they are expressed by:

Chapter 3: Development and Validation of Numerical Model

$$I_1 = \lambda_1^2 + \lambda_2^2 + \lambda_3^2 \tag{2.36}$$

$$I_2 = \lambda_1^2\,\lambda_2^2 + \lambda_2^2\,\lambda_3^2 + \lambda_3^2\lambda_1^2 \tag{2.37}$$

$$I_3 = \lambda_1^2\,\lambda_2^2\lambda_3^2 \tag{2.38}$$

The strain energy function per unit volume in hyperelastic model is defined by W, and it depends symmetrically on principle strains $\lambda1$, $\lambda3$, $\lambda3$. These principle strains can be calculated with the square root of right Cauchy deformation tensor and left Cauchy deformation tensor.

$$W\,(\lambda_1, \lambda_2, \lambda_3) = W\,(\lambda_1, \lambda_3,\ \lambda_2) = W\,(\lambda_2, \lambda_1,\ \lambda_3) \tag{2.39}$$

Again, we can define the strain energy (W) in terms of invariants (I_1, I_2, and I_3). The left Cauchy Green deformation tensor (*Bij*) expressed in terms of principle strains. (λ_1, λ_2, and λ_3).

$$W\,(F) = W\,(I_1,\ I_2, I_3) = W\,(I_1,\ I_2, J) = W\,(\lambda_1, \lambda_2,\ \lambda_3) \tag{2.40}$$

2.7   Previous Studies

2.7.1   Soft Tissue and Tissue Mimic

For the last few decades there has been increasing interest of characterizing the mechanical properties of soft tissues specially in biomedical research such as needle insertion techniques [5], robotic surgery [125], surgical simulation and training [126]. Numerous studies have been conducted to determine the mechanical properties of soft tissues using tissue mimicking phantoms. To characterize material properties using soft tissue, tissue mimicking phan- toms have been widely described to be an appropriate tool for research and development [64].

The mechanical properties of soft tissue have been investigated in variety of techniques such as uniaxial testing, biaxial testing and different forms of indention testing techniques.

Chapter 3: Development and Validation of Numerical Model

Biological soft tissue is a complex material and it is composed of elastin, actin, resilin, abductin and collagen [36]. Many previous investigations postulated that soft tissues undergo large deformation due to their low stiffness, hence exhibiting material non-linearity [11, 30]. Out of all soft tissue constituent's elastin and collagen are the most important component of biological soft tissues [36, 59].

Biological soft tissues are inhomogeneous, anisotropic and are often subjected to large deformations [30] and often exhibit viscoelastic behavior. Generally, the mechanical behavior of biological soft tissues is more complex than engineering materials [19, 127]. The mechanical properties of soft tissues have been estimated in vivo, ex vivo, or using soft tissue mimic (e.g. PVA-C) by employing (i) stretch tests [128], (ii) aspiration experiments [129], (iii) compression tests and, (iv) needle insertion, for linear [130] and non-linear bio-mechanical models [94]. This complex mechanical behavior of such tissues is also often characterized by using indentation testing based on resulting tissue response to applied load [39].

It is very difficult to use human and animal cadaveric tissues to develop medical devices because of its biodegradability and hygienic or biohazard risk factor [5, 131]. Advantages of using tissue-mimicking materials include (i) biodegradability and steady shape preservation (ii) having similar mechanical properties of human tissues [5]. It is also a proven to be a good choice as bio-compatible material for preparing tissue mimicking phantoms [34, 72, 76].

The mechanical properties of soft biological tissues and hydro-gels such as polyvinyl alcohol cryogel (PVA-C) [5, 6, 34], PVA hydrogel [65], polydimethylsiloxane (PDMS) [6], Bovine gelatin (BoGe10), porcine gelatin (PoGe-10X) [26], PEG hydrogel materials synthesized from polyethylene glycol, dimethyl methacrylate (PEGDMA) and monomer [66], have been studied by many researchers using various test methods and established procedures for usage in biomedicine [67].

Table: 2.1 A List of papers describing mechanical properties of human organ/tissues modified from [38].

Chapter 3: Development and Validation of Numerical Model

Authors	Human Organ/ Tissue	Young's Modulus (MPA)	Hydrogel Preparation
Lepage et al. (2015)	Bladder	0.128	10% 4FTC, 15% 2FTC
Rubod et al.(2006)	Galbladder	0.015-0.05	15% 6FTC, 20% 4FTC & 6 FTC
Rebelo et al. (2013), Casciaro et al. (2009)	Kidney	6.7-41.5	
Rubod et al. (2012), Al-ja'afreh et al. (2008)	Liver	0.46-0.56	20% FTC
Rosen et al. (2008)	Large intestine	0.20-0.33	15% 6FTC, 20% 4 FTC
Rosen et al. (2008)	Small Intestine	0.22-0.60	20% 4 & 6 FTC
	Stomach	0.30-0.52	20% 6 FTC
Mebius et al. (2005)	Spleen	0.18-0.20	15% 4 & 6 FTC
Franceschini et al (2006)	Whitenmatter	0.0017-0.0054	-
Mesa-Munera (2011)	Grey Matter	0.0016-0.0031	-
	Thalamus	0.0025-0.0032	-
	Midbrain	0.0025-0.0033	-
Saxena et al. (2012)	Spinal Cord	0.0002-0.007	5% FTC
Samani et al. (2004), Ramiao et al. (2009)	Breast (human)	0.00325-0.0008	5% 2FTC
Egorov et al. (2012)	Vaginal Tissue (Female)	0.0074	
Lyshchik et al. (2005)	Thyroid	0.009-0.0114	5% 4& 6 FTC
Pailler-Mattei et al. (2008)	Skin (Human)	0.001-0.008	5% 2 & 4 FTC
Spiller et al. (2011)	Articular Cartilage (Fibrous)	0.32	20% 6FTC
Boschetti et al. (2004), Delaine-Smith et al. (2016)	Articular Cartilage(Hyaline)	0.80-2.78	
Elsheikh et al. (2011), Elsheikh et al. (2007)	Cornea	1.59-0.961	20% 6FTC
Mathew et al (2014)	Sclera	0.269-0.412	15% 6FTC
Mathew et al (2014)	Aquas Humour		2% 6FTC
	Intervertibral Disk		
Wang et al. (2009)	Anulus Fibrous	2.9-6.1	
Hoyt et al (2008)	Nucleus Pulposus	.269-0.412	5% 1FTC
Kot et al. (2012)	Muscles(RF)	0.00922-0.08512	
Carson et al. (2011), Krouskop et al. (1998)	Prostate	0.002-0.0056	5% 2 FTC

Polyvinyl alcohol (PVA) is a commercially available water-soluble powder. Hydrogels are called chemical gels when they are covalently cross-linked [132]. The concentration of this hydrogel is determined by its application. At a higher concentration 25 (w/w%) the hydrogel becomes sticky and extremely difficult to work with [34]. Hoffman and his co-workers successfully used PVA hydrogels to cultivate living cells as hydrogels have large pores and are capable of degradation [69]. The use of hydrogel structure depends on freeze–thaw cycle [5, 6, 13, 69]. Due to its excellent biocompatibility, chemical stability and appropriateness PVA hydrogels have become a major candidate for various biomedical applications [4–6].

PVA hydrogel has been used in many biomedical applications. In 1990, Kita et al. developed hydrogel for contact lens material. They compared their developed contact lens with commercially available contact lens material like polyhydroxy-ethyl-methacrylate (PHEMA) and copolymers of methyl-methacrylate (MMA) and N-vinyl pyrrolidone (N- VP) [79]. They also reported that PVA hydrogel showed higher tensile strength and elongation before breaking than any other commercially available materials.

Chapter 3: Development and Validation of Numerical Model

Tanabe and Nambu introduced a unique method of crosslinking aqueous PVA by applying freeze-thaw cycling [133]. Stauffer and his co-worker reported that hydrogels formed by the freezing and thawing cycles can be elongated up to 5 to 6 times their original shape. They also reported that this rubbery and elastic nature is a strong indication of the formation of a new material with high mechanical strength [134]. Jiang and his co-workers reported that the structure and mechanical properties of PVA hydrogels changed significantly with the increase of freeze-thaw cycle. They found that at 5 freeze-thaw cycle the hydrogel's Young's modulus increased from 3.6 kPa to 11.4 kPa, which is very similar to porcine liver tissues [65].

Li and his group (2015) developed a pelvic model with transparent polyvinyl alcohol hydrogel as a substitute for human soft tissue. In the process of building prostate tissue mimicking phantom they used 7 freeze-thaw cycle. They used insertion force comparison between organ and tissue mimicking phantom and found the same mechanical properties between the two [80].

In 2009, Wang et al. experimented on PVA-C to mimic natural lumbar intervertebral disc [76]. They used PVA-C due to its high-water content, excellent biocompatibility, and versatile mechanical properties [6, 76, 79]. They found unique results with 3% 3 FTC, PVA-C, which became the number one candidate for tissue mimicking artificial nucleus pulposus. Their work helped to fill the gaps in replacing the human lumbar IVD with PVA-C.

PVA cryogel is used to mimic human soft tissues (cornea, sclera, vitreous humor) [13]. PVA-C construct can mimic human tissue as it can be built to have similar biomechanical properties [6, 34]. PVA-C has increased mechanical strength while it exhibits no toxic effect when prepared in an appropriate ratio of PVA and water in repeated freeze thawed cycle of freezing at 22∘C and thawing at a room temperature [6]. PVA hydrogels are popular in "tissue engineering" for reconstructing and regenerating tissues and organs [65]. A typical tissue mimicking eye construct is prepared at six freeze-thaw cycle along with a block diagram of its preparation are shown in Figure: 2.5 and Figure: 2.6, respectively.

Chapter 3: Development and Validation of Numerical Model

Figure 2.5: A tissue mimicking eye (PVA-C) at 6 freeze-thaw cycles modified from [34].

Figure 2.6: Preparation of tissue mimicking eye construct with PVA-C hydrogel [5].

Soft tissue mimics can help medical residents and trainees get surgery training to enhance their skills for safer and more accurate surgical procedures. This state-of-the-art development will improve patient care and reduce health care cost significantly. For a researcher, understanding material properties of soft tissues is vital for the development of artificial organ and tissues. This novel work will help researchers to develop artificial organs which is biocompatible and has similar mechanical properties to biological soft tissues.

2.7.2 Indentation Studies on Soft Tissue Mimics

The existing literature on indentation on soft tissue can be categorized into two general groups. The first one includes numerical indentation studies on soft tissue and mimics, and the second one includes experimental indentation studies on soft tissue and mimics. A number of studies of numerical and experimental indentation on soft tissue and mimics have been published earlier, and some of those which are more relevant to this dissertation are discussed below: The mechanical properties of soft tissues and mimics have been investigated by many researchers previously.

Table 2.2: List of some papers based on material and material characterization techniques modified from [38].

Chapter 3: Development and Validation of Numerical Model

Author Year	Experiment	Indentation Technique	Thickness	Materials	Range of E	Sample Thickness	Solution	Results
Wozniak 2002	Numerical Analysis	Cylindrical Indentation	Elastic 1/2 space				FEA	contact pressure distribution
Ming Zhang 1997	Numerical Analysis	Cylindrical Indentation	Infinite Elastic Layer	Soft Tissue	100 Kpa	3 mm - 30 mm	FEA Axisymmetric	Effect of Friction on Young Modulus
F. Yang 2003	Analytical	Cylindrical Indentation	Finite	Thin Film	Not known	thin	Closed form	Contact force is inversely proportional to film thickness independent of contact radius
Choi 2005	Numerical	Cylindrical Indentation	Finite	Cartilage	60 Kpa	4.5 mm	Axisymmetric	Nonlinear effect cased by Finite deformation
Carter 2001	Experiment Numerical	Indentation	Finite	Procine Liver Human Liver Human Liver	4.0 kPpa 0.27 kPa 0.74 kPa	(Diseased)	Axisymmetric	Young Modulus
Chowdhury 2001	Numerical	Cylindrical Parabolic	Finite	Homogeneous Material			Axisymmetric	Stress
Pinyochotiwong 2013	Analytical Cylindrical	Numerical	Finite	Soft Tissue			Axisymmetric	Force , Depth
Derline-Smith Stress strain 2016	Numerical	Cylindrical	Finite	Soft Tissue			FEA Axisymmetric	Displacement
Mayne 1999	Analytical Experimental Numerical	Cylindrical	Finite Infinite				FEA	Displacement influence factor
Cox 2014	Experimental Spherical	Spherical	Finite	PMMA			FEA	Force Displacement
Finan 2014	Experimental Numerical	Cylindrical	Finite	Brain			FEA	Force Displacement

Each type of soft tissue forming an organ has unique functionality, and while they are composed of very similar constituents, but have different structure and exhibit various properties [127]. They tend to be highly nonlinear, anisotropic and inhomogeneous [29, 30]. To quantify and characterize non-linear, non-homogeneous and anisotropic soft tissue behavior accurately [94] many indentation techniques have been introduced previously [3, 30, 59, 92, 94]. Due to the complexity involved in obtaining accurate data using indentation testing, interpreting such data towards characterizing mechanical properties of soft tissues used to be very challenging [94].

In 2011, Carson et al. conducted ex vivo spherical indentation tests for characterization of prostate tissue. They used 4.5 mm thick tissue specimens and reported that the Young's modulus of diseased prostate was significantly higher than the surrounding normal tissue [19].

In 2008, Cox et al. reported that bioprosthetic heart valve offers promising alternative for current treatment and replacement of heart valves [10]. Heart valve leaflets are composed of collagen fiber networks and their mechanical properties are highly nonlinear, anisotropic and inhomogeneous [10, 13]. Indentation test provides sufficient information for characterization of nonlinear, and anisotropic soft tissue properties. In order to avoid complexities of using heart valve leaflet, they used polydimethylsiloxane (PDMS) for its low stiffness and similarity to soft biological tissue.

Chapter 3: Development and Validation of Numerical Model

Firstly, they conducted indentation test with varying indenter sizes and compared their results to results obtained from tensile tests on the same specimens [13]. Secondly, they used uniaxial or biaxial statically constrained conditions for tissue engineered specimens, while they are used digital image correlation method to measure the anisotropy of tissue construct. After validation optimization algorithm was used to extract the specimen material parameter though minimizing the difference between experimental and simulated data [10].

In 2016, Delalleau et al. examined the mechanical properties of soft biological tissue using unconfined compression [135]. Based on limited previous studies, they reported that adipose, breast, livers, kidney and prostate tissues mainly exhibit compressive behavior [136] while most common form of indentation testing involved compression [137]. They also used flat-ended cylindrical indentation for mechanical properties of soft tissue specimens and to calculate their elastic moduli. In order to validate their results, they developed correlation factors and compared their results with uniaxial compression values [135].

Hertzian (spherical) indentation technique was the first kind to solve contact problems associated with elastic stress field where contact radius increases with applied load [31]. With Cylindrical (flat ended) indentation where contact radius is fixed with applied load a closed form solution is available [45]. Hayes et al. [29] developed a mathematical model for indentation test on articular cartilage. They considered it as a mixed boundary value problem.

An axisymmetric flat ended cylindrical indentation was modeled as an infinite elastic layer bonded to a rigid half space. They reported that for a linear elastic flat-ended cylindrical indenter with a fixed contact area, the deformation is directly proportional to the applied load. In 1997, Zhang et al. performed a numerical study on soft tissue indentation to estimate the effective Young's modulus [25]. They developed a nonlinear FE analysis to investigate the influence of friction and large deformation on the calculation of the effective Young's modulus. A layered soft tissue on bone was also modeled as an indentation of an infinite elastic layer bonded to a rigid boundary. E = 100 kPa and ν = 0.499 was considered in the respective FE analysis.

Chapter 3: Development and Validation of Numerical Model

In 2008, Cao et al. conducted a computational study of axisymmetric cylindrical indentation on a compressible elastic layer to solve axisymmetric frictional contact problem [30]. They further verified their results with numerical analysis. Based on Lebedev and Ulfiand [138], they developed a numerical technique to solve Boussinesq's problem. The radius to thickness (a/h) ratio varies from (0~20). They introduced a dimensionless function Π which was normalized by a function [30]. When (a/h) approaches 1 solution degenerates to Sneddon's equation. When (a/h) approaches infinity the load-depth curve converges to Jaffar's solution [98].

To understand the effect of indenter geometry and soft tissue thickness Final et al. (2014) carried out a numerical analysis on cylindrical, spherical and rounded cylinder indentation. For a cylindrical indenter, the effect of finite thickness was significant, and it increased the influence of large strains and friction between the indenter and sample. Even though for shallow indentations, the effect of finite thickness on cylindrical indenter cannot be neglected. For a spherical indenter, they found that there was a significant effect of finite thickness in shallow indentations because, the contact area depends on indentation depth [9, 29].

In 2005, Choi and Zheng investigated the effect of finite deformation on soft tissues [92]. They used different sized indenter to estimate Poisson's ratio and Young's modulus. They constructed two axisymmetric modeled with a flat ended rigid indenter of radius 5.5 mm and 9 mm. High grid density was introduced underneath both indenter for simulation. The modeled soft tissue was considered a linearly elastic and isotropic material.

A number of mathematical models have been developed [27, 28] to explain the behavior of soft tissues. Unfortunately, it is not possible to describe mathematical models for nonlinear materials without restoring to numerical models [89]. Indentation testing is not only used for characterizing solids [40] but also it is an ideal tool for investigating tissue mimics and their developments in tissue engineering applications [96, 97].

To avoid the stress singularity, they also introduced a round edge cylindrical indenter with a radius of 10 µm. They considered the material as isotropic and used Ogden hyperelastic constitutive law with Ogden parameters, $\mu = 2.553$ kPa and $\alpha = 1$. They reported that when the

Chapter 3: Development and Validation of Numerical Model

ratio of the sphere of the indenter radius to the internal radius of the indenter less than one, the rounded cylindrical indenter behaved like a cylindrical indenter. They also reported that there was a significant thickness effect on Poisson's ratio and non-dimensional value k.

In 2004 Samani and his co-worker developed a measurement method to characterize material parameters of breast tissue. They developed a tissue indentation technique to obtain the force-displacement response of breast tissue. They used a tissue specimen of (15x15x10) mm3 and constrained it within a cylinder to minimize tissue motion and deformation. A cylindrical indenter of diameter 5 mm connected with a servomotor used for indentation response and output was recorded via a LabVIEW. They used data inversion technique and forward analysis for tissue characterization. [15].

Zhang and his co-workers conducted an extensive study of hyperelastic material with spherical indentation through theoretical, computational, and experimental work [118]. They used constitutive models including neo-Hookean, Mooney-Rivlin, Fung, and Arruda-Boyce models. Based on hyperelastic load-displacement results, they examined the applicability of Hertzian solution to the measurement of the initial shear modulus. They have conducted tests on synthetic tissue made of polydimethylsiloxane to validate their theoretical analysis. They reported that the hyperelastic indentation response on soft materials is an ill-posed problem. They stated that an inverse problem is ill-posted if (i) a solution to the problem does not exist (existence) (ii) more than one solution exists (uniqueness) and (iii) the stability of the solution is violated [139, 140]. In order to investigate the solution of the inverse problem, they also mentioned the importance of the above-mentioned properties since there is no straightforward method of characterizing the hyperelastic material properties of soft tissue.

Naimani and Simha conducted an axisymmetric finite element analysis to investigate hyper-elastic parameters of soft tissue layers [95]. They used Mooney-Rivlin, polynomial (POLY), exponential (EXP) hyperelastic material model for hyperelastic parameter extraction. They reported that these parameters are independent of E. They used optimization algorithm for parameter extraction then conducted R^2 test for convergence accuracy and sensitivity analysis

Chapter 3: Development and Validation of Numerical Model

by adding percentage of error. They validated their results with Samani et al. [137] and Cox et al. [10].

Mesamunera and co-workers [90] experimented and modeled brain tissue using anisotropy assumption. They also implemented FEA parameter estimation algorithm for material characterization [91, 129]. Previous researchers reported that the stiffness of brain is very low, and it is about eight orders of magnitude less than engineering material [142]. Samani and his coworker worked on characterizing the nonlinear behavior of breast tissues. They mentioned that breast tissue has low stiffness and undergoes large deformation [15]. Simha and his coworker reported that the nonlinear elastic parameters of breast tissue is an indicator of breast cancer [143]. Based on experimental analysis, Kruskop discussed the dependency of Young's modulus of breast tissue with the level pre-compression which further demonstrates breast tissue nonlinearity [137, 144].

In 2016, Isvilanonda et al. conducted experimental work and FE simulation on sub calcaneal soft tissue [91]. They used inverse FE analysis to identify the first order and second-order Ogden hyperelastic material properties of the tissue. They followed Pai and Ledoux [141] testing protocol and method for the preparation of test specimen. They used displacement control triangle waves of frequencies (1Hz) to compress the tissue to an average of 48% strain. They averaged the data from three consecutive loading and unloading load-displacement cycles be- fore and using them as input data in their inverse FE analysis.

They reported that, at 30% compression the simulated deformation was within 3.6% of the peak deformation of the analytical solution [91]. They used inverse analysis for error optimization and parameter estimation and found consistency with experimental results. They suggested that the force-displacement response from the model was highly sensitive to Poisson's ratio and Ogden coefficient α.

2.8   Summary

In this chapter, an extensive literature review was conducted regarding indentation biomechanics of soft tissues. The objective of this chapter was to investigate the biomechanics of polyvinyl alcohol cryogel (PVA-C). Human tissues are nonlinear, anisotropic, and heterogenous. Due to the complexity involved in obtaining accurate experimental data, characterizing mechanical properties of soft tissues is challenging.

Many previous researchers discussed about large strain rate and materials intrinsic nonlinearity. Based on the available literature, it may be hypothesized that, despite of the understanding of the tissue responses from indentation test, still there is still a huge gap of understanding between the distribution of stress at any point within the specimen.

FE software Abaqus will be used for characterizing mechanical properties of soft tissue phantom. The experimental data provided by [38] would be used in the next chapter for numerical analysis.

Chapter 3

Development and Validation of Numerical Model

3.1 Introduction

Finite element method (FEM) was introduced in the mid-nineteenth century to solve elastic structural analysis problems in civil and aeronautical engineering where a system of partial differential equations that govern the problems needs to be solved. This method has been used to solve numerous complex problems such as stress analysis, heat transfer, wave propagation and many other problems in the engineering domain where analytical solutions cannot be obtained. FEM is regarded as the gold standard for providing numerical solutions to challenging problems arising in engineering, applied mathematics, biomedical Engineering.

There are many powerful commercial simulation packages readily available for structural analysis which have been developed based on FEM. They include Solid Works, ANSYS, MATLAB, Abaqus and others. Abaqus uses iterative solution techniques for solving nonlinear problems. It runs in two simulation environments, standard and explicit. Abaqus version 6: 13 − 4(2013) has been used as a simulation tool as part of algorithm developed for characterizing material property in this thesis.

Chapter 3: Development and Validation of Numerical Model

This chapter introduces the development and validation of a numerical model using (FEA) developed to simulate indentation. The main objectives of this chapter are stated as follows:

- Developing a numerical model for the cylindrical indentation test using finite element analysis implemented in Abaqus to predict the behavior of linear and non-linear materials.

- Assessing the effects of contact interaction, choice of elements, methods of applied loads friction coefficient and sample thickness on indentation response.

- Evaluating various constitutive relations used for linear and non-linear elastic models used for matching experimentally acquired stress and strain data of soft tissues with their simulated counterpart obtained through FEA.

- Evaluation of the finite element models based on experimental results for the indentation problem.

The first section of this chapter describes a general technique for solving a solid mechanics problem using FEM Abaqus version 6:13−4(2013). This section also describes the steps involved in the simulation, including the mathematics behind solving non-linear finite element equation using the Full Newton method. The second section of this chapter discusses the development and implementation of the numerical model, the third section of this chapter discusses non-linear hyperelastic models and finally the fourth section addresses validation of the model. This chapter is concluded with a brief validation exercise followed by a summary.

3.2   Procedure for Solving a Numerical Problem

In order to characterize the mechanical properties of soft biological tissue by Finite Element Method, a detailed understanding of the numerical problem is essential. To solve the system of equations, knowledge of the global stiffness matrix formulation is essential. A detailed

Chapter 3: Development and Validation of Numerical Model

theoretical understanding of the problem is crucial to validate results in the simulated environment.

3.2.1 Finite Element Analysis

This section discusses the approach for the finite element analysis. A commercially available software Abaqus completes the following tasks.:

1. **Pre-processing:** this task defines geometry including discretization using finite element meshing, material property, boundary condition and loading.

2. **Simulation:** in this section, the solver involves forming the problem's stiffness matrix based on approximations to the governing equations and the FE mesh before solving the equations and providing a solution for the discretized domain. This is the main processing unit.

3. **Post-processing:** In this section, the solutions are interpreted, visualized and presented either in a tabular or graphical form.

3.2.2 Numerical Model Algorithms

The solution criteria of numerical problems fall under two methods: (i) implicit method and (ii) explicit methods. Both these methods are discussed below:

Full Newton Method: The Newton Raphson method, also known as the Newton Method or the Full Newton Method, is another method for solving nonlinear finite element equations. The Full Newton equation can be written in terms of the discretized equilibrium equations:

$$\delta^e \vartheta^T K.\mathbf{u} = -\delta\vartheta^T r \tag{3.1}$$

where $\delta^e\vartheta$ are the arbitrary virtual velocities, K is denoted as the stiffness matrix and r is the residual vector. The discretized Full Newton equation is stated below:

$$K(x_k).\mathbf{u} = -r(x_k) \tag{3.2}$$

Chapter 3: Development and Validation of Numerical Model

$$X_{k+1} = X_k + u \tag{3.3}$$

For each iteration k, both the residual vector and the stiffness matrix are re-evaluated, and a displacement increment u is calculated by pre-multiplying an inverse of the stiffness matrix both sides of Equation (3.2). This iteration continues until a convergence criterion is satisfied. Full Newton is a computationally expensive method which requires considerable processing time.

3.2.3   Explicit Method

The explicit FEM method calculates the incremental procedure at a later time = tn+1 and updates the stiffness matrix based on geometry and material changes. It calculates a linear change in displacement over each time step. Explicit method provides accurate results due to the small-time step. A major drawback of this method is the small increment increases the computation time and insufficient increment cannot provide correct solutions.

3.3   Development of the FEA Model

For the last few decades, numerical modeling has been a very popular tool for investigating structural analysis in simulated environment. Although there are some distinct advantages with indentation testing, the interpretation of the force-displacement behavior of very soft materials is not straight-forwards. A number of techniques have been developed for interpreting indentation using elastic theoretical models, namely: Hertz [45], Boussinesq [27], Love [48], Sneddon [28] and Hayes [29]. These techniques can be employed to characterize mechanical properties of soft tissues [26].

Analytical models provide accurate solutions of mathematically defined problems. However, such models tend to rely on material and geometric simplifications, such as linear elasticity and isotropy, etc. Numerical methods, such as FEM use an approximation approach to convert partial differential equation to algebraic equations valid within each element domain.

Chapter 3: Development and Validation of Numerical Model

Numerical methods can provide sufficiently accurate solutions in comparison with analytical methods and are now commonly used in science and engineering applications.

Finite element analysis (FEA) is currently the most widely used numerical method that allows us to process theoretical and experimental models to solve boundary value problems in engineering domain [40]. FEA has been widely used in biomedical engineering application including development of artificial biocompatible tissue and characterizing their properties. Numerous investigations have tackled indentation testing and its simulation using FEM. Anderson and his coworkers [145] worked on structural analysis tools to improve the understanding of the mechanical behavior of soft tissues. Many investigations conducted on soft tissue indentation have used flat-ended rigid indenter where non-linear response was found [30, 31, 59]. Cao et al. reported that most of the material obeys Hooke's law at low strain but at higher strains, tissues exhibits non-linear behavior [30].

3.3.1   Constitutive Models

ABAQUS/CAE is the complete simulation package used in this thesis. This package works by solving the following a system of stiffness equations [119]:

$$[\mathbf{K}]\{\mathbf{u}\} = \{\mathbf{F}\}$$

(3.4)

where K is the stiffness matrix, u is the displacement vector and $\mathbf{F}$ is the force vector. The solution process is stated below:

1. Based on the definition of elements and nodes, discretize a continuous domain into a set of discrete sub-domains called finite elements.
2. After determination of the group of elements and their corresponding nodes, this defines the following interpolation scheme to relate displacements within the element to nodal displacements:

Chapter 3: Development and Validation of Numerical Model

$$u_i(X) \;=\; \sum_{a=1}^{n} N^a(X)u_i^a \tag{3.5}$$

where x stands for coordinate for arbitrary point in the solid and N^a (X) presents as an interpolation function which must be satisfied by Kronecker delta stated below:

$$N^a(x^b) = = \begin{cases} 1, & if\ a = b \\ 0, & if\ a \neq b \end{cases} \tag{3.6}$$

The shape function N can be determined for any order of P is written by the definition of Lagrangian:

$$N_i^k \;=\; \prod_{i=1, j \neq i}^{p+1} \frac{x - x_j^k}{x_i^k - x_j^k} \tag{3.7}$$

3. Using shape function third step calculates the following element stiffness equation where $[K^e]$ and $\{F^e\}$ are the element stiffness matrix and nodal force vector.

4. All the stiffness matrix $[K^e]$ and load vectors $\{F^e\}$ are assembled for each element in the domain Ωi into the following global stiffness equation. where [K] and {F} are the global stiffness matrix and global load vector respectively.

5. Apply boundary conditions.

6. Solve system of equations using $\{u\} = [K]{-}1\{F\}$

Post processing in FE simulation provides nodal displacement, force, stresses at any point of interest.

A significant body of literature is available on hyperelastic material modeling to predict mechanical response of soft tissues during indentation test. Choosing the right model is very important to identify accurate material constants [146, 147]. There are different forms of strain energy function for modeling incompressible and isotropic material [121, 147], transversely isotropic material [148] and orthotropic [149]material model. There are many constitutive models, including Ogden, polynomial, reduced polynomial, Arruda and Boyce, Neo-Hookean

Chapter 3: Development and Validation of Numerical Model

solid and Mooney-Rivlin, Van der Waals, Yeoh models, that describe material strain energy as a function of the deformation [15, 26, 119]. A few of these models are discussed below, including Ogden hyperelastic model which has been introduced as a strain energy potential in this dissertation.

3.3.1.1   Ogden Model

The Ogden constitutive model is a phenomenological model developed by Ogden [150]. This model is based on the principle strain ratio rather than strain invariants. According to Ogden, strain energy functions are based on principle strains (λ_1, λ_2, and λ_3) which are a directly measurable quantity [89]. Ogden strain energy function is considered for fitting the experimental data in this thesis. The Ogden strain energy density function is stated below [85, 126]:

$$W \ = \sum_{i=1}^{\infty} \frac{\mu_i}{\alpha_i} \ (\lambda_1^{\alpha_i} + \ \lambda_2^{\alpha_i} + \lambda_3^{\alpha_i} - 3) \ + \sum_{i=1}^{\infty} k_i (J^{el} \ - 1)^{2i} \tag{3.8}$$

For incompressible material, the Jacobian become zero and the Ogden strain energy function is reduced to:

$$W \ = \sum_{i=1}^{\infty} \frac{\mu_i}{\alpha_i} \ (\lambda_1^{\alpha_i} + \ \lambda_2^{\alpha_i} + \lambda_3^{\alpha_i} - 3) \tag{3.9}$$

Where $$\sum_{i=1}^{\infty} \frac{\mu_i}{\alpha_i} = 2\mu_i \tag{3.10}$$

For incompressible material, the principle Cauchy stress can be calculated from

$$\sigma_j \ = \ \lambda_i \frac{\delta W}{\delta \lambda_j} - \ P \ \ (j{=}1{,}2{,}3 \ ...) \tag{3.11}$$

Also due to material incompressibility, the hydrostatic pressure p is eliminated from the deformation and taken into consideration for direct equilibrium equation:

Chapter 3: Development and Validation of Numerical Model

$$\sigma_j \;=\; \sum_{i=1}^{N} \mu_i \, \lambda_{ji}^{\infty} - P \tag{3.12}$$

Let us consider the compression to be uniaxial and let the strain be in the direction of compression where $\lambda_1 = \lambda$ and corresponding principle Cauchy stress $\sigma_1 = \sigma$ and where the two other two principal stresses are zero. As the material is incompressible and no lateral forces are applied in the analysis, the stretch equation becomes:

$$\lambda_1 \;=\; \lambda_3 = \lambda^{-1/2} \tag{3.13}$$

μ_i and α_i explains the shear behavior of the constitutive material parameters. The stress equation can be written as:

$$\sigma \;=\; \sum_{i=1}^{N} \mu_i \, \lambda^{\alpha_i} - P \tag{3.14}$$

and further manipulation leads to the following:

$$0 = \sum_{i=1}^{N} \mu_i \, \lambda^{\alpha_i/2} - P \tag{3.15}$$

Substituting P from (3.15) in to (3.14)

$$\sigma \;=\; \sum_{i=1}^{N} \mu_i \, (\lambda^{\alpha_i} - \lambda^{-\alpha_i/2}) \tag{3.16}$$

where $N = 1, 2, 3...$ and in this case $N = 1$ and the Ogden stress equation becomes

$$\sigma \;=\; \mu(\lambda^{\alpha_i} - \lambda^{-\alpha_i/2}) \tag{3.17}$$

For nominal stress

$$T = \sigma \lambda^{-1/2} \tag{3.18}$$

Chapter 3: Development and Validation of Numerical Model

Hence the theoretical nominal stress for any soft tissue can be calculated by using the following equation [151]:

$$T = \mu(\lambda^{\alpha_i - 1} - \lambda^{-\alpha_i/2 - 1}) \tag{3.19}$$

where, μ and α describe the shear behavior of the material. Ali and his colleagues reported that Ogden's energy function is computationally more demanding than any other polynomial form in material characterization [147]. They also reported that the accuracy level of the Ogden model is high in fitting experimental data [89, 152].

3.3.1.2   Mooney-Rivlin Model

The strain energy function in the Mooney-Rivlin model is as follows [102, 137]:

$$W = \sum_{i+j=1}^{N} C_{ij}(I_1 - 3)^i \, (I_2 - 3)^j + \sum_{i=1}^{\infty} \frac{1}{D_i}(J^{el} - 1)^{2i} \tag{3.20}$$

When $N = 2$, $\alpha = 2$ or $\alpha = -2$, the Ogden hyperelastic model converts to:

$$W = C_{10}(\vec{I_1} - 3) + C_{01}(\vec{I_2} - 3) + K_1/2 \, (J - 1)^2 \tag{3.21}$$

C_{ij} is mentioned as C_{10}, C_{01} and K_1 are temperature dependent material parameters that can be obtained as follows:

$$\mu_1 = 2C_{10}, \; \mu_2 = 2C_{02}, \; \mu_0 = (\mu_1 + \mu_2), \; \text{and } K_0 = K_1 \tag{3.22}$$

Due to higher water content, soft biological tissue is considered as nearly incompressible material and the Jacobian (J) is equal to 1, hence the last term vanishes.

$$W = C_{10}(\vec{I_1} - 3) + C_{01}(\vec{I_2} - 3) \tag{3.23}$$

Among other constitutive models, the Mooney-Rivlin and Ogden models are the most favored ones. The hyperelastic parameters in these two models can be estimated experimentally

Chapter 3: Development and Validation of Numerical Model

through data fitting [14]. For cases with a large number of parameters, the fitting method can be complicated [25].

3.3.2 Choice of hyperelastic model

The choice of the most appropriate hyperelastic material model depends on the accuracy of the experimental setup and results, stability of the material model and convergence of the FE analysis.

The fitting of experimental data on the basis of optimization algorithm is not straight forward. Ogden et al. investigated three separate forms of strain-energy function based on principle stretches and mentioned two difficulties (a) relative errors propagated in the fitting process and (b) the existence of multiple sets of optimal material parameters for the same data sets. This multiplicity of extracted material properties can lead to very different numerical solutions for a given boundary-value problem [145]. Furthermore, difficulties involved in the fitting procedure are intrinsic to the problem in hand and are not dependent on the specific choice of constitutive law [145].

As soft biological tissues are anisotropic and inhomogeneous, it can be hypothesized that there is no universally accepted model for hyperelastic soft tissue behavior. Also, as the Ogden hyperelastic model works with the principal stresses and provides accurate optimization in curve fitting, this model is chosen for the development of the optimization algorithm used in this work as shown in Figures: 3.1 and Figure: 3.2.
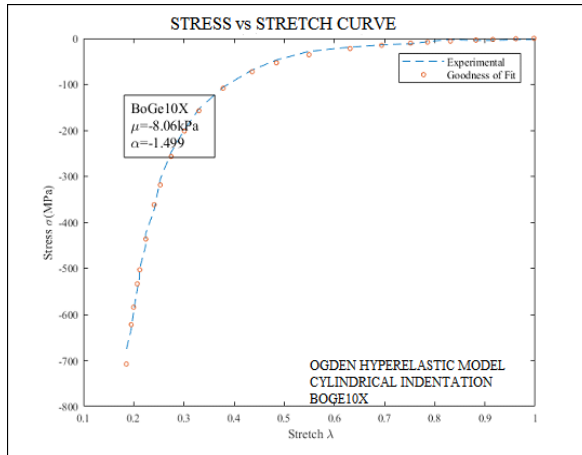
Figure 3.1: Experimental vs fitted stress-stretch curve (BoGe10X). Optimization techniques provide accurate parameter estimation. [26].
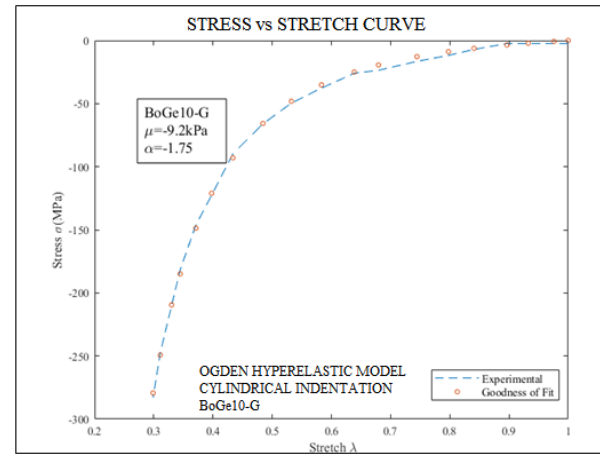
Figure 3.2: Experimental vs fitted stress- stretch curve (BoGe10-G). Optimization techniques provide accurate parameter estimation. [26].

3.4   Application of Ogden Model

3.4.1 Inverse Algorithm

To estimate soft tissue hyperelastic parameters using indentation experimental data, inverse problem analysis is used. In the context of this work, the inverse problem is nonlinear, which can be solved using optimization. In this work, an optimization algorithm was developed where the cost function to be minimized is the difference between experimental force-displacement data and corresponding data obtained from FEM simulation of the indentation test [129].

3.4.2 Optimization Method

The optimization algorithm developed in this work calculates a set of hyperelastic parameters that lead to best fit between experimental and FE generated force-displacement data. It uses inverse approach to minimize an objective function formed based on this criterion with respect to the unknown constitutive parameters [26].

Chapter 3: Development and Validation of Numerical Model

The parameter estimation procedure consists of the following three steps: (i) Record the mechanical responses of soft tissues whose hyperelastic parameters are to be determined; (ii) con- struct corresponding finite element model; and (iii) minimize error (cost) function that quantifies the deviation of the numerical model predicted data from the experimental data [94, 157]. An optimization algorithm is developed in conjunction with MATLAB for calculating the unknown parameter (μ, α).

Let us consider $\Lambda = [\Lambda_1, \Lambda_2, \ldots \Lambda_m]^{\mathrm{T}}$ are vector values of deformation, and $[\tau = \tau_1, \tau_2 \ldots \tau_m]$ are the corresponding values of stress. (Λ, τ) are the given pair of data values. Ogden strain energy function (W) is considered for stress calculation and written as $F(\Lambda, Q) : \mathbb{R} X \mathbb{R} \rightarrow \mathbb{R}n$, where, Λ takes values Λ_i, $1 = 1 \ldots m$ and $Q = [Q_1, Q_2, Q_3 \ldots Q_n]^{\mathrm{T}}$ is a set of n material parameters to be identified. The object function is defined as the squared 2-norm to be minimized [121]

$$S_F(\mathbf{Q}) = \|F(\Lambda, \mathbf{Q}) - \tau\|_2^2 = \sum_{i=1}^{m} [F(\Lambda, \mathbf{Q}) - \tau_i]^2 \tag{3.24}$$

where $F(\Lambda, Q) := [F(\Lambda_i, Q), \ldots\ldots, F(\Lambda_m, Q)]^T$. Using Equation: (3.24) we can conduct sensitivity analysis for the Ogden strain energy function [151]:

$$\sigma = \sum_{i=1}^{N} \mu_i(\lambda^{\alpha_i} - \lambda^{-\alpha i/2}) = F_S(\lambda, \mathbf{Q}) \tag{3.25}$$

Here we use the MATLAB built-in function fminsearch optimization Toolbox to run an iterative optimization algorithm until the objective function is minimized. There are many optimization algorithms available in the literature based on slight modification of Newton-Raphson iterative technique [121]. A number of researchers have published methods of material characterizations from soft biological tissues as discussed previously.

Fellay et al. tackled the problem of characterizing material properties from gelatin gel. They found difficulties in choosing the right hyperelastic model [26]. They used the spherical indentation test for measuring the load displacement curve. The FE simulated load-displacement data of different stiffness values 0.06 to 55 kPa were inserted into the MATLAB optimization

Chapter 3: Development and Validation of Numerical Model

algorithm for parameter estimation. The parameters obtained using their work for hydrogel (μ = 3.67 kPa, α = −6.67) matches reported data provided by Gamonpilas et al. (μ = 3.1 kPa, α = −6.2) [11].

The optimization process uses global or local minimization method for parameter estimation. Starting with an initial guess for the unknown hyperelastic parameters, these parameters are input in the tissue specimen FE model. The FE model leads to tissue response (e.g. indentation force-displacement) which is compared to the experimental data. Comparison process determines the value of the object function $O(\hat{\mathbf{p}})$ for the actual set of target parameters $\hat{\mathbf{p}}$ at the respective iteration step. The target parameter vector p is updated based on the optimization algorithm to find an improved estimate that reduces the objective function. This process is repeated until an optimal set of hyperelastic parameters are found that lead to best matching between experimental and simulated data. The object function $O(\hat{\mathbf{p}})$ is equal to the sum of the squared normalized element of the residual vector [26]:

$$O(\hat{p}) = \frac{1}{2} \sum_{i=1}^{m} r_i(p)^2 = \frac{1}{2} r(p)^T r(p) \tag{3.26}$$

It was reported that the accuracy of the constitutive parameter (μ, α) depends on the initial guess of the optimization process (μ_0 *and* α_0).

3.4.3   Trust Region Approach

The Levenberg-Marquardt algorithm works with optimal parameter vector p iteratively, and an iteration counter k is implemented. In the iteration step k a correction $\Delta p^{(k)}$ to the actual parameter vector $p(k)$ is estimated. The quadratic model $\tilde{O}(p^{(k)})$ of the object function is approximated by Taylor series expansion as follows:

Chapter 3: Development and Validation of Numerical Model

$$O(p^{(k)} + \Delta p^{(k)}) \approx O(p^{(k)} + \Delta p^{(k)}) \tag{3.27}$$

Where

$$O(p^{(k)} + \Delta p^{(k)})) = O(p^{(k)} + \Delta p^{(k)T} \Delta Op^{(k)} + \frac{1}{2} \Delta p^{(k)T} [\ ^2Op^{(k)}] \Delta p^{(k)} \tag{3.28}$$

For zero, first and, second order derivatives of $Op^{(k)}$ introduced at point p^k. A more realistic approach is to define some neighbourhood Ω of $p(k)$ to minimize $O(p^{(k)} + \Delta p^{(k)})$. This approach is known as the trust region approach [22]. The optimization problem is solved by quadratic model $\widetilde{O}(p^{(k)} + \Delta p^{(k)})$ not for the object function $\widetilde{O}(p^{(k)} + \Delta p^{(k)})$.

minimize $\widetilde{O}(p^{(k)} + \Delta p^{(k)}$ subject to

$$\|\Delta p^{(k)}\| \leq (\Delta h^{(k)}) \tag{3.29}$$

After identifying the optimal Ogden hyperelastic material properties, a parametric analysis is performed to evaluate the model's sensitivity to the Ogden material properties (μ, α) perturbing each parameter by $\pm(1\%)$. Fellay et al. also reported that only α is sensitive to material properties [26].

3.5   Axisymmetric Indentation Model

Commercial finite element modeling software package, Abaqus is used to develop the 2D axisymmetric rigid, flat-ended, cylindrical indentation model. The radius of the indenter a is used to indent a test specimen of thickness h. Cylindrical polar coordinates are (r, θ, z) are used as the indenter axis coincides with the z-axis, r is perpendicular to z, and θ represents the angular distance between a reference line and r.

For an isotropic elastic half-space, the axisymmetric displacement field $w(r)$ is chosen in $\theta = 0$ plane with two degree of freedom (DOF). The test sample is bounded on the equipment surface, and shear traction between the indenter and test sample are assumed to be negligible. During simulation, the initial elastic modulus, $E = 0.1$ kPa, and Poisson's ratio, $\upsilon = 0.499$ is considered. This model is developed for the characterization of soft tissue phantoms.

Chapter 3: Development and Validation of Numerical Model

3.5.1 Choice of Element Type

Depending on the type of applications from simplest to complex FE simulations have been categorized as (2*D*) element shown in Figure 3.3.
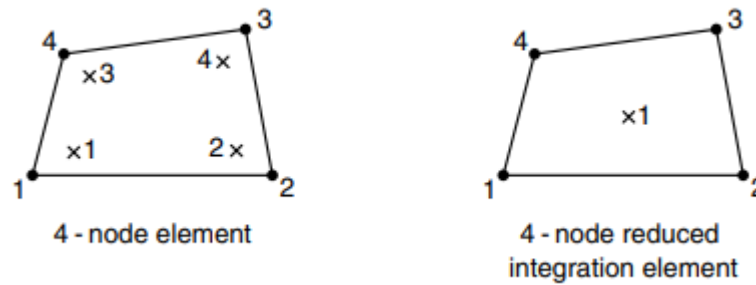
Figure 3.3: Schematic of the 2D element used in FEA for solving solid mechanics problems [35].

Each element is determined based on family, number of nodes, degree of freedom, formulation and integration. 'Full integration' refers to elements utilizing standard number of numerical integration points within FE element to obtain accurate integration involved in the elements' stiffness matrix calculation. 'Reduced integration' is one order less than the 'full integration' rule. 'Reduced integration', linear elements have a smaller number of integration points within each finite element, leading to significant reduction of CPU calculation time at the expense of some accuracy.

In this dissertation, models utilized FE with reduced integration. The mesh density is maximized (refined) in the vicinity of the indenter and test specimen and gradually decreased out- side the contact region. At least 7600 (CAX4RH) quadratic elements were generated in the meshing process for all of the finite element simulations. Fine FE meshing was used underneath the indenter to overcome the effect of hourglass during simulation.

Chapter 3: Development and Validation of Numerical Model

3.5.2 Discretization of the Domain

Before mesh generation, the domain was divided in many subunits and each one is called element. For the case of iso-parametric element, each element has a local coordinate system called natural coordinates. Using the same shape functions the element geometry can also be mapped. Let us consider ξ_1, ξ_2, ξ_3 as the natural coordinates and n is the number of nodes. The shape function can be explained as

$$X = \sum_{a=1}^{n} N_a(\xi_1, \xi_2, \xi_3)X_a \tag{3.30}$$

The motion of the body is presented in terms of $x_a(t)$

$$x(t) = \sum_{a=1}^{n} N_a(\xi_1, \xi_2, \xi_3)x_0(t) \tag{3.31}$$

Other solution fields such as displacement, velocity virtual velocity, can also be expressed using the shape functions (ABAQUS User's Guide Vol. 5, 2013)

3.5.3 Mesh Design

Mesh generation is an extended discretization process that provides control to converge a solution accurately. Changing grid density is the fine-tuning tool that makes the optimum balance between computation and the accuracy of the solution. The cylindrical indenter used in FE simulation is perfectly rigid, hence is modeled as an analytically rigid body. A rigid body reference point is assigned on the tip of the indenter for the translations of variables on a single node. A typical meshing of the specimen for spherical indentation and meshing of the specimen for uniaxial indentation are shown in Figure: 3.4 and Figure: 3.5.

Chapter 3: Development and Validation of Numerical Model
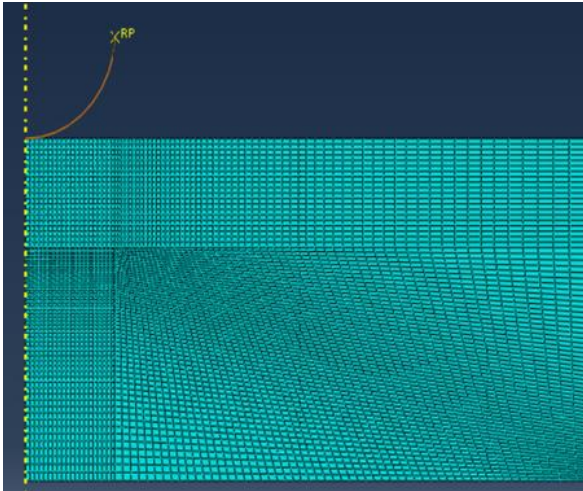
Figure 3.4: Meshing of the specimen for spherical indentation. 7600 (CAX4RH) elements were generated in the meshing process [36].
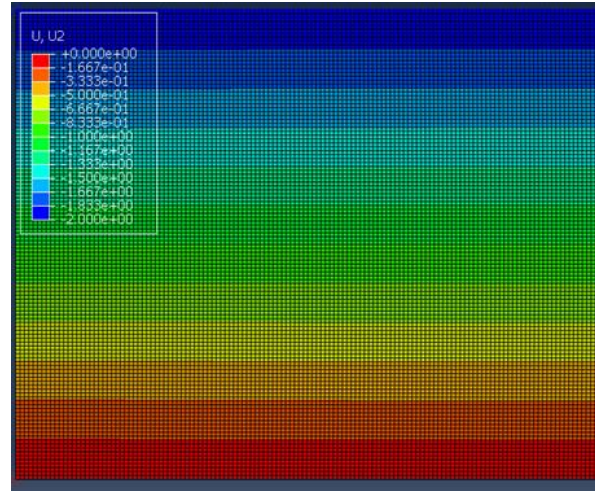
Figure 3.5: Meshing of the specimen for uniaxial indentation. 11000 (CAX4RH) elements were generated in the meshing process.

Four-nodded axisymmetric linear quadrilateral elements are utilized. Reduced integration was employed to reduce computation time. Abaqus used axisymmetric, first order, four-noded bilinear, reduced integration with hourglass control 'CAX4RH'continuum element respectively. The indentation problem was modelled using contact mechanics where the rigid surface (indenter) was considered as master surface and the surface of the soft tissue is considered as slave surface in a contact pair. To have a better understanding about the deformation pattern, bias element distribution was implemented. Very fine mesh was used underneath the master surface, and 5% bias ratio was introduced to decrease the grid density from finer to coarser for the area farther from the indenter.

3.5.4 Indenter-Specimen Interaction

Indentation deals with the theory of contact problem. There are two kinds of contact interaction (i) interaction normal to the surface and (ii) tangential to the surface. Contact pair interaction between master and slave surface is shown in Figure: 3.6 and 3.7.

Chapter 3: Development and Validation of Numerical Model
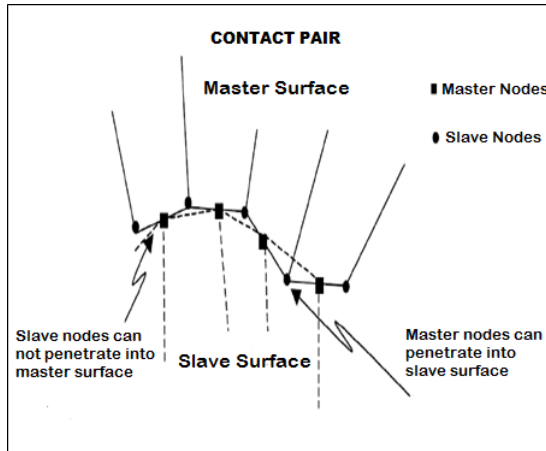
Figure 3.6: Schematic showing the master and slave surface and penetration restriction be- tween the two surfaces (ABAQUS User's Guide Vol. 5, 2013)
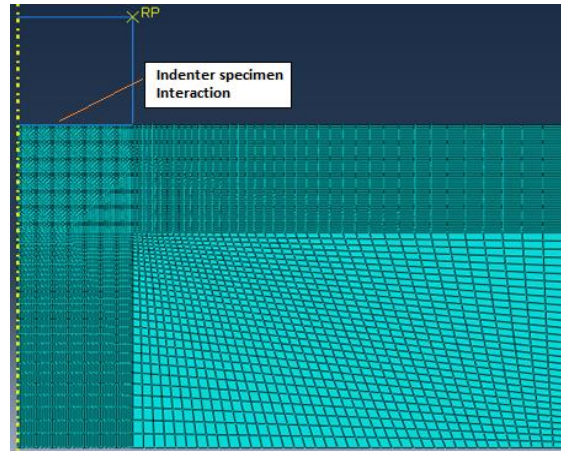
Figure 3.7: Schematic of the master and slave surface, where the interaction between surface and node was observed during FE simulation (Abaqus).

Based on the definition of contact region in Abaqus manual, the normal component uses contact pressure on soft tissue. Rigid cylindrical indenter is chosen as the master surface and the soft tissue as the slave where the nodes on the two contacting surfaces are grouped together to create master and slave surfaces. In order to formulate interaction property surface-to-surface interaction the contact formulation Abaqus used Coulomb friction in the simulation. The rigid indenter and the soft tissue mimic were adjusted in such a way that contact region has zero clearance and acts as an initial condition before the application of load. The process was completed by specifying an "adjustment zone" in Abaqus. The "hard" contact relationship was introduced to define the normal contact that restricts the penetration of the slave surface into the master surface at the constraint locations. The coefficient of friction between the master and the slave surface can be changed according to the choice of interest.

3.5.5 Effect of Coefficient of Frictions

Together, the indenter and soft tissue were treated as a contact pair. The indenter is specified as master surface and the soft tissue slave surface. Coefficient of friction between the contact pair has been reported by others with a wide range [94]. As second order elements can cause problems in contact simulation, first-order elements were selected to form the slave surface.

Chapter 3: Development and Validation of Numerical Model

Schematic of indenter to node interaction where friction coefficients are in effect and FE simulated load-displacement contours plot shown in Figure: 3.8 and Figure: 3.9.
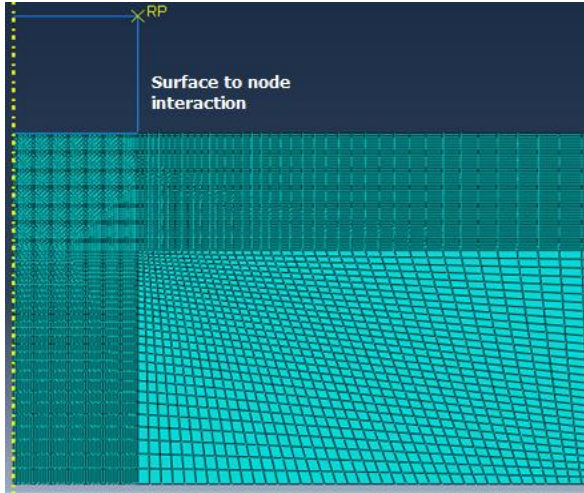
Figure 3.8: Schematic of the slip region where friction of coefficient is introduced between surface to node interaction
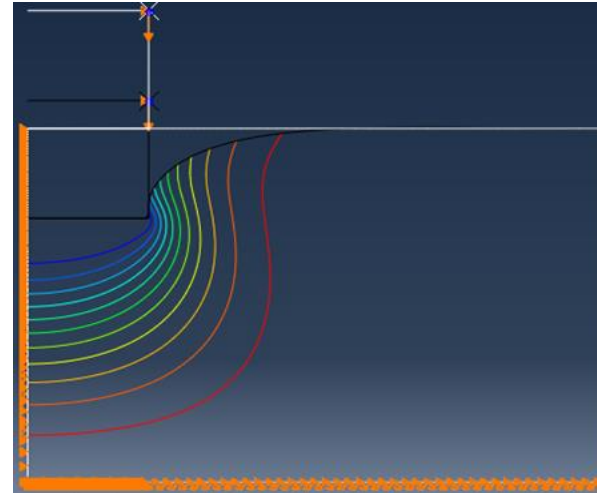
Figure 3.9: Schematic of FE simulated load-displacement contours plot at aspect ratio a/h=8, zero friction coefficient and Poisson's ratio of 0.5.

Friction coefficient plays an important role in numerical simulation. Many researchers paid special attention to frictionless interface between indenter and test samples in FE simulation [25, 139]. Cao et al. showed a correlation between the indenter radius to thickness ratio and the effect of friction in two different friction coefficients [30]. Also, Zhang et al. reported the effect of friction on the calculation of tissues, cryogel's Young's modulus [25]. In order to investigate the effect of friction on polyvinyl alcohol cryogel (PVA-C), a number of friction coefficients have been introduced in simulation as follows: 0.05, 0.1, 0.2, 0.3, 0.4, 0.5 etc. Marteau et al. discussed the influence of friction coefficient and identify optimized friction coefficient for numerical analysis [99].

3.5.6 Boundary Condition and Applied Load

Boundary condition is applied to the specimen to prevent rotation and promote normal translation. In order to prevent rigid body motion, it is necessary to apply constraints. For an

Chapter 3: Development and Validation of Numerical Model

axisymmetric model roller boundary condition is introduced along the symmetry of axis which only allows translation in vertical direction. The nodes at the bottom and right side of the mesh are fixed. In order to avoid boundary effect soft tissue mimic, the aspect ratio of indenter radius to specimen size was validated beforehand. Load control method was introduced where a concentrated force of 0.6 kN was applied on the top of the analytical rigid indenter. The boundary conditions underneath the indenter towards the z direction at the test specimen are shown in Figure: 3.10 and Figure: 3.11.
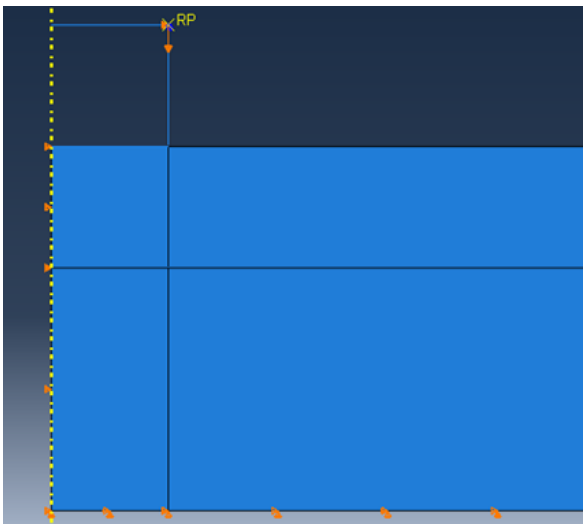
Figure 3.10: Schematic of FEA (produced by Abaqus) for cylindrical indentation.
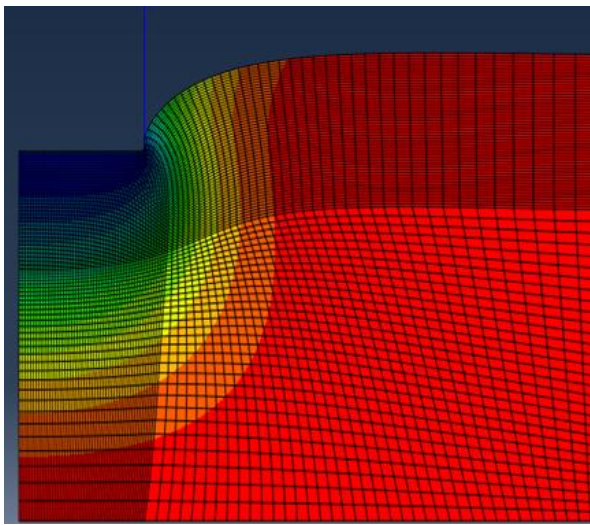
Figure 3.11: Schematic of 7600 CAX4RH element mesh for cylindrical indentation.

Case 1: There is no normal stress acting on the free surface outside the contact region σ_z.

$$u_z(r, 0) = h; \ 0 \leq r < a \tag{3.32}$$

Case 2: The contact region between the indenter and the elastic half space (test specimen) are frictionless.

$$\sigma_z(r, 0) = 0; \ r > a \tag{3.33}$$

Case 3: The force should be consistent for displacement in the z direction u_z. Due to sharp edge of the cylindrical indenter $\sigma_z \rightarrow \infty$, when r = a.

$$\sigma_{rz}(r,\ 0) = 0;\ \ r \le a \qquad\qquad (3.34)$$

3.6   Validation of the Finite Element Model

The nature of the stresses arising from the contact between two elastic bodies is of considerable importance and was first studied by Hertz [31, 45]. To examine the suitability of finite element model assumptions and the simulated results and to implement physical model in real biomedical applications, model validation is necessary [158]. Boussinesq first investigated the problem associated with the distribution of stress within an elastic half space when it is deformed by the normal pressure against its boundary of a rigid punch [28]. He used potential theory to solve this problem, and one of the cases was flat-ended cylindrical punch [48]. For validation, the FE solutions pertaining to linear elastic model for the displacement and stress are compared with Hertz, Boussinesq, Sneddon's elastic analysis [25, 28].

3.6.1   Mesh Refinement

Convergence analysis of the numerical solution was assessed for solving two-point boundary value problems and to minimize truncation error [159]. Accuracy in FEA depends on (i) the number of gaussian points involved in numerical integration, (ii) the number of elements involved in discretization, and (iii) the number of integration points used in the numerical experiment. In FE analysis, contact detection includes the definition of two elements: indenter as a master surface and soft tissue as a slave surface. Accuracy of a numerical solution depends on choosing appropriate mesh through mesh refinement process [160].

To obtain accurate detection of the contact between indenter and soft tissue the grid density of the indented area must be high [99]. The convergence for each thickness and friction coefficient are shown Figure: 3.12 and Figure: 3.13.

Chapter 3: Development and Validation of Numerical Model
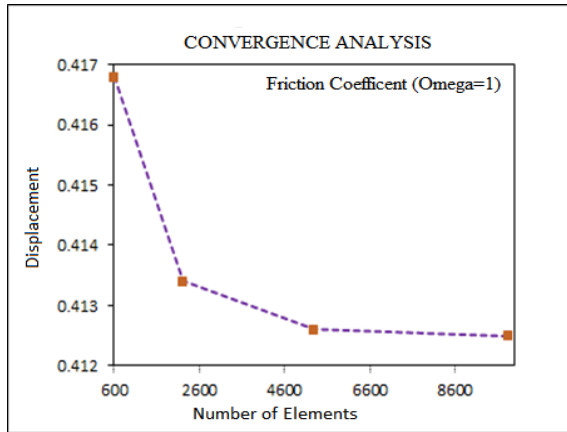
Figure 3.12: FE simulated displacement at different number of elements for infinite thick model. Solution converges after mesh refinement process.
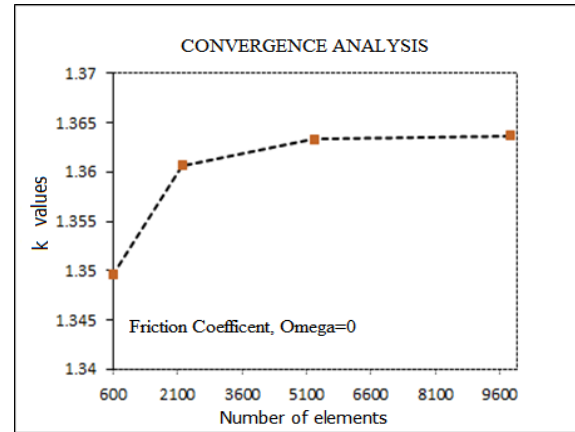
Figure 3.13: FE simulated displacement with different number of elements for finite thick model. Solution converges after mesh refinement process.

Accurate meshing confirms convergence and accuracy of numerical results that is mesh refinement and element size. If coarse grid density is considered, solution will not be accurate [99]. It can be concluded that element size is inversely proportional to the number of discretized elements. In order to have a converged solution the number of discretized elements must be increased to a certain degree, but beyond some point further refinement, does not improve accuracy appreciably [160].

A fully non-linear finite element analysis was conducted for indentation simulation to obtain simulated response. Numerical studies are accomplished to examine the effect of indenter geometry and materials stress-strain pattern on the load-displacement output [161]. A test specimen of thickness 0.4 to 20 mm and axial length of 25 mm used to validate FE simulated analysis.

The axisymmetric finite thickness isotropic FE models consist of three-nodded (CAX3) and four-node (CAX4RH) quad element (bilinear axisymmetric, quadrilateral, reduced integration, hourglass control). Static, general. non-linear geometry, equal step size 0.01 to a maximum 100 number of increments used in each analysis step. Direct method equation solver and full Newton-Raphson technique was utilized in the simulation. Finite sliding, surface-to-surface contact discretization, and single configuration with no slave adjustment methods were

Chapter 3: Development and Validation of Numerical Model

initiated in the interaction process. A mesh convergence analysis was performed to determine that an adequate number of nodes and elements are present in the simulation.

3.6.2 Validation with Hertz Theory of Elastic Indentation

The solution for stress analysis problem between two elastic bodies placed in a mutual contact was first developed by Hertz [31]. His approximation assumptions are known as Hertz theory of elastic indentation which are stated below: [45]:

1. The displacements and stresses must satisfy the differential equations of equilibrium for elastic bodies and the stresses must vanish at a great distance from the contact surface.

2. The contact between the bodies are frictionless.

3. At the outer surface of the body the normal pressure is assumed to be zero at the point of contact, and it is equal and opposite.

4. The inner surface distance between the two bodies is zero at the outer surface of contact is greater than zero.

5. The total distribution of pressure within the circle of contact provides the force acting between the two bodies.

3.6.2.1 Stress Field for Spherical Indenter

The normal pressure distribution directly beneath a spherical indenter of radius a is given by Hertz:

$$\frac{\sigma_z}{P_m} = -\frac{3}{2}\left(1 - \frac{r^2}{a^2}\right); \quad r \leq a \tag{3.35}$$

The pressure distribution $\sigma_z = 1.5P_m$ is a maximum at the center of contact and is zero at the edge of the contact circle. Outside the contact circle, the normal stress σ_z is zero. The

Chapter 3: Development and Validation of Numerical Model

displacement of points on the surface of the specimen within the contact circle, measured with respect to the original specimen free surface [31, 45] is:

$$U_z = \frac{1 - v^2}{E} \ \frac{3}{2} \frac{\pi}{4a} \ (2a^2 - r^2 \ ); \ \ r \leq a \tag{3.36}$$

And outside the contact circle is:

$$U_z = \frac{1 - v^2}{E} \ \frac{3}{2} \frac{1}{2a} \left[(2a^2 - r^2 \ ) \sin^{-1} \left(\frac{a}{r} \right) + ar \left(a - \frac{a^2}{r^2} \right) \right]^{1/2} \tag{3.37}$$

Equation (3.36) shows that the depth beneath the original surface of the contact circle (at r/a = 1) is exactly one-half of the total depth at r = 0, which indicates that the surface deformation mode is always sinking-in for pure elastic materials.

3.6.2.2 Stress Field for Cylindrical Indenter

The stress field created by a cylindrical flat punch is very similar to Hertzian stress field for a spherical indenter. Cylindrical indentation is preferred over the spherical indentation because the contact radius of the cylindrical indenter is fixed. However, the sharp edge of the cylindrical punch indenter may create a stress singularity at the edge, leading to plastic deformation and tissue damage. The distribution of pressure beneath the rigid cylindrical flat punch is calculated based on the superposition of Boussinesq's stress field equation as given below:

$$\frac{\sigma_z}{P_m} = -\frac{1}{2} \left(1 - \frac{r^2}{a^2} \right); \quad r \leq a \tag{3.38}$$

Here, $\sigma_z = 0.5 \ P_m$ is a minimum at the center of contact and approaches infinity at the edge. Outside the indenter, $\sigma_z = 0$ throughout the surface. Beneath the indenter, U_z is the penetration depth beneath the original specimen free surface [31].

$$U_z = \frac{1 - v^2}{E} \ \frac{a\pi}{2} P_m; \quad r \leq a \tag{3.39}$$

Chapter 3: Development and Validation of Numerical Model

when, r is independent and outside the contact circle, the normal displacement is given below [28, 31]:

$$U_z = \frac{1 - \nu^2}{E} P_m a \sin^{-1}\left(\frac{a}{r}\right); \quad r > a$$

(3.40)

Sneddon's equations are used to solve Boussinesq's problem. Also plots of stress components obtained from FE simulation are provided below in Figure: 3.14 and 3.15.
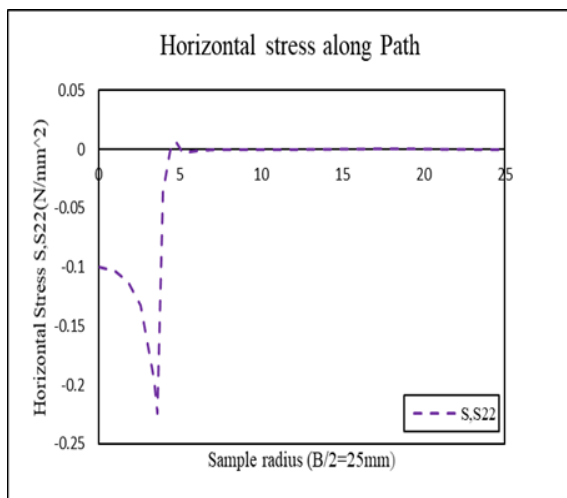
Figure 3.14: Horizontal stress distribution vs specimen radius (25 mm) for linear elastic model.
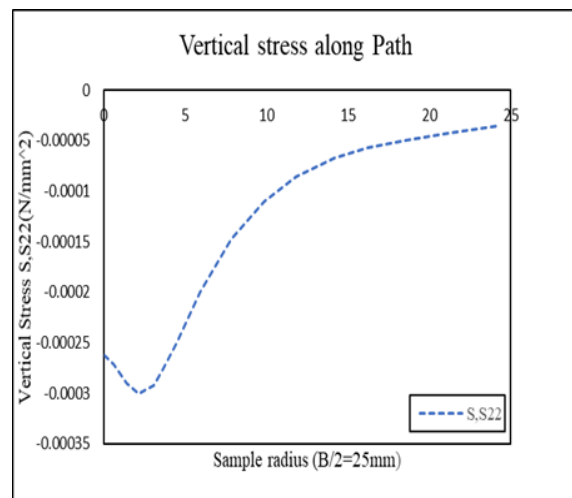
Figure 3.15: Vertical stress distribution vs specimen radius (25 mm) for linear elastic model.

3.6.3 Validation with Boussinesq's Solution

Boussinesq developed the solution for vertical stresses below (a) the center (b) at any point (c) the edge (d) or, any type of circular loaded area under semi-infinite medium assumption.

(a). Vertical stress below the center of a uniformly loaded circular area

From Boussinesq's equation for a uniform surface pressure the compressive stress at a depth h beneath the center line is given by:

Chapter 3: Development and Validation of Numerical Model

$$\sigma_z = P \left\{ 1 - \frac{1}{\left(1 + \left(\frac{a}{h}\right)^2\right)^{3/2}} \right\} \qquad (3.41)$$

where, P is the uniform pressure over a circular area. A typical stress distribution at points below a load distributed over a circular area was given by Ahlvin and Ulery [37] as shown in Figure: 3.16 and Vertical stress below the center of the uniformly loaded circular area as a function of sample aspect ratio is also shown in Figure: 3.17.
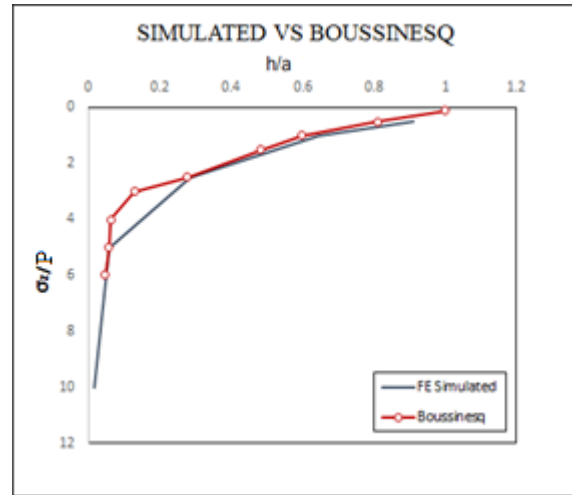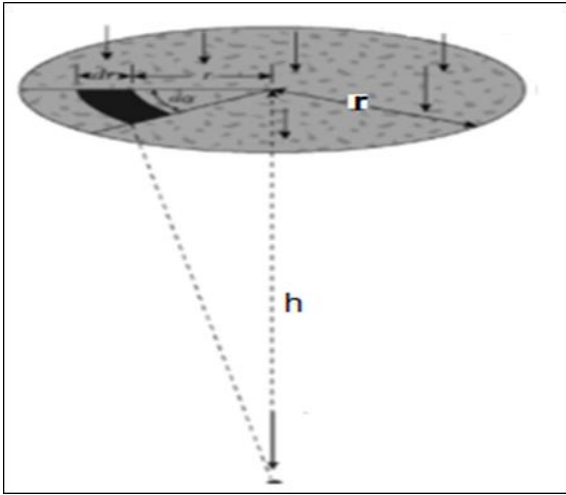
Figure 3.16: Vertical stresses at a point below a load uniformly distributed a circular area [37].

Figure 3.17: Variation of vertical stress vs sample aspect ratio analytical vs simulated data shown in Table 3.1.

Table 3.1: Simulated vertical stress data obtained from different aspect ratio's and Boussinesq's stress equation

a	h	a/h	h/a	σ_h	σ_h/P
mm	mm	mm		kN/mm^2	FEA
4	2	2	0.5	0.546334369	0.910557281
4	4	1	1	0.387867966	0.64646609
4	10	0.5	2.5	0.170674948	0.284458247
4	20	0.2	5	0.034280379	0.057133966
4	40	0.1	10	0.008888798	0.014814663

Chapter 3: Development and Validation of Numerical Model

(b). Vertical deformation under uniformly loaded circular area

Boussinesq equation for vertical deformation in this case of a uniform pressure p applied over a circular area of radius r is given by :

$$\Delta_h = Pr\,\frac{2(1 - v^2)}{E}I_F$$

(3.42)

Table 3. 2 Analytical vertical deformation obtained from Boussinesq's deformation equation and compared with FE simulated results.

According Boussinesq [27]:	Influence Factor	Influence Factor
	At the center	At the Edge
$P = \frac{q}{\pi r^2} = 0.011937$ kN/mm^2 E = 0.1 kPa r = 4 mm v = 0.4999.	$I_C = 1$	$I_E = 0.637$
Boussinesq's analytical solution	$\Delta_{Bous} = 0.4870$mm	$\Delta_{Bous} = 0.310226$ mm
Present FE simulated solution	$\Delta_{FE} = 0.4426$mm	$\Delta_{FE} = 0.308406$ mm

(c). Vertical stress at any point below a uniformly loaded circular area

Vertical stress below a uniformly loaded flexible circular area was given by Ahlvin and Ulery [37]. A detailed calculation for vertical stress located at a depth z at any distance s from the center of the loaded area is given by:

$$\sigma_h = P(A' + B')$$

(3.43)

Where, A', B' are the functions of *s/b* and *z/b* detailed in tables provided in the Appendix.

σ_I : Vertical stress at point I

σ_{II} : Vertical stress at point II

σ_{III} : Vertical stress at point III q : Uniform circular load

A', B' : Partially influence factor which depend on, (*z/b*, *s/b*)

Chapter 3: Development and Validation of Numerical Model

P=Force/ πb^2 = 0.01193659282

Vertical stress at any point below a uniformly loaded circular area and its FE simulation are shown in Figure: 3.18 and Figure: 3.19.
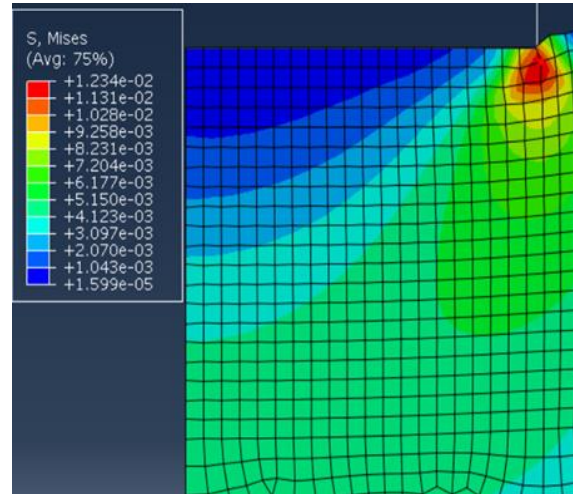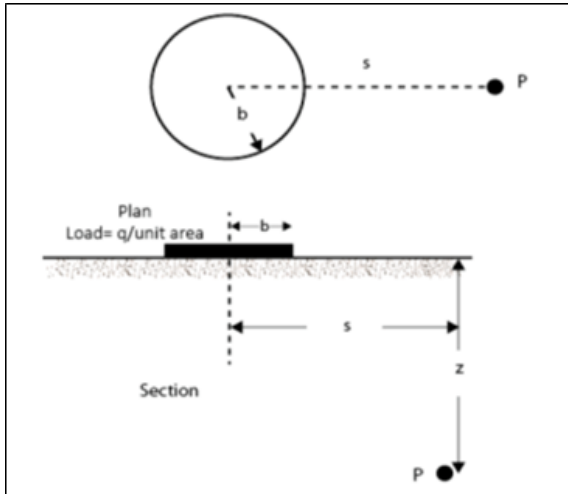
Figure 3.18: Schematic of vertical stress at any point below a uniformly loaded circular area [31].

Figure 3.19: Axisymmetric FE model with fine grid density underneath the indenter surface.

Table 3.3: Boussinesq's analytical and simulated vertical stress.

	s/b	z/b	s/b	z/b	s/b	z/b		Vertical Stress	Analytical (kN/mm^2)	FEA
	0	0.2	1	0.2	1.5	0.2	(I).	$\sigma_I = P(A^{'} + B')$	0.011846	0.0153342
A,	0.80388	0.38269		0.05251			(II).	$\sigma_{II} = P(A^{'} + B')$	0.005584	0.00603391
B,	0.18857	0.08519		0.04448			(III).	$\sigma_{III} = P(A^{'} + B')$	0.000092	0.00001049

Table 3.2: Vertical stress at three points below a uniformly loaded circular area and its FE simulation.

3.6.4   Validation with Sneddon's Solution

For this validation, a number of indentation tests were simulated using the model developed here using FEM and results compared with Sneddon's equation. In the first developed here using FEM and results compared with Sneddon's equation. In the first example the dimensions of the specimen were taken as (25 mm x 12.57 mm). A concentrated load of 0.6 kN was applied

Chapter 3: Development and Validation of Numerical Model

on the top of cylindrical indenter of radius 4mm. The material was considered nonlinear with modulus of elasticity and Poisson's ratio of 0.1 and 0.499 respectively. The FE model consists of 4216 nodes and 4130 elements. FE analysis provides maximum stress value of 0.0326 kN/mm^2 and from Sneddon's equation value of 0.03 kN/mm2 which shows a very good agreement between simulated and calculated results. Schematic of force-displacement contours and stress contours for finite thick (25 mm x 12.57 mm) FE model are shown in Figure: 3.20 and Figure: 3.21.
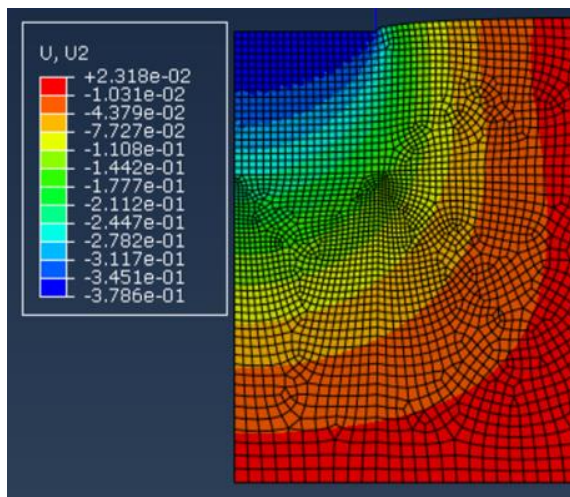
Figure 3.20: Displacement contours of axisymmetric FE simulated finite thickness linear elastic model.
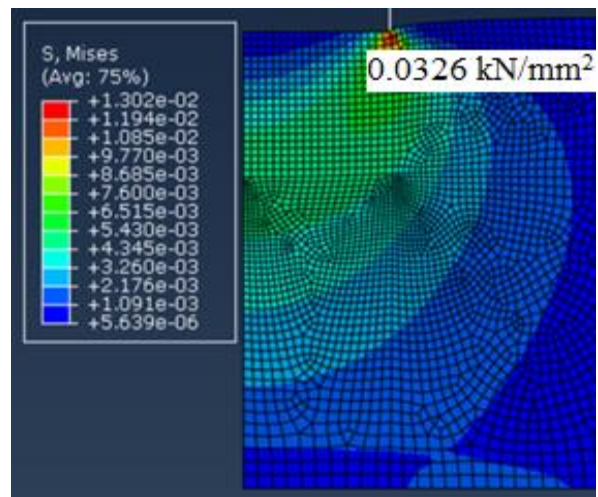
Figure 3.21: Stress contours of axisymmetric FE simulated finite thickness linear elastic model.

In the second example, the dimensions of the specimen were taken as (25 mm x 10 mm). A concentrated load of 0.6 kN was applied on the top of cylindrical indenter of radius 4*mm*. The material was considered nonlinear with modulus of elasticity and Poisson's ratio are 0.1 and 0.49 respectively. The FE model consisted of 6239 nodes and 6134 (CAX4RH) and 105 (CAX3) number of nodes elements. FE analysis led to a maximum stress value 0.0271 kN/mm^2 while Sneddon's equation value 0.02879 kN/mm^2 which shows a very good agreement between simulated and calculated results. Schematic of force-displacement contours and stress contours for finite thick (25 mm X 10 mm) FE model are shown in Figure: 3.22 and Figure: 3.23.

Chapter 3: Development and Validation of Numerical Model
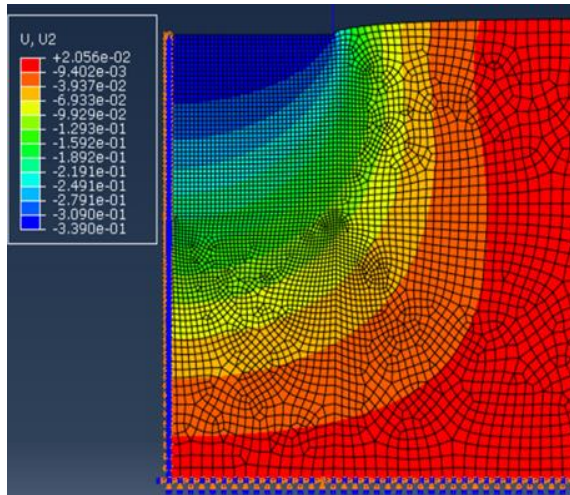
Figure 3.22: Displacement contours of axisymmetric FE simulated finite thickness linear elastic model.
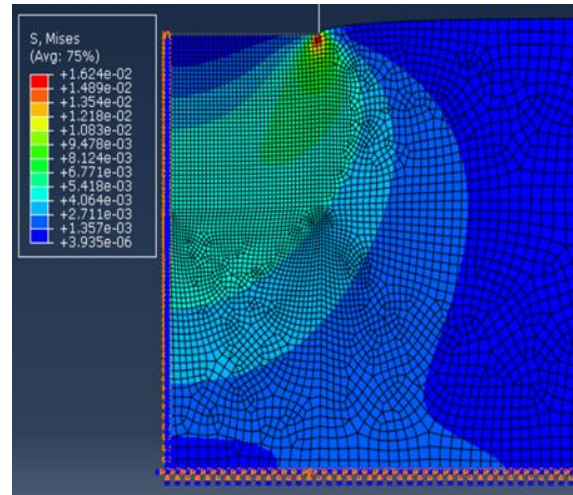
Figure 3.23: Stress contours of axisymmetric FE simulated finite thickness linear elastic model.

In the third example the dimensions of the specimen were taken as (25 mm x 5 mm). A concentrated load of 0.6 kN was applied on the top of cylindrical indenter of radius 4mm. The material was considered nonlinear with modulus of elasticity and Poisson's ratio are 0.1 and 0.499 respectively. The FE model consisted of 6868 nodes and 6690 (CAX4RH) and 178 (CAX3) elements. FE analysis led to a maximum stress value 0.0168 kN/mm^2 while Sneddon's equation led to 0.0118 kN/mm^2. Schematic of force-displacement contours and stress contours for finite thick (25 mm x 5 mm) FE model are shown in Figure: 3.24 and Figure: 3.25.
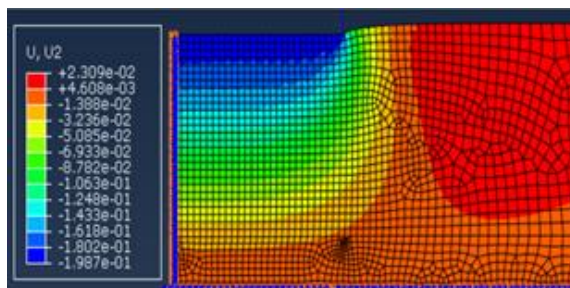
Figure 3.24: Displacement contours of axisymmetric FE simulated finite thickness linear elastic model.
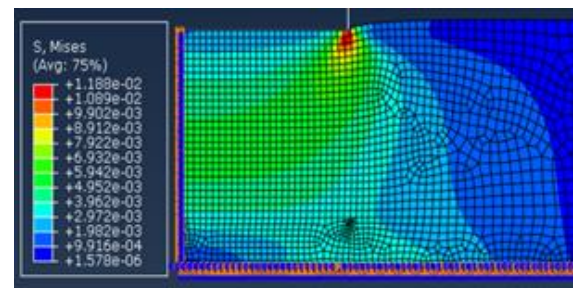
Figure 3.25: Stress contours of axisymmetric FE simulated finite thickness linear elastic model.

Chapter 3: Development and Validation of Numerical Model

In the fourth example the dimensions of the specimen were taken as (25 mm x 4 mm). A concentrated load of 0.6 kN was applied on the top of cylindrical indenter of radius 4mm. The material was considered nonlinear with modulus of elasticity and Poisson's ratio are 0.1 and 0.499 respectively. The FE model consisted of 2519 nodes and 2484 (CAX4RH) and 35 (CAX3) elements. FE analysis led to a maximum stress value 0.00268 kN/mm^2 while Sneddon's equation led to 0.0021 kN/mm^2. Schematic of force-displacement contours and stress contours for finite thick (25 mmX4 mm) FE model are shown in Figure: 3.26 and Figure: 3.27.
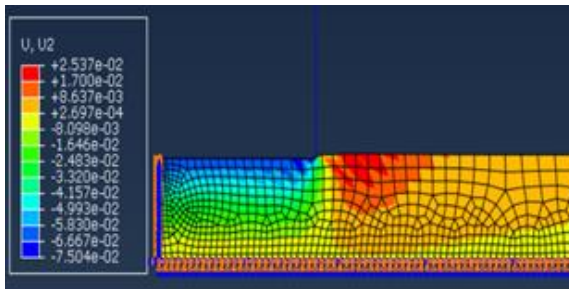
Figure 3.26: Displacement contours of axisymmetric FE simulated finite thickness linear elastic model.
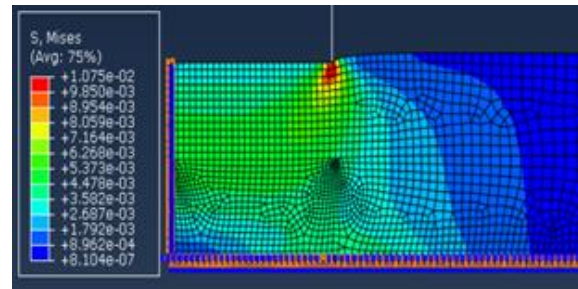
Figure 3.27: Stress contours of axisymmetric FE simulated finite thickness linear elastic model.

In the fifth example the dimensions of the specimen were taken as (25 mm X 2.667 mm). A concentrated load of 0.6 kN was applied on the top of cylindrical indenter of radius 4mm. The material was considered nonlinear with modulus of elasticity and Poisson's ratio are 0.1 and 0.499 respectively. The FE model consisted of 1244 nodes and 1137 (CAX4RH) elements. FE analysis led to a maximum stress value 0.0085 kN/mm^2 while Sneddon's equation led to 0.0082 kN/mm^2.

Schematic of force-displacement contours and stress contours for finite thick (25 mm X 2.667 mm) FE model are shown in Figure: 3.28 and Figure: 3.29.

Chapter 3: Development and Validation of Numerical Model
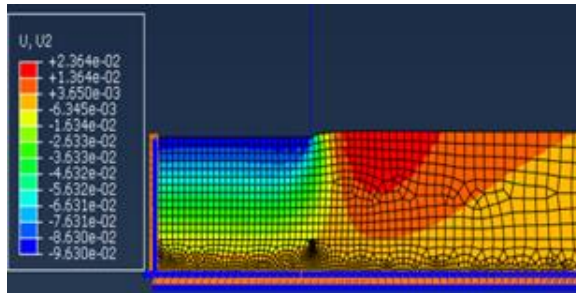
Figure 3.28: Displacement contours of axisymmetric FE simulated finite thickness linear elastic model.
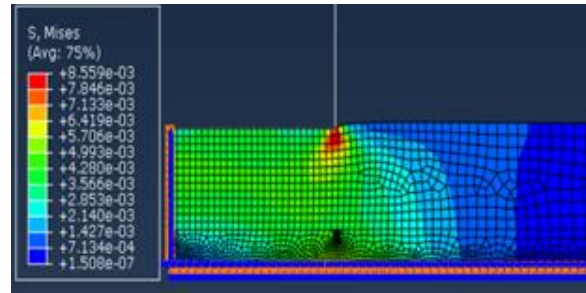
Figure 3.29: Stress contours of axisymmetric FE simulated finite thickness linear elastic model.

In the sixth example the dimensions of the specimen were taken as (25 mm X 2 mm). A concentrated load of 0.6kN was applied on the top of cylindrical indenter of radius 4mm. The material was considered nonlinear with modulus of elasticity and Poisson's ratio are 0.1 and 0.499 respectively. The FE model consisted of 1244 nodes and 1137 (CAX4RH) elements. FE analysis led to a maximum stress value 0.002193 kN/mm^2 while Sneddon's equation led to 0.0021 kN/mm^2. Schematic of force-displacement contours and stress contours for finite thick (25 mm X 12.57 mm) FE model are shown in Figure: 3.30 and Figure: 3.31.
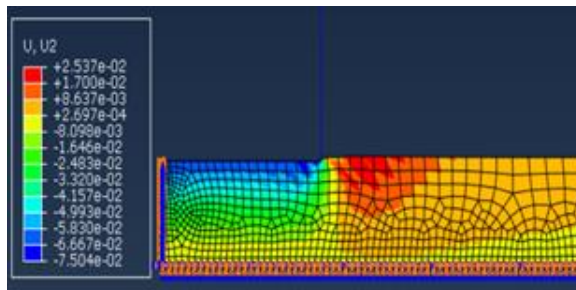
Figure 3.30: Displacement contours of axisymmetric FE simulated finite thickness linear elastic model.
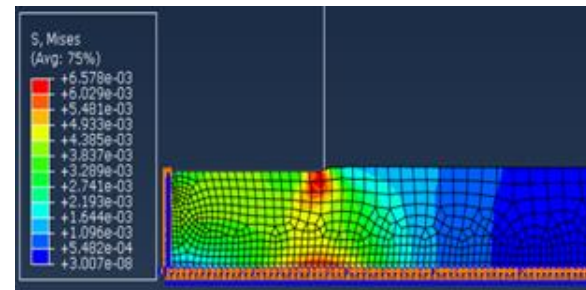
Figure 3.31: Stress contours of axisymmetric FE simulated finite thickness linear elastic model.

In the seventh example the dimensions of the specimen were taken as (25 mm x 0.8 mm). A concentrated load of 0.6kN was applied on the top of cylindrical indenter of radius 4mm. The material was considered nonlinear with modulus of elasticity and Poisson's ratio are 0.1 and 0.499 respectively. The FE model consisted of 1425 nodes and 1245 (CAX4RH) elements. FE analysis led to a maximum stress value 0.001456 kN/mm^2 while Sneddon's equation led to

Chapter 3: Development and Validation of Numerical Model

0.0015 kN/mm^2. Schematic of force-displacement contours and stress contours for finite thick (25 mm x 12.57 mm) FE model are shown in Figure: 3.32 and Figure: 3.33.
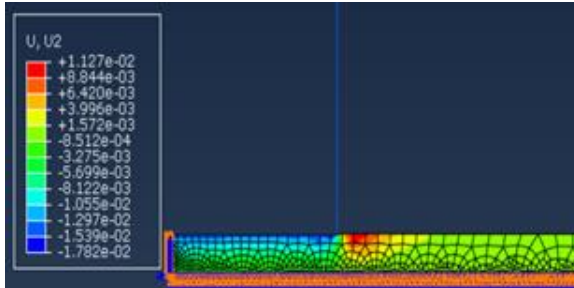
Figure 3.32: Displacement contours of axisymmetric FE simulated finite thickness linear elastic model.
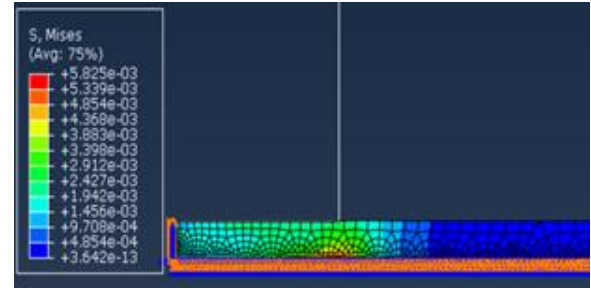
Figure 3.33: Stress contours of axisymmetric FE simulated finite thickness linear elastic model.

In the eight example the dimensions of the specimen were taken as (25 mm x 0.4 mm). A concentrated load of 0.6 kN was applied on the top of cylindrical indenter of radius 4mm. The material was considered nonlinear with modulus of elasticity and Poisson's ratio are 0.1 and 0.499 respectively. The FE model consisted of 2097 nodes and 1813 (CAX4RH) elements. FE analysis led to a maximum stress value 0.00049 kN/mm^2 while Sneddon's equation led to 0.0004 kN/mm^2. Schematic of force-displacement contours and stress contours for finite thick (25 mm x 12.57 mm) FE model are shown in Figure: 3.34 and Figure: 3.35.
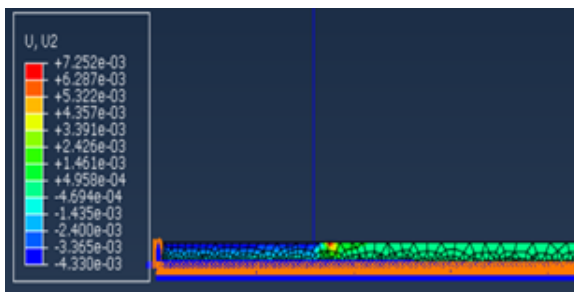
Figure 3.34: Displacement contours of axisymmetric FE simulated finite thickness linear elastic model.
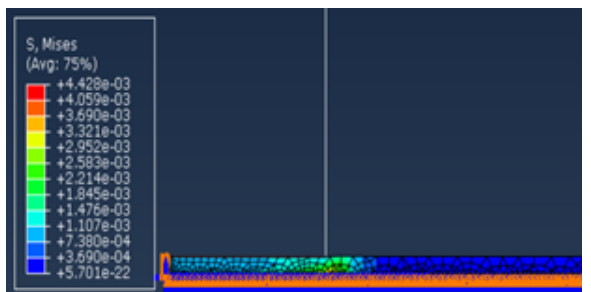
Figure 3.35: Stress contours of axisymmetric FE simulated finite thickness linear elastic model.

3.7 Summary

In this chapter, a two-dimensional axisymmetric numerical model was developed for the cylindrical, spherical indentation and uniaxial testing in the finite element software package Abaqus to study material characterization of nonlinear soft biological tissue phantom (PVA-C). A concentrated load was applied at the top of the indenter's reference point which was also chosen at the right top corner of the indenter. The material (PVA-C) was characterized as nonlinear. To discuss the nonlinearity of this material, two hyperelastic models were discussed in this chapter. Due to nonlinear tissue properties, other, more suitable models were required for further investigation. Ogden and Mooney-Rivlin hyperelastic models were considered to be the most appropriate for this finite element analysis.

At the initial stage of the study, linear elastic models were considered appropriate for the understanding of displacement pattern. Mesh refinement process was adopted for optimal convergence that ensured numerical accuracy. Finite and infinite thickness specimen were considered for FE simulation.

In the validation phase, a series of numerical analysis were conducted using Abaqus to confirm whether simulated results are consistent with Boussinesq's analytical solution. The simulated stress values were compared with Boussinesq's analytical solutions and found good agreement, which were shown in Table: 3.2. Based on Boussinesq's solution, one can evaluate stress at any point within the specimen body. This investigation will help to calculate stresses at any point on a specimen where geometric nonlinearity is considered.

The effect of relative indentation depth, aspect ratio, Poisson's ratio and dimensionless k on the indentation response of soft tissues were investigated. This addition, a new function Ω will be introduced as a function of k (Φ, Ψ, Ω) [25]. At the second stage stress analysis were conducted for linear and hyperelastic model. Furthermore, a validation exercise was conducted using Hayes, Cao's and Zhang's data. Finally, to fulfill the short comings from indenter-specimen interaction, a novel analytical solution will be developed to investigate the material properties of soft tissues. and will be included Chapter 4 of this dissertation.

Chapter 4

Characterizations of PVA-C Material Behavior using Finite Element Method

4.1 Introduction

For the last couple few decades, indentation techniques have played an active role for material mechanical characterization. Analytical solutions for nonlinear elastic materials are not available for finite indentation depth. However, for linear elastic materials, closed form solutions are readily available [95]. Having effective solutions non-linear elastic tissue undergoing indentation testing is very important for various future biomedical applications. Specimen's friction coefficient, displacement influence factor, Poisson's ratio, relative indentation depth, aspect ratio influences the tissue response greatly, and hence should be considered properly in estimating tissue properties. It has been reported by many previous researchers that most pathological tissues stiffer than their healthy tissue counterparts [25, 162]. Flat-ended cylindrical indenter is used in this dissertation to mechanically stimulate finite and infinite thickness soft tissues or mimics (PVA-C) to characterize the non-linear mechanical properties [33].

The main objective of this chapter is to investigate the behavior of non-linear material. This chapter will investigate the following using FEM:

(i) the mechanical properties of Polyvinyl Alcohol Cryogel (PVA-C) using finite and infinite thickness.

Chapter 4: Characterization of PVA-C using Finite Element Method

(ii) validation of Boussinesq's, Sneddon's, Cao's, Zhang's theory of elastic indention and compare their results with the results obtained from this study.

(iii) the effect of displacement influence factor on finite thickness specimens with linear and non-linear elastic model.

(iv) the effect of Poisson's ratio, aspect ratio and relative indentation depth and friction coefficient on PVA material response.

(v) results obtained from the model used in this study and compared their results with previous published works.

The first section of this chapter describes a general technique for solving a linear and non-linear problem using Abaqus. This section also describes convergence and compares between experimental and FE simulated results. The third section of this chapter discusses Hayes, Cao's and Zhang's model. Finally, the fourth section addresses about a novel analytical solution by modifying Zhang's model. This chapter concludes followed by a summary.

4.2 Finite Element Model of Soft Tissues

Commercial FE software package Abaqus was used to create an axisymmetric model for examining indentation. PVA-C was used a soft tissue mimic and a flat ended cylindrical indenter was modeled in this simulation. The contact surface between the indenter and the soft tissue was set as frictionless. Soft biological tissue is generally considered to be as incompressible [39], hence the linear elastic models, the Poisson's ratio and Young's modulus were set as 0.499 and 10 kPa, respectively. A concentrated load of 5 kN was applied on the top of the indenter. For optimal numerical accuracy, high mesh density was adapted underneath the indenter and convergence criteria was verified. Indentation tests were simulated under linear and non-linear hyperelastic model assumptions.

Chapter 4: Characterization of PVA-C using Finite Element Method

4.2.1 FE Mesh Convergence Assessment

Numerical mesh convergence analysis is necessary in any numerical solution used for solving boundary value problems for minimizing model errors [73]. Accuracy of FEA results depends on (i) number of Gaussian points engaged in the FE numerical integration and (ii) number of elements involved in domain discretization. Also, accuracy of a numerical solution depends on choosing the appropriate mesh through a mesh refinement process [160]. Mesh convergence analysis, whereby the size distribution of FE elements is altered until desired accuracy is achieved, is essential to ensure results reliability [163]. Pinyochotiwong et al. reported that, element size is inversely proportional to the number of discretized elements [160]. In order to obtain accurate results in the simulated environment, mesh optimization is critical. The mesh density is maximized (refined) in the vicinity of indenter and gradually decreased outside the contact region. Mesh refinement process is implemented for convergence and finally optimal grid density is chosen for all FE simulations.

In this work, 5346 (CAX4RH) quadratic elements were generated with aspect ratio > 1 for all elements. Average aspect ratio of elements was 1.23 while the least desirable aspect ratio was 2.65. Out of the 5346 elements, 120 of the elements were triangular elements of type (CAX3H) with aspect ratio > 1 with average aspect ratio of 1.27 and highest aspect ratio of 1.84 and shape factor <0.01. The left side of the vertical boundary was subjected to axisymmetric boundary condition U1=U3=UR2=0 which allows the test sample to move only in the vertical direction, and the boundary condition of the bottom and right side was U1 = U2= U3 = UR1 = UR2 = UR3 = 0.

An axisymmetric flat ended cylindrical and spherical indenter was used in this simulation. Very fine mesh was used underneath the indenter region. The contact ratio between the indenter and material was (1:1). Convergence criteria was checked for each thickness. Except for the loading region, the rest of the material was meshed at a 5% bias ratio. Large displacement criteria were also invoked in this analysis. For a nonlinear material, optimal convergence is obtained after mesh density corresponding to 5000 elements as shown in

Chapter 4: Characterization of PVA-C using Finite Element Method

Figure: 4. 1, and optimal convergence was obtained at mesh density corresponding to 4600 elements as shown in Figure: 4.2.
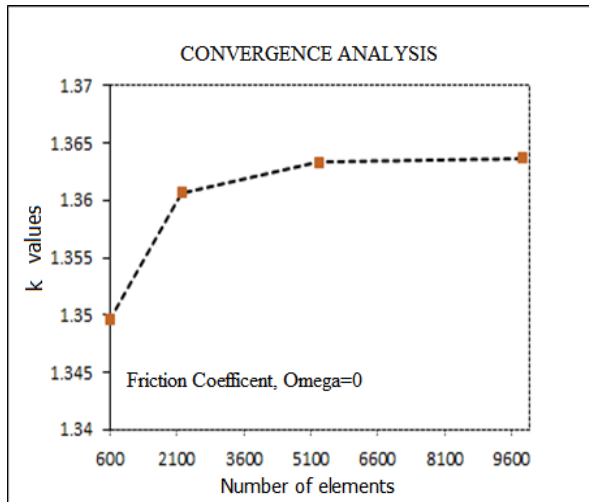
Figure 4.1: Non-dimensional value K is plotted against different grid density for converged solution. Friction coefficient is $\Omega = 0$.
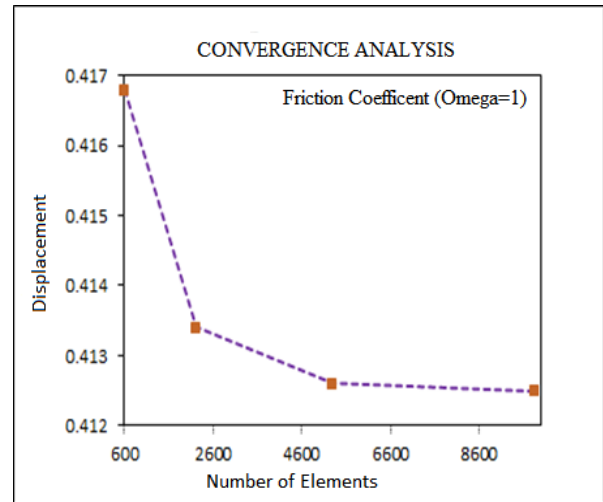
Figure 4.2: Non-dimensional value K is plotted against grid density for converged solution. Friction coefficient is $\Omega = 1$.

To understand the combined effect of the indenter radius and specimen thickness the indentation procedure was simulated using a model with axisymmetric finite elements. For finite and infinite thickness specimens, the load-displacement contours are shown in Figure: 4.3 and Figure: 4.4.
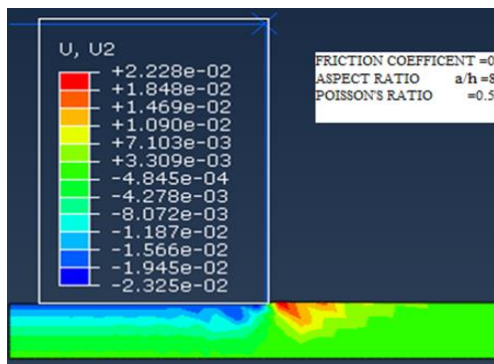
Figure 4.3: Force-deformation curve of specimen under cylindrical indenter. A boundary effect is observed for finite thick specimen 0.5 mm and $\Omega = 0$.
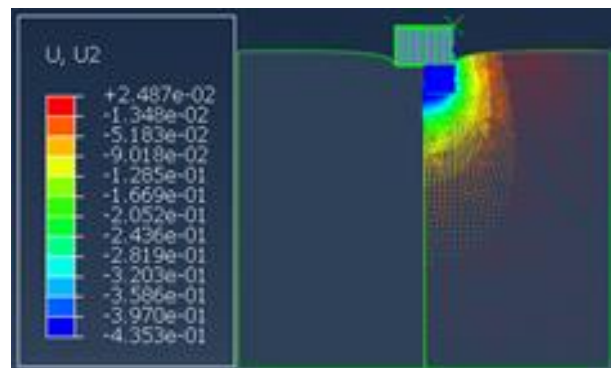
Figure 4.4: Force-deformation curve for a specimen with infinite thickness under cylindrical indentation. No boundary effect was observed for infinite thick 40 mm and $\Omega = 0$.

Chapter 4: Characterization of PVA-C using Finite Element Method

The coefficient of friction between the soft tissue and the indenter was set to zero. For indentation with large thickness, the soft tissue does not experience any boundary effect. When the thickness of the soft tissue decreases, the boundary will influence the apparent stiffness of the material. Similarly, the indenter size, and thickness plays an important role in the stiffness measurement. Thus, Indenter size, thickness plays an important role in the linearity of the indentation force-displacement data.

4.2.2 Experimental Results vs FE Model Simulated Results

At the initial stage of this numerical work, an axisymmetric FE model was developed using Abaqus and optimum mesh convergence was ensured. 7600 (CAX4RH) quadrilateral elements were taken in the convergence process. A 4-mm radius of cylindrical and spherical indenters were taken in the simulation process. Experimental data of PVA-C obtained from [38] was taken as an input parameter for this numerical work.

4.2.2.1 Cylindrical Indentation

A typical force-displacement curve for experimental and FE simulated data for 5% and 15% PVA-C are shown in Figure: 4.5 and Figure:4.6, respectively.
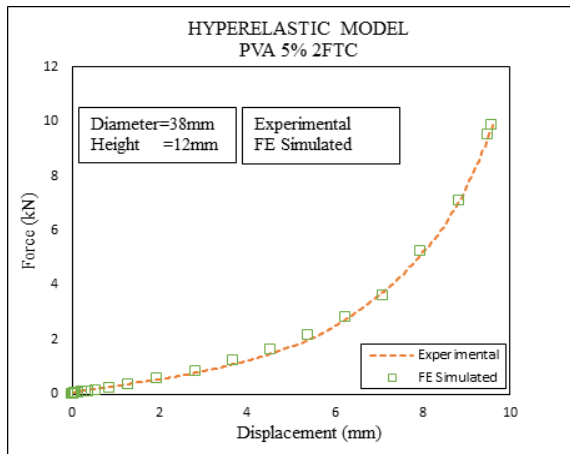
Figure 4.5: FE simulated and experimental data for PVA-C, 2 FTC at 5% concentration
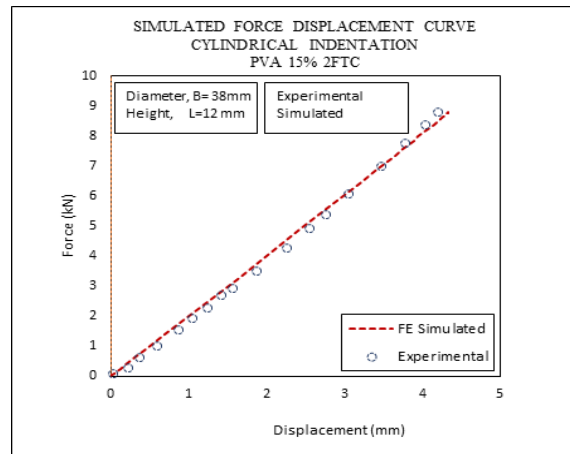
Figure 4.6: FE simulated experimental data for PVA-C, 2 FTC at 15% concentration.

Chapter 4: Characterization of PVA-C using Finite Element Method

Ogden model is used in the curve fitting process. As this fitting is non-optimized, inverse method will be applied to identify optimized Ogden parameter from cylindrical indention force-displacement curve for all PVA-C samples. PVA-C 5%, 2FTC showed hyperelastic behavior as shown in Figure: 4.5. PVA-C 15%, 2FTC showed liner elastic behavior as shown in Figure: 4.6. This is due to the increase PVA-C concentration.

4.2.2.2   Spherical Indentation

A typical force-displacement curve for experimental data obtained from [38] and FE simulated data for 5% and 15% PVA-C are used as input parameter for Mooney-Rivlin hyperelastic model shown in Figure: 4.7 and Figure:4.8, respectively.
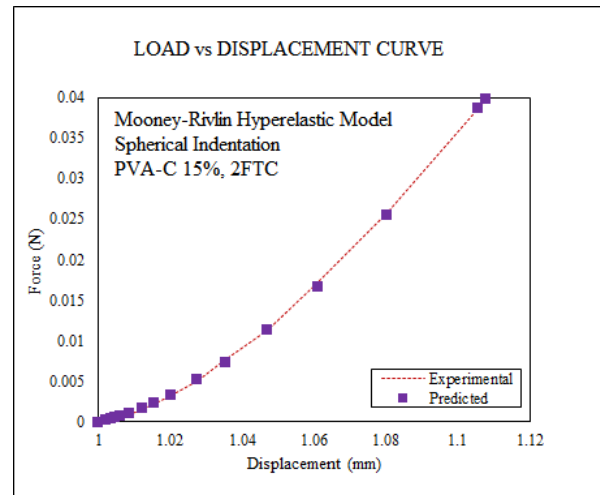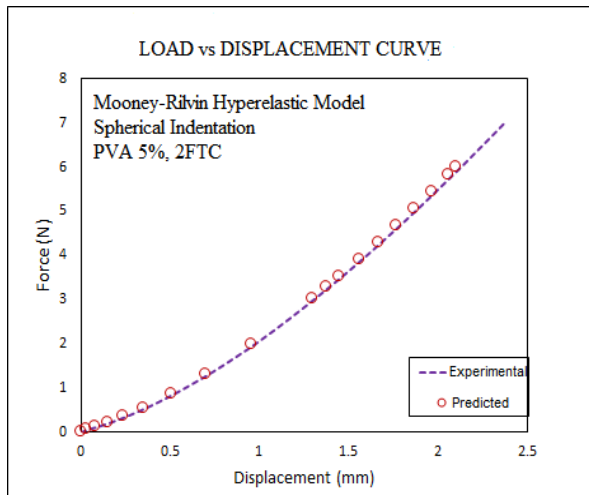
Figure 4.7: FE simulated and experimental data for PVA-C, 2 FTC at 5% concentration.

Figure 4.8: FE simulated and experimental data for PVA-C, 2 FTC at 15% concentration.

The experimental force-displacement data is plotted against corresponding FE simulated PVA-C (mimic) with finite thickness and 5% concentration shows nonlinearity. Also, PVA-C (mimic) with finite thickness and 15% concentration shows high stiffness based on the shown force- displacement relationship.

4.2.2.3   Uniaxial Test

Chapter 4: Characterization of PVA-C using Finite Element Method

A typical stress-strain relationship pertaining to for experimental test obtained from [38] and corresponding FE simulated (Ogden model) data for 5% and 15% PVA-C are used as input parameter for Mooney-Rivlin hyperelastic model are shown in Figure: 4.9 and Figure: 4.10, respectively.
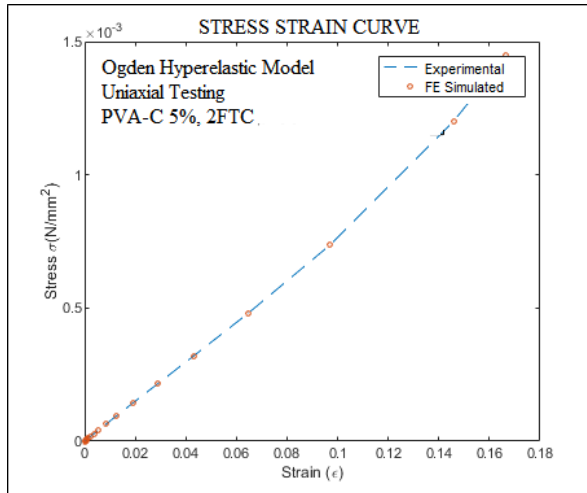
Figure 4.9: FE simulated (Ogden model) and experimental data for PVA-C, 2 FTC at 5% concentration.
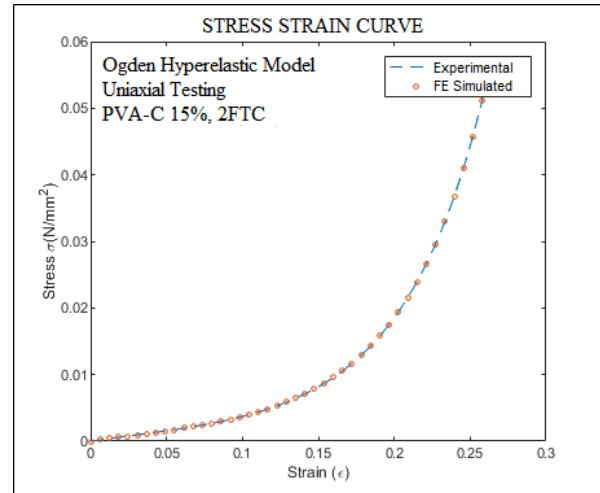
Figure 4.10: FE simulated (Ogden model) and experimental data for PVA-C, 2 FTC at 15% concentration.

The experimental stress-strain data is plotted against its FE simulated data counterparts. PVA-C (mimic) with 5% concentration and finite thickness shows nonlinearity. Also, PVA-C (mimic) with 15% concentration shows high stiffness based on stress-strain relationship.

4.2.3 Finite vs Infinite Thickness

Finite thickness: Indentation with a flat-ended cylindrical indenter applied to a sample with finite thickness was simulated using FEM. The mesh consisted of 5346 quadrilateral elements with aspect ratio greater than 1, average aspect ratio of 1.23, and largest aspect ratio of 2.65 of the mesh also included 120 triangular elements with aspect ratio greater average aspect ratio 1.27 and largest aspect ratio 1.84.

Infinite thickness: A flat-ended cylindrical indentation of infinite thickness is considered numerical FE simulation. The FE mesh consists of 4584 quadrilateral elements with aspect ratio of 2.88. It is also consisting of a triangular element 62 with aspect ratio greater than 1, average aspect ratio of 1.23, and largest aspect ratio of 1.61.

Chapter 4: Characterization of PVA-C using Finite Element Method

FE simulations were carried out for samples with (i) Finite and (ii) Infinite thickness load-displacement data were obtained for high accuracy of the FE solution, fine meshes were employed in the analysis. Typical force-displacement and displacement-distance contours are shown in 4.11 and 4.12.
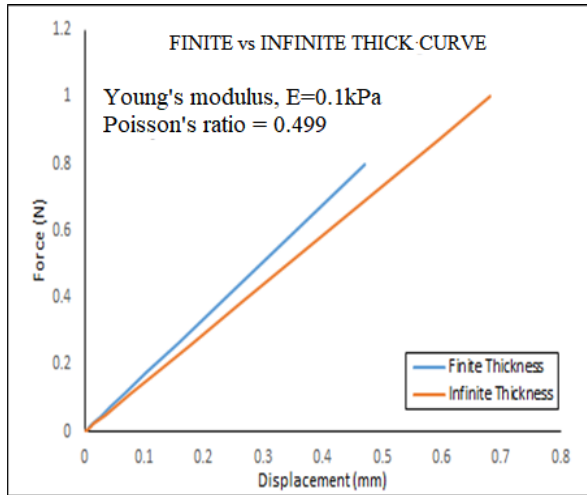
Figure 4.11: FE simulated load displacement data for samples with finite and infinite thickness where displacements of 0.4706 mm and 0.6818 mm were recorded.
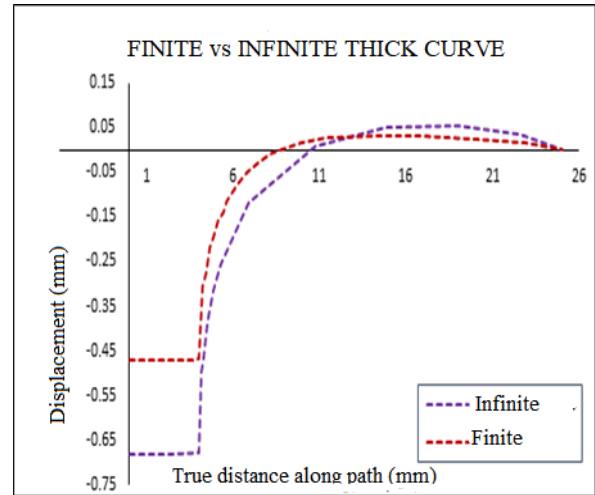
Figure 4.12: Simulated displacement data along true distance along path for finite and infinite thickness with maximum displacements of 0.4706 mm and 0.6818 mm.

4.3 Stress Analysis using FEA

A sample with a thickness of 12.57mm under indentation with a cylindrical indenter was simulated for stress using axisymmetric finite elements. For effective stress analysis using Sneddon's model, the total load required to produce deformation is given below:

$$P = \frac{2Eaw}{1 - v^2} \qquad (4.1)$$

E is the Young's modulus, v is the Poisson's ratio, a is the indenter radius, r is the specimen length and w is the depth of penetration. The distribution of stress beneath the punch is given by following equation [28]:

Chapter 4: Characterization of PVA-C using Finite Element Method

$$\sigma = \frac{2Ew}{\pi(1-v^2)}(a^2 - r^2)^{-1/2} \tag{4.2}$$

4.3.1 Effect of Stress on Thickness and Aspect Ratios

Indentation with a flat-ended cylindrical indenter applied to a sample with finite thickness specimen with the dimension of (19 mm x 12.57 mm) was simulated using FEM. The mesh consisted of 7600 quadrilateral elements A stress contours for finite thick is shown in Figure: 4.13.
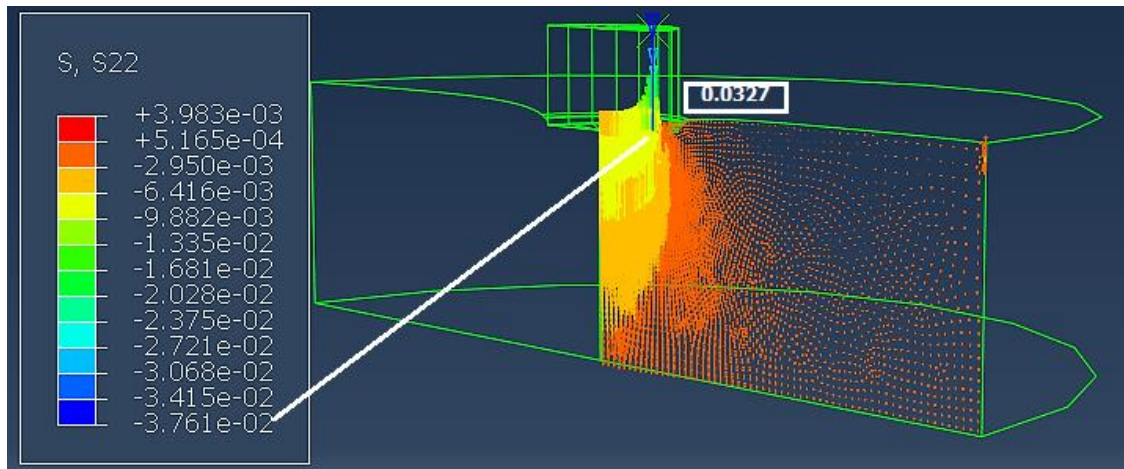
Figure 4.13: FE based stress contours for a sample with finite thickness under cylindrical indenter

Abaqus uses "query" to find the stress any point within the specimen. Maximum stress from the simulation was 0.037 kN/mm^2 and noted from the FE (Abaqus) simulation also pointed at Figure: 4.13. The displacement value obtained from numerical (FE) analysis was used in Equation (4.2) to calculate stress. Result shows good agreement between analytical and simulated solutions.

An axisymmetric FE model was developed using Abaqus. The effect of stress on thickness and aspect ratios are simulated numerically. The simulated results were compared with Sneddon's analytical solution. A typical stress distribution vs thickness and aspect ratios for a sample with

Chapter 4: Characterization of PVA-C using Finite Element Method

finite thickness were calculated using Sneddon's model shown in Figure: 4.14 and Figure: 4.15.
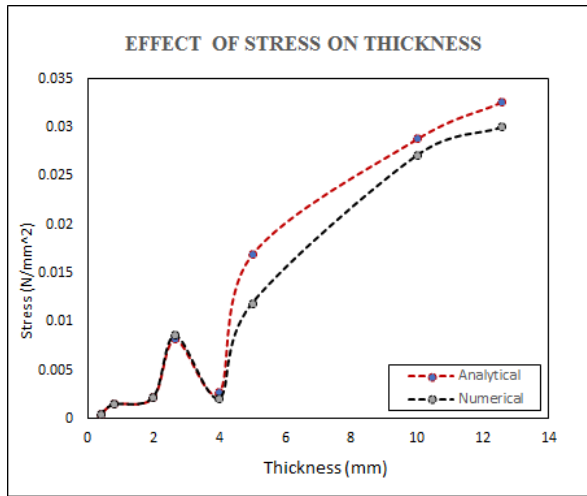
Figure 4.14: Stress vs thickness graph of a sample with finite thickness loaded by a cylindrical indenter, Sneddon's solution shows good agreement between analytical and simulated solutions Table: 4.1.
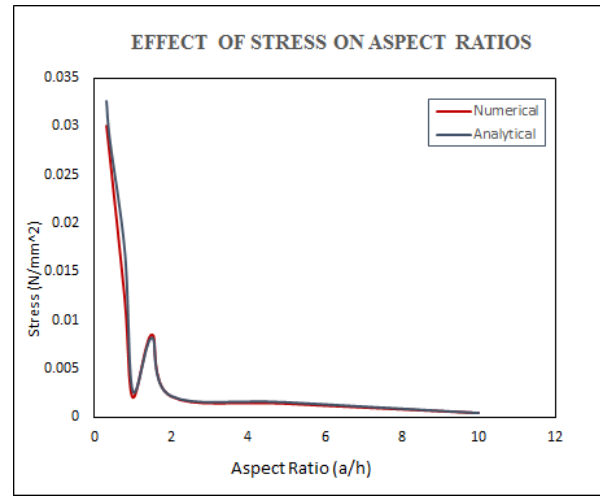
Figure 4.15: Stress vs aspect ratio graph of a sample with finite thickness loaded by a cylindrical indenter, Sneddon's solution shows good agreement between analytical and simulated solutions Table: 4.1.

Table 4. 1: Shows analytical and numerical solutions for Sneddon's model.

Thickness in (mm)	Aspect Ratio a/h	Young's modulus E	Shear Modulus μ	Displacement FEA (mm)	Stress (Analytical) σ_{zz} (N/mm^2)	FEA Stress σ_{zz} (N/mm^2)
12.57	0.3182	0.1	0.0333	0.3788	0.0326	0.03
10	0.4	0.1	0.0333	0.339	0.0287	0.027
5	0.8	0.1	0.0333	0.1987	0.0168	0.011
4	1	0.1	0.0333	0.1551	0.0026	0.002
2.67	1.498	0.1	0.0333	0.0963	0.0081	0.008
2	2	0.1	0.0333	0.02537	0.0021	0.0021
0.8	5	0.1	0.0333	0.01782	0.0015	0.0014
0.4	10	0.1	0.0333	0.00433	0.0004	0.0004

4.3.2   Stress Distribution for Linear Elastic and Hyperelastic Model

Sneddon's solution allowed us to calculate stress any point underneath the indenter. An axe-symmetric model is developed with the dimension of (19 mm x 12mm). Displacement control indentation is employed to calculate stress. Experimental stress-strain data taken from the PVA-C specimen at a concentration of 5%, 2FTC, simulated and the obtained stress-strain contours for linear elastic and hyperelastic model are shown in Figure: 4.16 and Figure: 4.17.

Chapter 4: Characterization of PVA-C using Finite Element Method
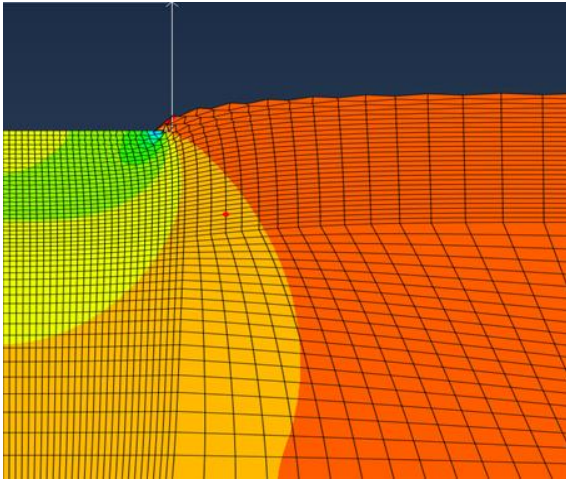
Figure 4.16: Stress contours (S, S22) at (δ = 8*mm*) for PVA-C with 5% and 2FTC (19 mm X 12 mm) for linear elastic model.
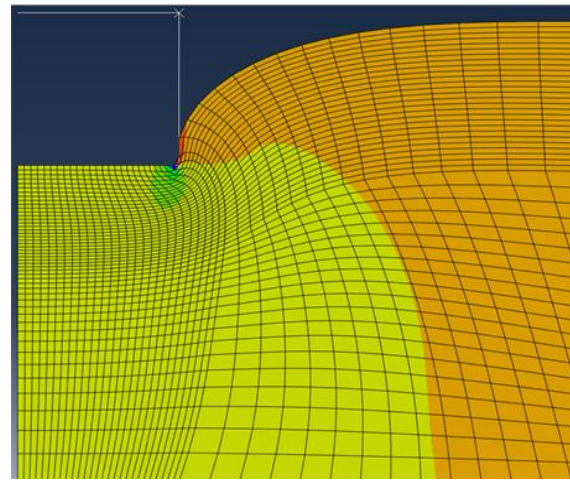
Figure 4.17: Stress contours (S, S22) at (δ = 8*mm*) for PVA-C with 15% 2FTC (19 X mm 12 mm) for hyperelastic model.

FE simulated vertical stress at a concentration of 5%, 2FTC are plotted against sample radius for linear elastic and hyperelastic models and shown in Figure: 4.18 and Figure: 4.19.
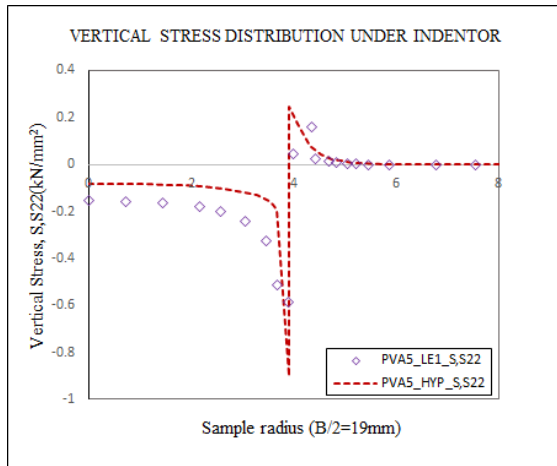
Figure 4.18: Distribution of stress under the indenter. For hyperelastic model and linear elastic model LE1 (E=10kPa, Poisson's ratio (*v*)=0.499).
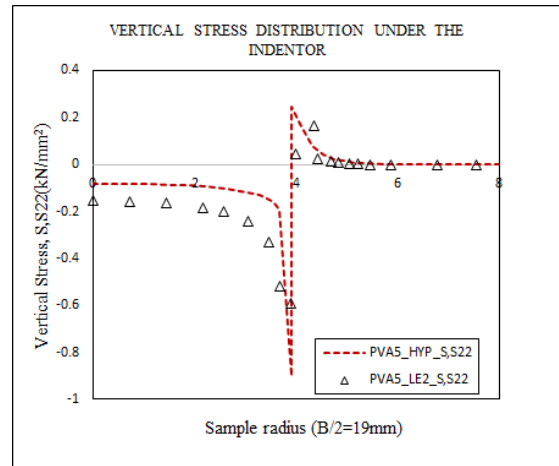
Figure 4.19: Distribution of stress under the indenter. For hyperelastic model and linear elastic model LE2 (E=1kPa, Poisson's ratio (*v*)=0.499).

Vertical stress distribution along horizontal and vertical axes were plotted for linear elastic and hyperelastic model are shown in Figure: 4.20 and Figure: 4.21 where PVA-C data of 10%, with 2FTC and 6FTC concentrations were used in the simulation.

Chapter 4: Characterization of PVA-C using Finite Element Method
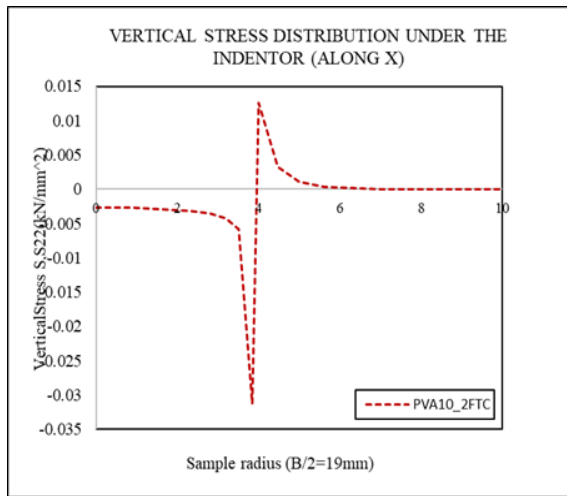
Figure 4.20: Vertical stress distribution for hyperelastic model of PVA 10% and 2FTC along X direction.
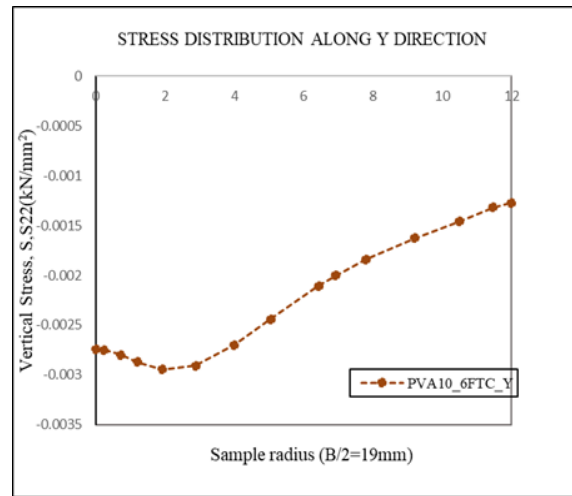
Figure 4.21: Vertical stress distribution for hyperelastic model of PVA 10% and 6FTC sample along Y direction.

Vertical stress distribution along horizontal axis was plotted for hyperelastic and linear elastic model shown in Figure: 4.21 and Figure: 4.23.
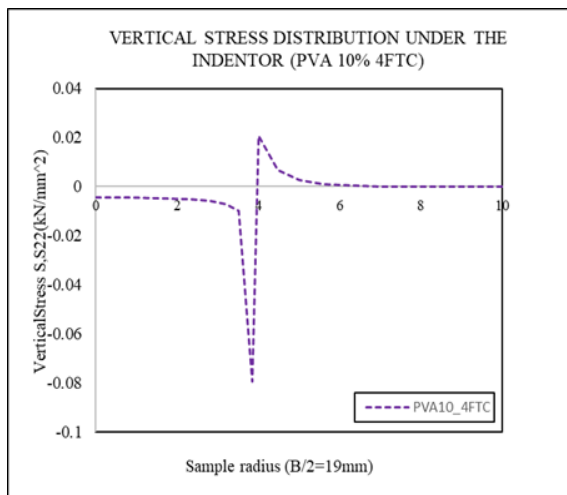
Figure 4.22: Vertical stress distribution for hyperelastic model of PVA 10% and 4FTC sample along X direction.
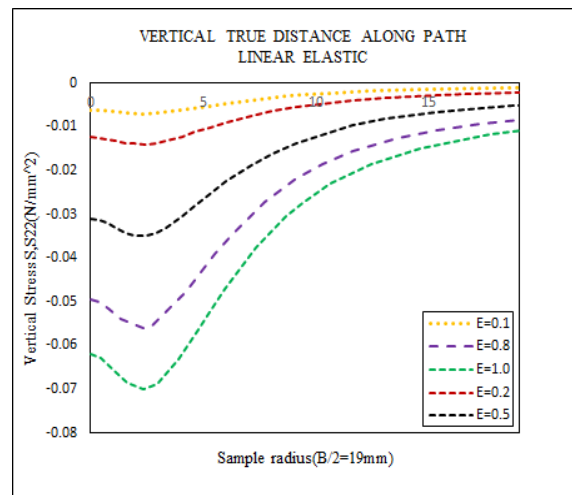
Figure 4.23: Vertical stress distribution for linear elastic model for different E values along Y direction.

Chapter 4: Characterization of PVA-C using Finite Element Method

4.4 Model Validation

A numerical analysis of indentation was conducted by the closed-form approximation incorporating the features of elastic half space (finite and infinite thick) model and simulated results were compared with theoretical calculations of Sneddon's, Hayes, Cao's and Zhang's model.

4.4.1 Hayes Model

To characterize the mechanical properties of soft tissues indentation tests have been conducted previously by several investigators. Due to lack of theoretical solutions, appropriate constitutive models for layered soft tissue specimen under indentation is limited [29]. To overcome those problems Hayes et al. developed a mathematical model for indentation testing of articular cartilage. The relation between the applied force (P) and displacement (w) is represented by a dimensionless parameter (k) as given below:

$$k = \frac{P(1 - v^2)}{2Eaw} \tag{4.3}$$

The values of k for a range of Poisson's ratios (v), indenter radius (a), thickness (h). To validate the present model with Hayes mathematical model an axisymmetric finite element model was developed using FE Abaqus solver. Simulation was conducted with friction ($\Omega = 1$) and without friction ($\Omega = 0$).

A significant friction effect is observed between the two indentation conversion factors vs aspect ratio. Results of these simulations are shown in Figure: 4.24 and Figure: 4.25 also in Figure: 4.26 and Figure: 4.27.

Chapter 4: Characterization of PVA-C using Finite Element Method
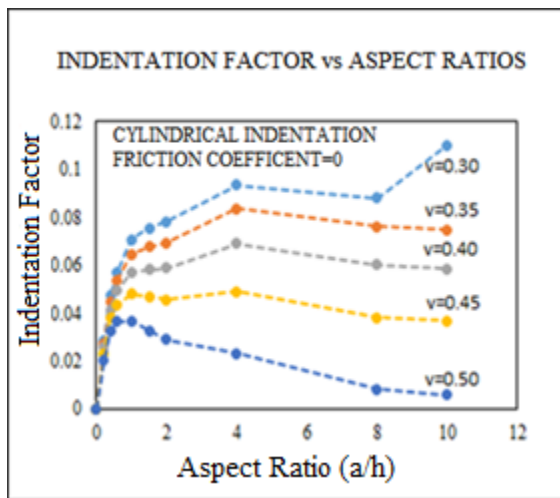
Figure 4.24: FE (Abaqus) simulated graph of indentation conversion factor w.r.t aspect ratio for a flat ended cylindrical indenter when friction coefficient is zero [29].
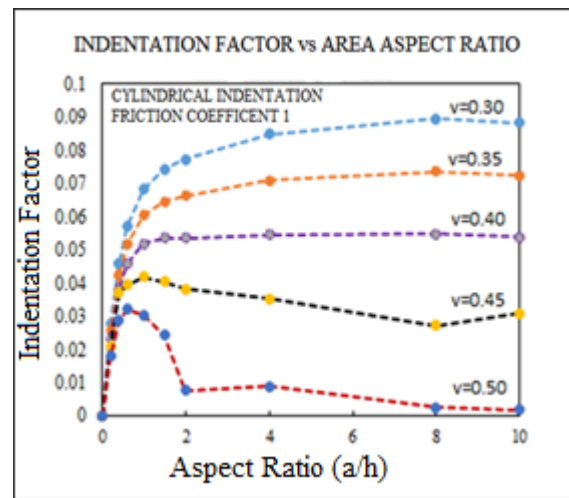
Figure 4.25: FE (Abaqus) simulated graph of indentation conversion factor w.r.t aspect ratio for a flat ended cylindrical indenter when friction coefficient is one [29].
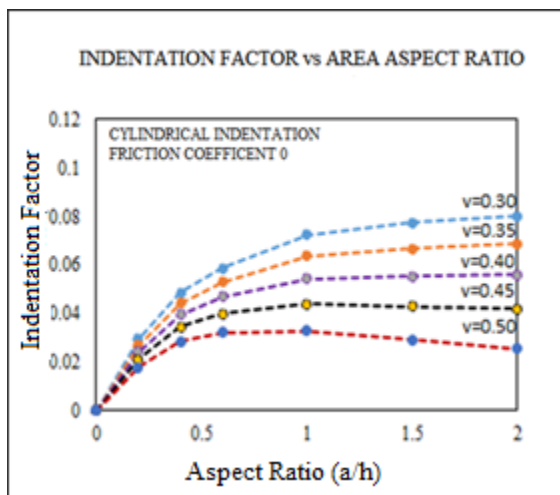
Figure 4.26: FE (Abaqus) simulated results of indentation conversion factor w.r.t aspect ratios for a flat ended cylindrical indenter. The friction coefficient is zero and aspect ratios are in the range of zero to two.
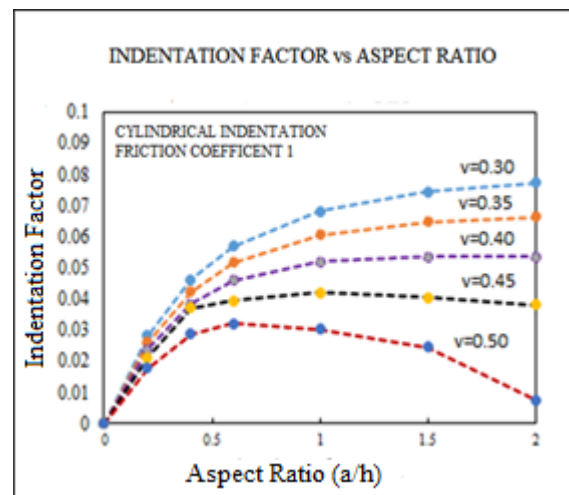
Figure 4.27: FE (Abaqus) simulated graph of indentation conversion factor w.r.t aspect ratios for a flat ended cylindrical indenter. The friction coefficient is one and aspect ratios are in the range of zero to two.

The validation exercise is conducted based on Hayes model of linear elastic theory. For flat ended cylindrical indenter, the displacement is directly proportional to load. The indentation factor $(w/h)(P/\mu a^2)$ is plotted for Poisson's ratios of 0.30, 0.35, 0.4, 0.45 and 0.5. For small aspect ratios increase no significant Poisson's effect is observed, but a significant friction and

Chapter 4: Characterization of PVA-C using Finite Element Method

Poisson's effect is visualized at Poisson's ratio 0.5 and friction coefficient one. Detailed calculations are provided in Appendix B.

4.4.2 Cao's Model

Cao et al. conducted a computational study to solve indentation problem of a flat punch applied to a compressible elastic layer [30]. They reported a number of expressions of the load-displacement curve for a range of Poisson's ratio $0.3 \sim 0.5$ and (a/h) is in the range of ($0 \sim 20$). The present work performed numerical simulation to validate Cao's model as a proof-of-principle. Cao made a little modification to Hayes load-depth equation [29] which is in the form:

$$P = \frac{2E}{1 - v^2} \, ahk\left(\frac{a}{h}, v\right)$$

(4.4)

Cao also normalized Π with a normalization factor f

$$f = 1.03e^{(-\frac{a}{h})} + \frac{\pi}{2}\frac{(1 - v^2)}{1 - 2v}\frac{a}{h}\left[1 - e^{\left(\frac{-a}{h}\right)}\right]$$

(4.5)

where e is the exponential term. When (a/h) approaches 0, f approaches to 1, and when (a/h) approaches infinity Cao's modified load-depth equation converges [12, 32]. Hence, the final f is:

$$f = \frac{\pi}{2}\frac{(1 - v^2)}{1 - 2v}\frac{a}{h}$$

(4.6)

A flat ended cylindrical indentation was modeled in the FEM (Abaqus) solver. Poisson's ratio is taken as 0.5, layer thickness (a/t_0) is taken from ($0.1 \sim 10$) with friction coefficients 0.5 and 0.05. The normalized dimensionless function (k/ f) and the ratio of the indenter radius to the layer thickness (a/h) are shown in Figure: 4.28 and Figure: 4.29.

Chapter 4: Characterization of PVA-C using Finite Element Method
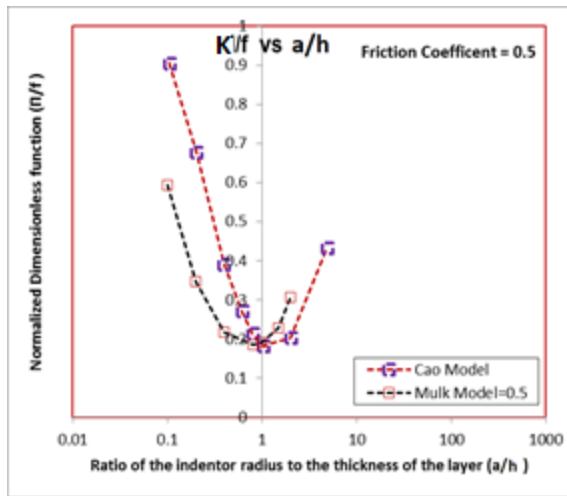
Figure 4.28: FE (Abaqus) simulated graph for the normalized dimensionless function (k/ f) and the ratio of the indenter radius to the layer thickness (a/h) at friction coefficient $\Omega = 0.5$
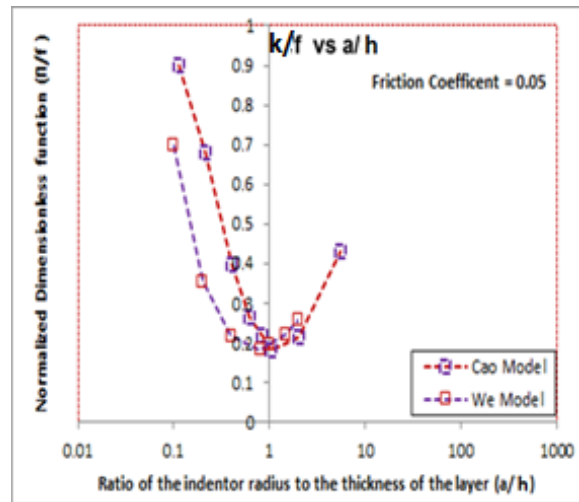
Figure 4.29: FE (Abaqus) simulated graph for the normalized dimensionless function (k/ f) and the ratio of the indenter radius to the layer thickness (a/h) at friction coefficient $\Omega = 0.05$

It has been observed that as the layer thickness ratio increases the normalized dimensionless function decreases until a/$h \geq 1$. Beyond this point friction effect decreased and negligible at (a/h » 1. Since, Cao et al. did not work on incompressible materials with Poisson's ratio ($v = 0.5$), this present work only investigated incompressible materials with Poisson's ratio ($v = 0.5$) and ($v = 0.05$) and found consistent results which validated Cao's model numerically.

Chapter 4: Characterization of PVA-C using Finite Element Method

4.4.3 Zhang's Model

To validate this study, an axisymmetric FE model of flat ended cylindrical indentation model was developed using Abaqus finite element solver to characterize the soft tissues biomechanics. Friction coefficient was employed in the simulation with respect to aspect ratio (a/h) and Poisson's ratio. The simulated displacements for different aspect ratio and friction coefficient were substituted in Zhang's equation. According to Zhang:

$$k\left(\frac{w}{h}, \frac{a}{h}, v\right) = \frac{P(1 - v^2)}{2Eaw} \tag{4.7}$$

where, P is the indentation force, w is the indentation depth, a is the indenter radius, h is the thickness of the soft tissue. Hence, the dimensionless K and coefficient of friction are plotted as shown in Figure: 4.29 and compared with Zhang's model shown in Figure: 4.30.
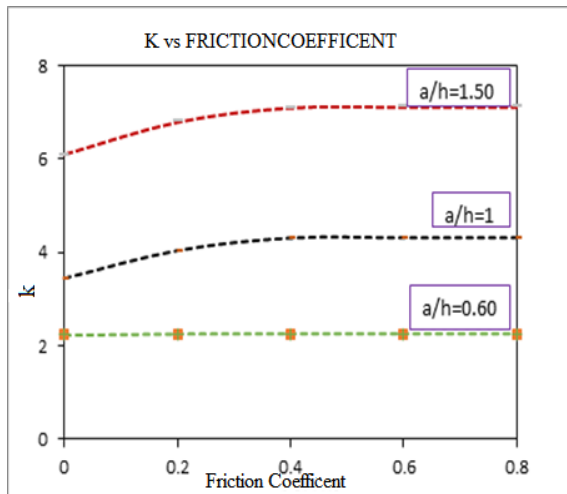
Figure 4.30: Graph of a dimensionless K vs coefficient of friction which investigating the effect of friction at different aspect ratios (a/h).
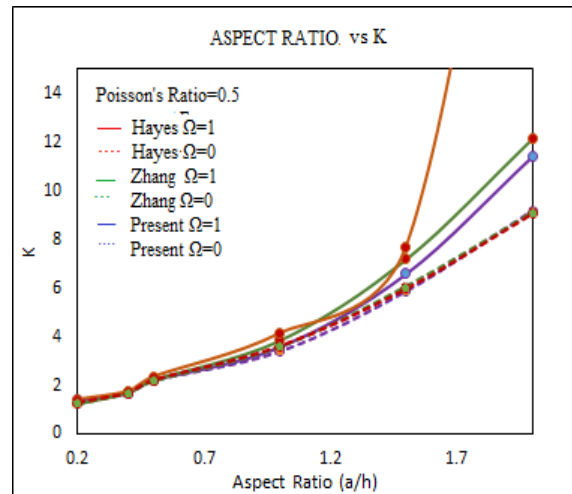
Figure 4.31: Graph of a FE (Abaqus) simulated results for dimensionless K and varying aspect ratios (a/h) and friction coefficients of Ω =0 and Ω =1.

Table: 4.2 shows the effect of dimensionless K vs coefficient of friction. relative indentation depth (w/h)% and aspect ratio (a/h)% are also shown in table. The simulated results were then plotted with Zhang's provided data [25]. A considerable effect of friction coefficient was observed as the value of friction coefficient increases.

Chapter 4: Characterization of PVA-C using Finite Element Method

Table 4. 2: Data obtained at different values of friction coefficient vs k. Obtained k values are compared with Zhang's model [25].

Aspect Ratio	Relative indention	Friction	Zhang	Present
a/h	depth (w/h)	Coefficient	k=P(1-vˆ2)/2Eaw	k=P(1-vˆ2)/2Eaw
0.6	4.400	0	2.213	2.207
0.6	4.364	0.2	2.210	2.215
0.6	4.355	0.4	2.211	2.217
0.6	4.353	0.6	2.212	2.217
0.6	4.353	0.8	2.213	2.218
1	4.768	0	4.070	3.168
1	4.070	0.2	4.334	4.155
1	3.818	0.4	4.393	4.163
1	3.813	0.6	4.414	4.171
1	3.810	0.8	4.390	4.176
1.5	0.072	0	5.915	5.884
1.5	0.064	0.2	6.190	6.558
1.5	0.062	0.4	6.239	6.803
1.5	0.061	0.6	6.263	6.822
1.5	0.061	0.8	6.326	6.830

Table: 4.3 presented a comparison of nondimensional functional k values between friction and no friction. Data obtained at different relative indentation depths of (w/h)=0.1%, 10%, 15% and 100% with $\Omega = 0$ and $\Omega = 1$ are compared between the present model and Zhang's model where good consistency was found. There is a considerable effect of friction coefficient on indentation however, as the aspect ratio (indenter radius to sample thickness) increases observed effects become more significant.

Table 4. 3: Data obtained at different relative indentation depths (w/h)=0.1%, 10% and 15%. Obtained k values are compared with Zhang's model [25].

k values	$\Omega=0$	$\Omega=1$	Difference	$\Omega=1$	$\Omega=1$	Difference
w/h(percent)	Present	Present	Percentage	Present	Zhang	Percentage
0.1	9.425	9.516	0.955	9.516	9.111	4.268
10	9.488	12.365	23.262	12.365	11.555	6.553
15	9.520	12.511	23.899	12.511	13.052	-4.323
100	10.030	13.084	23.341	13.084	13.08	0.033

The results were also validated by changing Young's modulus (E1, E2). Through axisymmetric cylindrical indentation and the depth of penetrations were recorded with increasing Young's modulus. The simulated displacement validated the analytical solution $\frac{E_1}{E_2} = \frac{w_1}{w_2}$

Chapter 4: Characterization of PVA-C using Finite Element Method

4.5   Novel Approach

A novel analytical model was developed by adding a new parameter called friction coefficient as a function of k in Zhang's solution [25]. To validate this analytical model using the present FE model, let us consider k as a function of relative indentation depth, ($\Psi = \frac{w}{h}$), aspect ratio ($\Phi = \frac{\bar{a}}{h}$), Poisson's ratio, ν and friction coefficient $\Omega = (F_c)$. The new equation is given below:

$$P = \frac{2Eaw}{(1 - \nu^2)}\mathbf{k}(\Phi, \Psi, \Omega) \qquad (4.8)$$

The validation of the novel analytical solution is illustrated in Figure: 4.32 and Figure: 4.33.
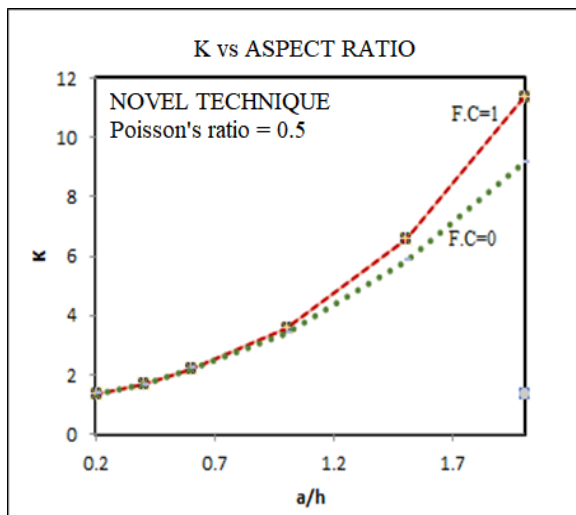
Figure 4.32: Non-dimensional value K is plotted against aspect ratio indenter radius to material thickness(*a/h*).
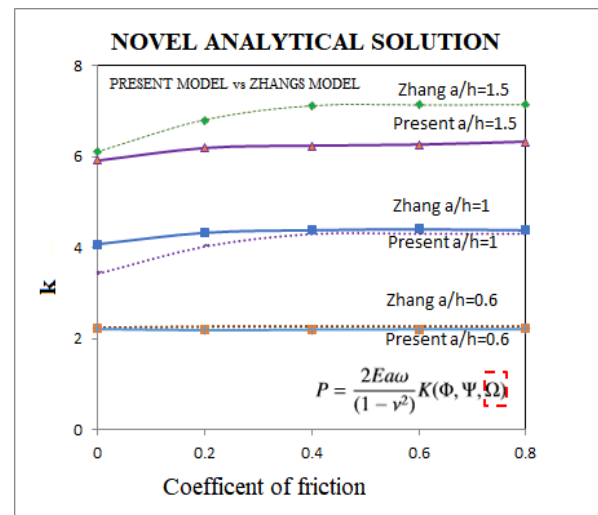
Figure 4.33: Non-dimensional value K is plotted against fraction coefficient with varying aspect ratios (*a/h*), Table: 4.2.

Friction coefficient is believed to be an important factor for nonlinear soft biological tissues. As a part of the validation exercise an axisymmetric FE simulation is conducted at friction coefficients of 1 and 0. The simulated results are presented as a part of the validation exercise.

The numerical deformation is inserted in the novel equation to calculate the dimensionless value K. The above figures indicate a good agreement between finite element and analytical results, especially for $\Omega = 1$ and $\Omega = 0$. It implies that the novel analytical model exhibited

Chapter 4: Characterization of PVA-C using Finite Element Method

promising results. The verification of the novel analytical solution is introduced here as illustrated in Figure:4.34 and Figure: 4.35 as a part of the proof of the principle. This new approach shows a good potential to investigate the mechanical responses of finite thick biological tissues.

4.5.1   Model Validation

To conduct numerical validation of the present method, simulated displacement data were inserted into the analytical solutions. Hence the same data was used in Hayes [29] and Zhang's [25] models considering no friction between the indenter and the specimen. For Zhang's, Hayes' and the present model, the analytical solutions of k vs Poisson's ratio (v) at different aspect ratios are plotted. Also, k vs coefficient of friction is plotted for the purpose of comparison among Zhang, Hayes and the present models. Both graphs are shown in Figure: 4.34 and Figure: 4.35.
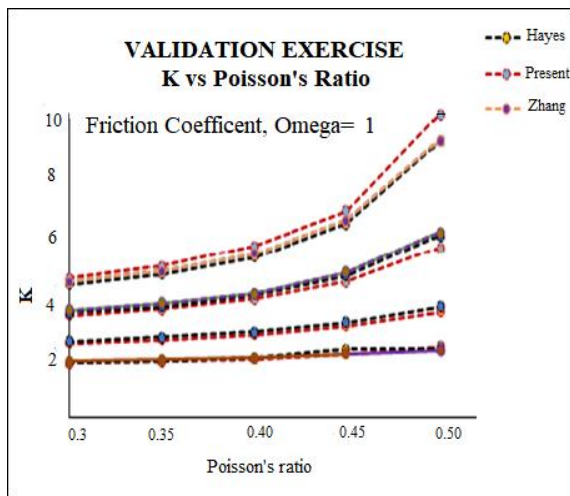
Figure 4.34: FE (Abaqus) simulated graph of dimensionless k and relative indentation depth (w/h)% for finite thickness with comparison to Zhang model. All simulations were performed at friction coefficient $\Omega = 1$.
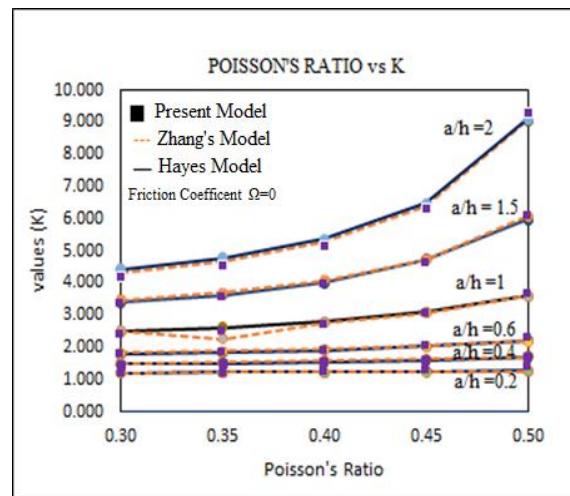
Figure 4.35: FE (Abaqus) simulated graph of dimensionless k vs Poisson's ratio for finite thickness with comparison to Zhang and Hayes models. All simulations were performed at friction coefficient $\Omega = 0$.

Table 4. 4: Data obtained at different relative indentation depth (w/h)=0.1%. k values are compared with Hayes, Zhang and the present models [25, 29].

Chapter 4: Characterization of PVA-C using Finite Element Method

a/h	Present	Zhang	Hayes	Present	Zhang	Hayes	Present	Zhang	Hayes	Present	Zhang	Hayes	Present	Zhang	Hayes
							$\Omega = 0$			w/h=0.1%					
	v=0.3			v=0.35			v=0.40			v=0.45			v=0.50		
0.2	1.18	1.21	1.21	1.21	1.22	1.21	1.24	1.22	1.23	1.29	1.23	1.25	1.40	1.244	1.28
0.4	1.44	1.513	1.47	1.47	1.54	1.50	1.52	1.57	1.54	1.59	1.625	1.59	1.71	1.70	1.698
0.6	1.77	1.82	1.78	1.81	1.87	1.83	1.89	1.93	1.91	2.01	2.03	2.03	2.26	2.18	2.21
1	2.36	2.52	2.48	2.49	2.26	2.60	2.68	2.77	2.78	3.01	3.06	3.08	3.62	3.59	3.60
1.5	3.31	3.479	3.4	3.55	3.712	3.62	3.93	4.08	3.99	4.61	4.73	4.73	6.08	6.078	5.97
2	4.20	4.42	4.33	4.56	4.782	4.68	5.16	5.36	5.27	6.33	6.47	6.38	9.31	9.11	9.07

The simulated results for incompressible material ($v = 0.499$) are further analyzed for statistical significance. The R-squared values among the tree models were found to be very consistent and this result completes the verification process as shown in Table: 4.5.

Table 4. 5: Data obtained at different Poisson's and Aspect ratios compared k values with Zhang and Hayes models.

Aspect Ratio	Linear equation $\Omega = 0$			R^2 value		
(a/h)	Present	Zhang	Hayes	Present	Zhang	Hayes
0.2	y = 1.0234x + 0.855	y = 0.126x + 1.1784	y = 0.364x + 1.0924	0.8431	0.9183	0.8583
0.4	y = 1.3461x + 1.0064	y = 0.91x + 1.2262	y = 1.098x + 1.1234	0.8806	0.8897	0.8897
0.6	y = 2.3951x + 0.9886	y = 1.782x + 1.2562	y = 2.092x + 1.1196	0.9105	0.8218	0.9478
1	y = 6.0996x + 0.3932	y = 5.8848x + 0.4886	y = 5.48x + 0.7212	0.8959	0.9544	0.9478
1.5	y = 13.214x - 0.9895	y = 12.44x - 0.559	y = 12.49x - 0.6502	0.961	0.961	0.943
2.0	y = 23.98x - 3.6803	y = 22.116x - 2.813	y = 22.326x - 2.9824	0.9568	0.9568	0.9623

The simulated results were fitted in linear regression model and finally, R-square test were conducted. At $\Omega = 0$, R-squared values from the three-model found consistent.

Chapter 4: Characterization of PVA-C using Finite Element Method

4.6 Summary

In this chapter, an axisymmetric model was developed for the cylindrical, spherical and uniaxial indentation test. FE simulation package Abaqus was used to characterize material properties of soft tissues or mimics. A concentrated load was applied at the top of the indenter's reference point and the reference point was also chosen at the right top corner of the indenter. To discuss the nonlinearity, two hyperelastic models were discussed in this chapter. Ogden and Mooney-Rivlin hyperelastic model are considered to be appropriate for the finite element analysis. At the initial stage of the study, axisymmetric linear elastic model was considered to be appropriate for the understanding of displacement pattern. Mesh refinement process was adopted for optimal convergence and the accuracy of the results were ensured. Finite and infinite thickness specimen were considered for FE simulation. The effect of relative indentation depth, aspect ratio, Poisson's ratio and dimensionless k on the indentation response of soft tissues were investigated.

To investigate the friction, the effect of friction coefficient Ω was added with Zhang's equation to the non-dimensional parameter (k) to be considered as a function of (Φ, Ψ, and Ω) [25]. At friction coefficient Ω =0, Hayes, Zhang and the present model shows good agreement as shown in Table: 4.4 and 4.5. A significant variation of results observed when a range of friction coefficients were introduced as shown in Table: 4.2. A significant variation (23%) is observed when we compared the results for Ω =0 and Ω =1 at a relative indentation depth (w/h=100%).

At the second stage, stress analyses were conducted for linear and hyperelastic model. Furthermore, a validation exercise was conducted using Hayes, and Zhang's and present data.

Later in this thesis, hyperelastic models will be constructed using experimental data for soft biological tissue and simulation will be performed. Finally, Ogden and Mooney-Rivlin hyperelastic models were adopted to capture unknown material properties. This model will be implemented in the parametric studies of material characterization and will be included in Chapter 5.

Chapter 5

Soft Tissues Mechanical Characterization Using Inverse Finite Element Technique.

5.1 Introduction

Inverse finite element analysis is a numerical method used to characterize the material properties of soft tissues for biomedical applications engineering [135, 164]. A number of techniques have been implemented previously to characterize tissue in *vivo,* ex *vivo* or tissue mimicking materials [119]. During the characterization process, the first order Ogden hyperelastic model is used for estimating material properties. Biological tissues are usually acquired from surgeries as small specimens with irregular shapes and rough surfaces. This precludes the possibility of using conventional techniques such as uniaxial testing for mechanical characterization of such tissue specimen's mechanical characterization. Another challenge is tissues' complex nonlinear behavior and heterogeneity which further complicates its mechanical. property.

Many previous researchers have indicated that indentation test is an effective technique for characterizing the compressive behavior of tissue under small and large deformation loading conditions [10]. They also questioned the validity of infinitesimal deformation theory for most

Chapter 5: Soft Tissue Characterization using Inverse Finite Element Techniques

biological tissue under physiological conditions, hence the necessity of considering tissue geometric and intrinsic nonlinearity in mechanical testing data interpretation [165]. Samani et al. considered tissue hyperelasticity in their indentation-based measurement technique and reported hyperelastic parameters of breast tissues. For the purpose, they processed force-displacement data pertaining to the tissue indentation test through an inverse FE framework [15].

Their method was founded on a combined "experimental-numerical" approach aimed at characterizing tissue hyperelastic behavior [10, 14, 15]. Soft tissues or tissue mimicking materials are typically modeled as nonlinear, homogeneous, isotropic and nearly incompressible. Ogden hyperelastic model is commonly used to capture biological tissue nonlinearity. Isvilanonda et al. used first order Ogden constitutive model in the material characterization process and using inverse problem analysis of experimental data, they found obtained very good results [91].

A similar approach is followed in this dissertation whereby indentation testing data is processed through an inverse FE framework to estimate tissue hyperelastic parameters. For solving the inverse problem in this context, an optimization algorithm developed in MATLAB was used where tissue FE model was used to calculate the cost function to be minimized. In order to measure material properties of soft tissues through inverse analysis, two major steps are considered (i) developing a mathematical model which is physically acceptable and mechanically pragmatic and (ii) developing a data inversion technique for parameter estimation [166].

For the first step FE modeling is a good candidate which has been used extensively in this dissertation while for the second step, a cost or objective function, which measures the difference between measured and model based mechanical response is developed. Having these two essential elements, the hyperelastic parameters can be calculated through an optimization by iteratively refining an initial guess of the sought parameters until the cost function reaches its minimum value [26].

Chapter 5: Soft Tissue Characterization using Inverse Finite Element Techniques

In the previous chapter, a non-linear elastic model was discussed. This chapter is geared toward developing a comprehensive understanding of soft tissues characterization based on a hyperelastic model using inverse analysis.

The principle objectives of the study presented in this chapter are:

(i) To conduct a parametric analysis with varying material properties and examine the effectiveness of an optimization meth

(ii) To develop a non-linear hyperelastic analysis for soft tissue samples with finite and infinite thickness.

(iii)To investigate the effect of specimen thickness, PVA-C concentration and Freeze-thaw cycle on (μ, α)

(iv)To develop and implement an inverse algorithm for Ogden hyperelastic model to determine tissue hyperelastic parameters from experimental data.

(v) To assess estimated parameters (μ, α) based on the non-linear hyperelastic FEA model prediction.

(vi) To conduct a stability analysis by using Levenburg-Marqardt (LM) optimization algorithm.

The first section of this chapter describes a hyperelastic material model for solving nonlinear material using Abaqus. This section also discussed about choice of constitutive model and inverse finite element analysis. The second section described the novel optimization algorithm for the identification of material properties. The third section of this chapter is the results section using cylindrical. spherical and uniaxial indentation. Finally. The fourth section discusses about effect on Mu and Alpha on concentration, freeze thaw cycle and sensitivity analysis. This chapter concludes followed by a summary.

Chapter 5: Soft Tissue Characterization using Inverse Finite Element Techniques

5.2   Hyperelastic Model

Polyvinyl alcohol cryogel (PVA-C) samples of 5%, 10% and 15% w/w concentration is modeled as soft tissues mimics to examine their non-linear material properties. Experimental force-displacement ($F - D$) data used as input parameter for Ogden and Mooney-Rivlin hyperelastic model.

5.2.1   Choice of Constitutive Model

Many previous studies reported the effectiveness of using Ogden model for correctly capturing the hyperelastic behavior of soft materials including hydrogels and living tissues [11, 100]. Selecting proper constitutive model is essential for determining physically meaningful material parameters which is still a major challenge [11]. To validate hyperelastic parameters obtained from cylindrical or spherical indentation or uniaxial compression testing, first order Ogden model has been utilized within inverse problem frameworks.

A hyperelastic material is a type of constitutive model where the presence of a strain energy density function is assumed, and stress-strain relationship is derived from a strain energy density function. The Ogden hyperelastic model for isotropic material can be obtained from strain

$$W = \sum_{i=1}^{\infty} \frac{\mu_i}{\alpha_i} (\lambda_1^{\alpha_i} + \lambda_2^{\alpha_i} + \lambda_3^{\alpha_i} - 3) + \sum_{i=1}^{\infty} k_i (J^{el} - 1)^{2i} \tag{5.1}$$

Where μ, α and K are presented as constitutive parameters. J is the determinant of the strain tensor and λ is known as the principle stretches. For incompressible materials deformation J = 1 leads the second term the above equation to vanish. For first order Ogden model $i = 1$. Thus, the model will have only two unknown parameters of initial shear modulus (μ), and strain hardening exponent (α).

Chapter 5: Soft Tissue Characterization using Inverse Finite Element Techniques

For a uniaxial compression test the nominal stress (σ) is represented as a function of the stretch ratio λ. The first order Ogden material model can be presented in the form given below:

$$\sigma = \frac{2\mu}{\alpha}\left(\lambda^{(\alpha-1)} - \lambda^{(-\alpha/2-1)}\right) \tag{5.2}$$

The above mentioned two equations can take only positive values. The experimental force-displacement ($F-d$) data are used as an input parameter for hyperelastic model. Through curve fitting to the experimental ($\sigma - \lambda$) data the first order Ogden parameter is extracted.

5.3   Numerical Analysis

Numerical analysis was performed by FEM using Abaqus version 6:13−4(2013). Spherical indenter and rigid flat ended cylindrical indenter were used for numerical analysis. A 4 mm radius of test indenter indented a soft tissue mimicking sample of PVA-C with, 5%, 10%, and 15% (w/w) concentration. The sample radius 19 mm and thickness 12mm. The soft tissue sample was is modeled as homogeneous, isotropic and nearly incompressible.

An axisymmetric model was developed and meshed with (CAX4RH) and (CAX3H) linear quadrilateral elements. A very fine mesh was made at the contact zone and comparatively coarse mesh was utilized outside the contact zone. The boundary conditions for three side of the sample was fixed ($U1 = U2 = U3 = UR1 = UR2 = UR3 = 0$) and one side is variable ($U1 = U3 = UR2 = 0$). During the indentation test a 4N vertical load was applied and the contact between the indenter and the sample was considered frictionless. Ogden hyperelastic material model was considered for PVA-C samples undergoing indentation test the data of which was provided by [38]. The simulation was completed in 13 steps with a step size of 0.01. To observe the indentation responses, the hyperelastic FE model was analyzed including sample with finite thick and infinite thickness made of PVA-C with (5%) and (15%) concentrations.

Chapter 5: Soft Tissue Characterization using Inverse Finite Element Techniques

5.3.1 Numerical Model Setting

A two dimensional axisymmetric cylindrical and spherical indentation model was developed using Abaqus. Ogden first order strain energy density function was used in the numerical simulation.7818 (CAX4RH) number of nodes generated in the meshing process shown in Table: 5.1 and Table: 5.2.

Table 5. 1: Generated FE mesh parameters for cylindrical indentation. Ogden hyperelastic material model used in simulation of soft tissue mimic PVA-C 5%, 2FTC and 15%, 2FTC.

CYLINDRICAL INDENTATION			
HYPERELASTIC MODEL - OGDEN STRAIN ENERGY FUNCTION WITH N = 1			
	μ	α	D
	0.0003	11.77	0.00000000
P R O B L E M S I Z E			
NUMBER OF ELEMENTS			3864
NUMBER OF ELEMENTS DEFINED BY THE USER			3783
NUMBER OF INTERNAL ELEMENTS GENERATED FOR CONTACT			80
NUMBER OF NODES IS			7818
NUMBER OF NODES DEFINED BY THE USER			3875
NUMBER OF INTERNAL NODES GENERATED BY THE PROGRAM			3943
TOTAL NUMBER OF VARIABLES IN THE MODEL			11694

Table 5.2: Generated FE mesh parameters for spherical indentation. Ogden hyperelastic material model used in simulation of soft tissue mimic PVA-C 5%, and 15% w/w, 2FTC

SPHERICAL INDENTATION			
HYPERELASTIC MODEL - OGDEN STRAIN ENERGY FUNCTION WITH N = 1			
	μ	α	D
	1.43977019	2.16155547	0.00000000
P R O B L E M S I Z E			
NUMBER OF ELEMENTS			3864
NUMBER OF ELEMENTS DEFINED BY THE USER			3783
NUMBER OF INTERNAL ELEMENTS GENERATED FOR CONTACT			80
NUMBER OF NODES IS			7818
NUMBER OF NODES DEFINED BY THE USER			3875
NUMBER OF INTERNAL NODES GENERATED BY THE PROGRAM			3943
TOTAL NUMBER OF VARIABLES IN THE MODEL			11694

An axisymmetric FE model was developed by using Abaqus, PVA-C 5%, and 15%, 2FTC experimental data obtained from [38] used as an input parameter for first order Ogden

Chapter 5: Soft Tissue Characterization using Inverse Finite Element Techniques

hyperelastic model. Load-displacement graph for both PVA concentration are shown in Figure: 5.1 and Figure: 5.2.
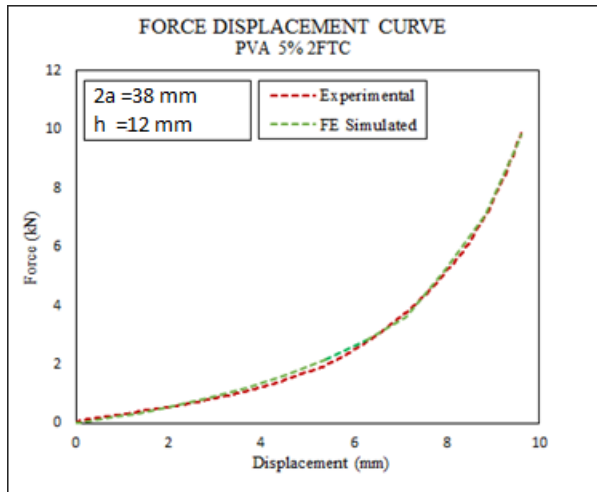
Figure 5.1: Load vs displacement graph for PVA-C model with 5% concentration.
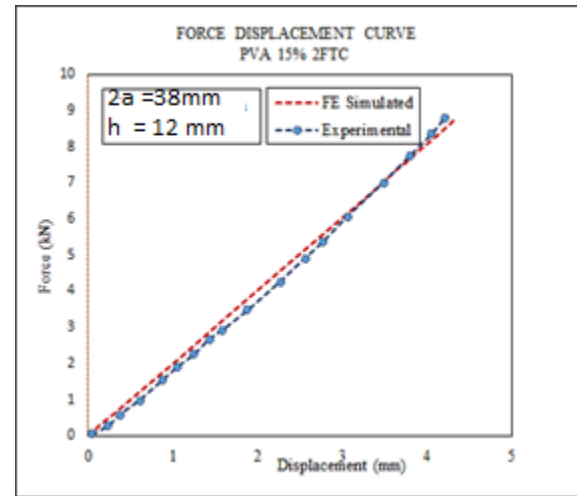
Figure 5.2: Load vs displacement graph for PVA-C model with 15% concentrations.

5.4   Parametric Studies

Based on previous research it has been found that the hyperelastic parameters determined using cylindrical or spherical indentation testing are not always the same as those obtained from experimental uniaxial compression test [10, 26, 91, 126]. To investigate the sources of such disagreement a parametric study was conducted to examine the influence of (μ, α) on the shape of the simulated data. An optimization algorithm combined with MATLAB used for minimizing the sum of squared difference between the experimental measurements and the FE simulated Ogden hyperelastic model predicted results. Finally, unknown parameters (μ, α) were determined. Sensitivity analysis was conducted to verify the accuracy and robustness of the parameters.

5.5   Inverse Finite Element Analysis

Inverse FE method was used to determine the hyperelastic material parameters of soft tissue specimens from indentation responses. Based on Hadamard's definition an inverse problem is

Chapter 5: Soft Tissue Characterization using Inverse Finite Element Techniques

ill posted if one of the three conditions are violated (i) existence, (ii) uniqueness, and (iii) stability. This means that stability of a solution depends on the quality of the input data which can be contaminated due to significant noises sources. Zhang et al. reported that as unstable solution can be encountered in inverse problems much attention must to be paid to obtain meaningful solutions. Many optimization algorithms are commonly used as such least square fitting power low, Levenberg-Marquardt (LM) Trust Region Algorithm, and Kalman Filter to solve the inverse problems.

The inverse analysis is introduced to minimize an objective function with respect to unknown constitutive material parameters (μ, α) that match the experimental data [11, 26]. It fits experimental data by determining material parameters (μ, α). In order to have accurate optimized results choosing the right model is not always obvious. Levenberg-Marquardt (LM) method was used in this dissertation to extract the unknown parameters based on inverse analysis. LM method is defined as the minimization of the error function Φ with respect to a vector $\hat{P}$. The error function is represented as:

$$\Phi(\hat{P}) = \frac{1}{2}\sum_{i=1}^{n}\left[r_i(\hat{P})\right]^2 = \frac{1}{2}r^T r \tag{5.3}$$

Here, $\hat{P}$ is a vector which contains unknown constitutive parameters $\widehat{P}^T = \{\mu, \alpha\}$ and n are the number of measurements. The vector $\hat{r}$ is defined as:

$$\hat{r} = t^* - \hat{t} \tag{5.4}$$

where, t^* and $\hat{t}$ are the model predicted and experimental data.

5.5.1   Optimization Algorithm: Using Ogden Model

A detailed flowchart of the inverse optimization process to characterize the tissue hyperelastic parameters used in the current study shown in Figure: 5.3.

Chapter 5: Soft Tissue Characterization using Inverse Finite Element Techniques
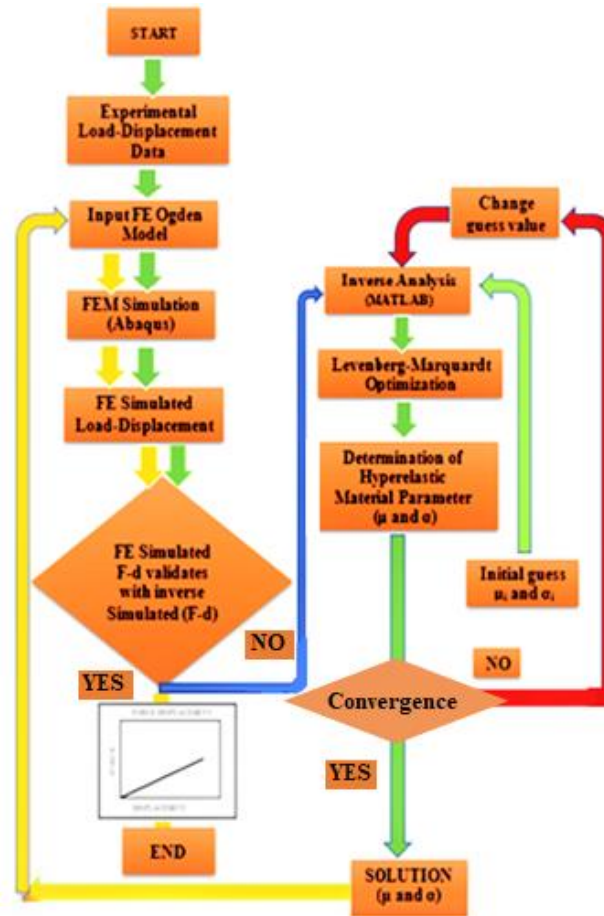
Figure 5.3: Flowchart of the inverse optimization process to characterize the unknown tissue hyperelastic parameters Ogden parameter. First, experimental (F-D) data are used as an input parameter for the numerical model (Abaqus). Simulated (F-D) data then used as an input parameter for inverse analysis (MATLAB). An object junction introduced to minimize the quadratic difference between simulated and model predicted data. Through optimization process numerical convergence was achieved and optimized unknown parameter was obtained. These parameters were used as an input parameter of Abaqus for numerical validation.

5.5.2   Mesh Optimization with μ and α

Although, the implicit method with Newton-Raphson iterative solver is enough to obtain converged solution, mesh optimization through adaptive meshing was adopted for numerical accuracy. Optimized μ and α through mesh convergence are shown in Figure: 5.4, Figure: 5.5, Figure: 5.6, and Figure: 5.7.

Chapter 5: Soft Tissue Characterization using Inverse Finite Element Techniques
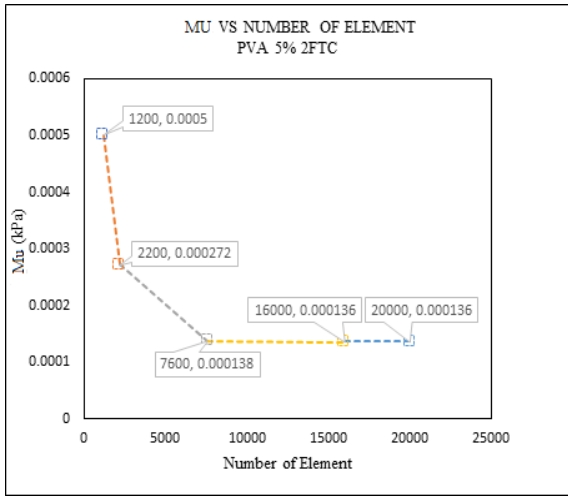
Figure 5.4: Graph of μ vs number of elements for PVA-C modeled with 5% concentration and finite thickness.
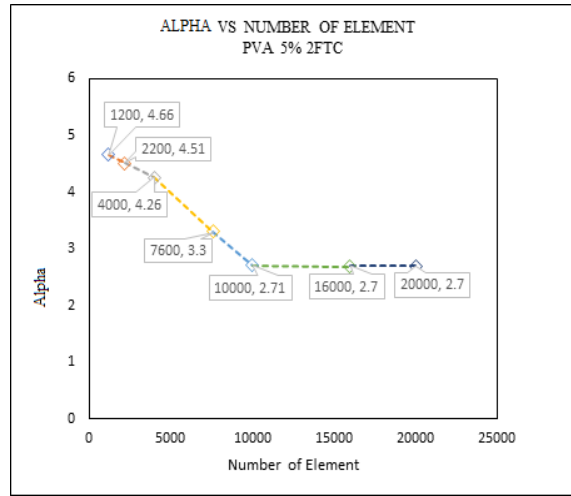
Figure 5.5: Graph of α vs number of elements for PVA-C modeled with 5% concentration and finite thickness.
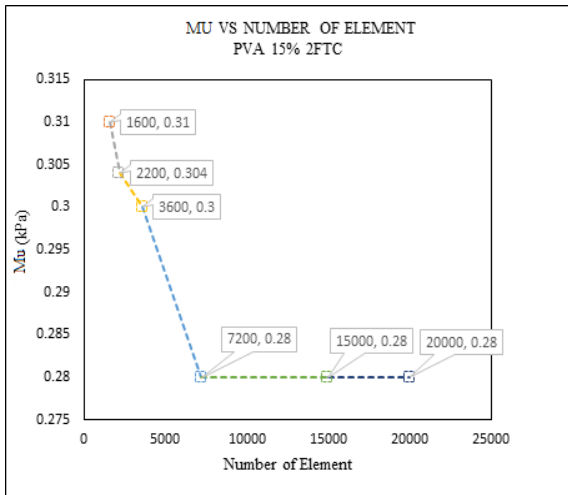
Figure 5.6: Graph of μ vs number of elements graph for PVA-C modeled with 15% concentration and finite thickness.
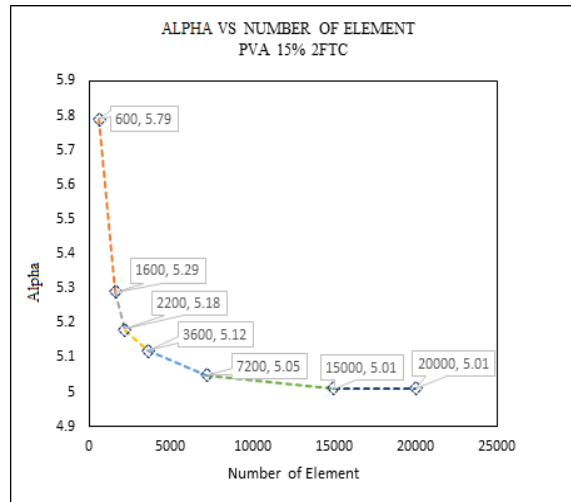
Figure 5.7: Graph of α vs number of elements for PVA-C modeled with 15% concentration and finite thickness.

5.5.3 Identification for Estimating Material Properties: A Novel Approach

Ogden model is used to identify the hyperelastic material properties. Levenburg-Marqardt (LM) algorithm was used to minimize the difference between experimental and model

Chapter 5: Soft Tissue Characterization using Inverse Finite Element Techniques

predicted data. Here, a novel approach is introduced to determine and validate material hyperelasticity. This method includes the following steps:

- Experimental data are used as an input for the Ogden hyperelasticity model.

- Numerical analysis is carried out with FEM (Abaqus) and the output of the load-displacement curve is recorded.

- This simulated load-displacement data are used as input for Levenburg-Marqardt (LM) optimization algorithm in MATLAB.

- Initial guess values (μ, α) are used for initializing the optimization algorithm.

- *MATLABR* Simulink: *R*2015*a* used @ *fminsearch* algorithm was used to fit the Ogden first order hyperelastic model shown in Equation: 5.2. Also, Levenburg-Marqardt (LM) optimization algorithm shown in Equation: 5.3 was used. The optimized parameters (μ, α) shown in Equation: 5.4 are recorded.

- These optimized parameters (μ, α) are inserted in FEA (Abaqus) for validation and verification of the inverse problem.

Through inverse analysis, extracted Ogden and Mooney-Rivlin parameters are readily available to use in simulation also to verify the stability of the solution. The detailed process was shown in the flow-chart of Figure: 5.3

5.5.4   Validation Exercise

FE simulated cylindrical load-displacement data was used in the robust optimization algorithm through inverse analysis. The entire procedure was shown as a flow-chart in Figure: 5.3. A validation exercise was conducted using Ogden parameters (μ) which was varied while kept α was constant and vice-versa as shown in Figure: 5.8 and Figure: 5.9 [26].

Chapter 5: Soft Tissue Characterization using Inverse Finite Element Techniques
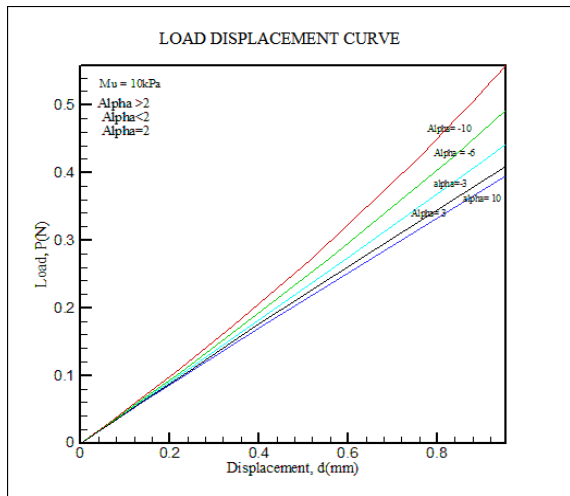
Figure 5.8: FE simulated Load-displacement graph for Ogden hyperelastic model. Material property α was kept constant and μ was varied.
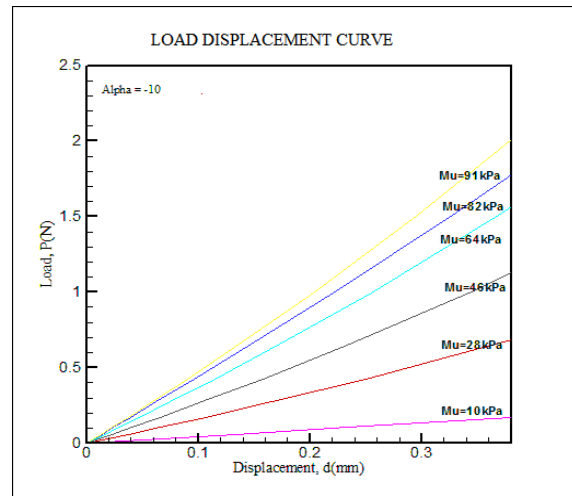
Figure 5.9: FE simulated Load-displacement graph for Ogden hyperelastic model. Material property α was varied and μ constant.

The results obtained from the load-displacement curve indicated that, there is a significant effect of (μ), as this parameter explains the strength of the material and (α) the strain hardening coefficient. In the process of validation μ and α values were compared with [26] and found good agreement.

5.6 Results

The performances of the novel model are illustrated in this section where 5% and 15% (w/w) soft tissue mimic data [38] were used in hyperelastic model. During the simulation, cylindrical, spherical and uniaxial indentation tests were conduction.

The hyperelastic model was simulated in Abaqus environment where, Ogden's first order constitutive model was used, and experimental data was fitted for parameter optimization. The indentation response from cylindrical indentation for 5% and 15% soft tissue mimics are shown in Figure: 5.10 and Figure:5.11. The results for indentation test using cylindrical indention are given below.

Chapter 5: Soft Tissue Characterization using Inverse Finite Element Techniques
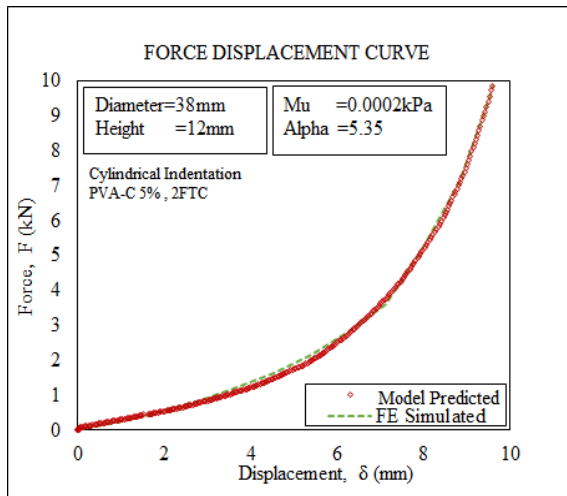
Figure 5.10: Load vs displacement graph for PVA-C sample with finite thickness and 5% concentration.
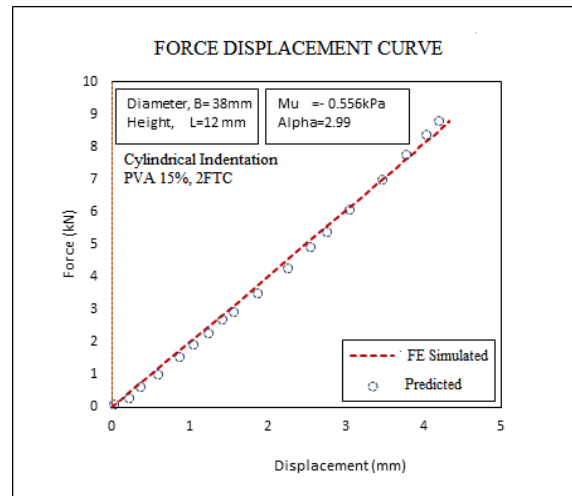
Figure 5.11: Load vs displacement graph for PVA-C sample with finite thickness and 15% concentration.

Experimental data obtained from [38] used as input parameter for FE simulated Ogden model. FE simulated and model predicted Load vs displacement curve for PVA-C, 2FTC 5% and 15% specimen are shown above. This process used optimization algorithm for the determination of material properties (μ, and α).

FE software Abaqus simulated indentation response from cylindrical indentation for 5% and 15% soft tissue mimics are used in the analysis. Ogden hyperelastic model is used in the analysis and the results for stress-stretch curve shown in Figure: 5.12 and Figure:5.13 are given below.

Chapter 5: Soft Tissue Characterization using Inverse Finite Element Techniques
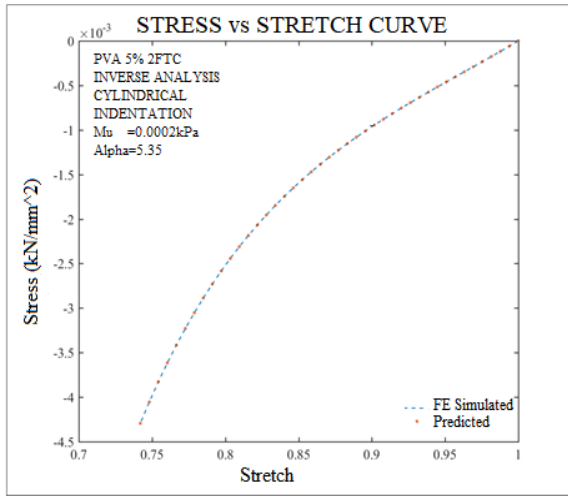
Figure 5.12: Stress-stretch graph for PVA-C samples with finite thickness and 5% concentrations.
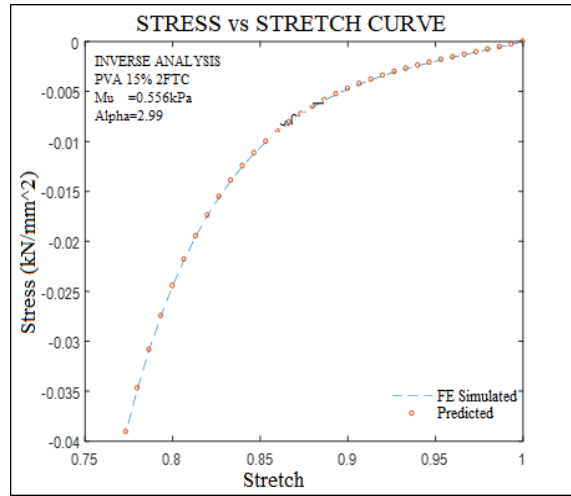
Figure 5.13: Stress-stretch graph for PVA-C samples with finite thickness and 15% concentrations.

Figure: 5.14 and Figure: 5.15 shows residual-stretch graph. It is defined by the proportion of variance (R-square) between the observed and the predicted data. FE simulated Ogden model used in optimization algorithm for the residual-stretch results. Experimental data used from cylindrical indentation at a concentration of (i) PVA-C 5%, 2FTC and (ii) PVA-C 15%, 2FTC.
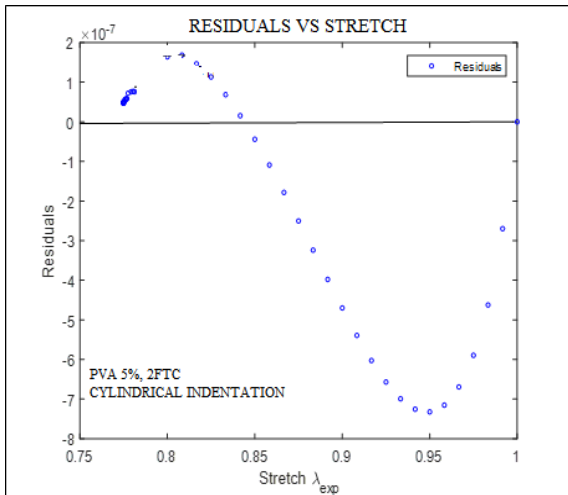
Figure 5.14: Residual vs stretch graph for PVA-C samples with (5%) concentrations where, fitness coefficient ($R^2 = 0.999$).
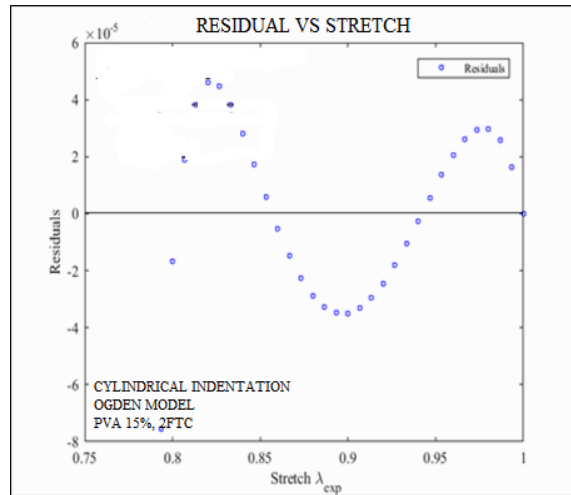
Figure 5.15: Residual vs stretch graph for PVA-C samples with (15%) concentrations where, $R^2 = 0.999$.

Chapter 5: Soft Tissue Characterization using Inverse Finite Element Techniques

5.6.1 Optimization Algorithm

A detailed flowchart of the inverse optimization process to characterize the tissue hyperelastic parameters used in the current study shown in Figure: 5.16.
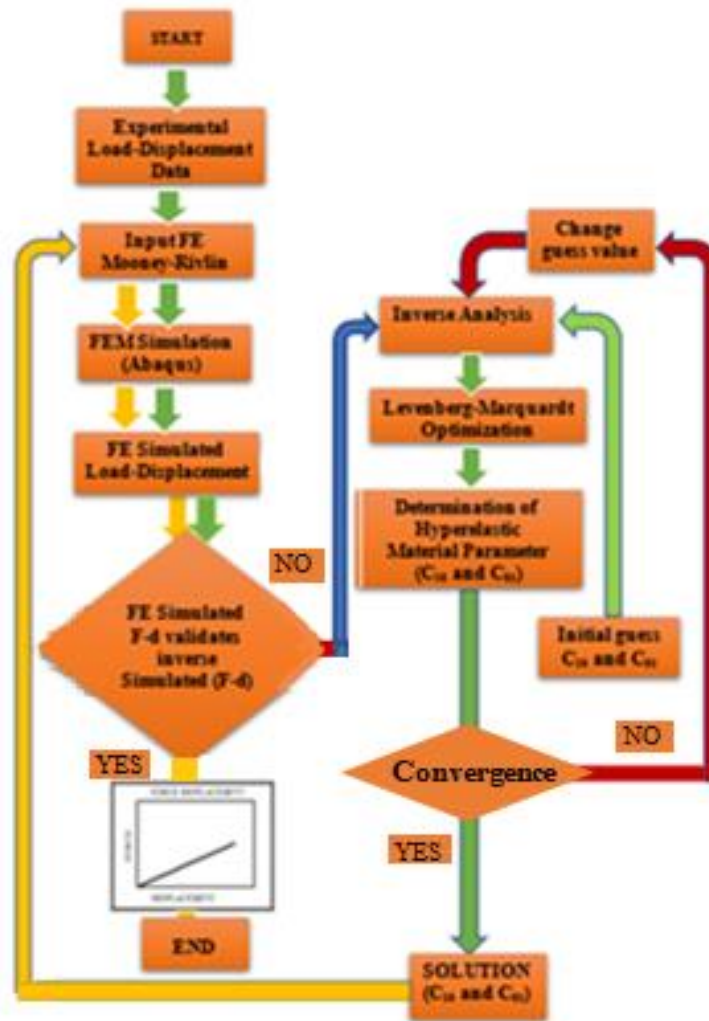
Figure 5.16: Flowchart of the inverse optimization process to characterize the unknown tissue hyperelastic parameters Mooney-Rivlin parameters. First, experimental (F-D) data used as an input parameter for the numerical model (Abaqus). Simulated (F-D) data then used as an input parameter for inverse analysis (MATLAB). An object junction introduced to minimize the quadratic difference between simulated and model predicted data. Through optimization process numerical convergence was achieved and optimized unknown parameter was obtained. These parameters were used as an input parameter of Abaqus for numerical validation.

Chapter 5: Soft Tissue Characterization using Inverse Finite Element Techniques

A set of simulated force-displacement data inserted in the optimization algorithm for identifying unknown Mooney-Rivlin material parameters. Fine mesh with spherical, the convergence analysis for PVA 15% 2FTC is shown in Figure: 5.17 and Figure:5.18.
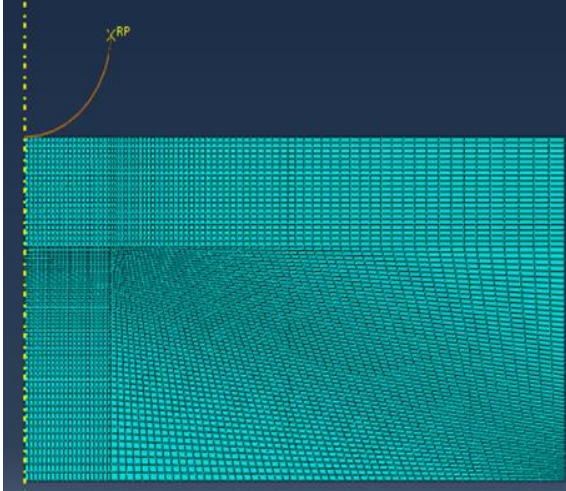
Figure 5.17: Very fine FE mesh with 7600 (CAX4RH) elements for indentation with spherical indenter
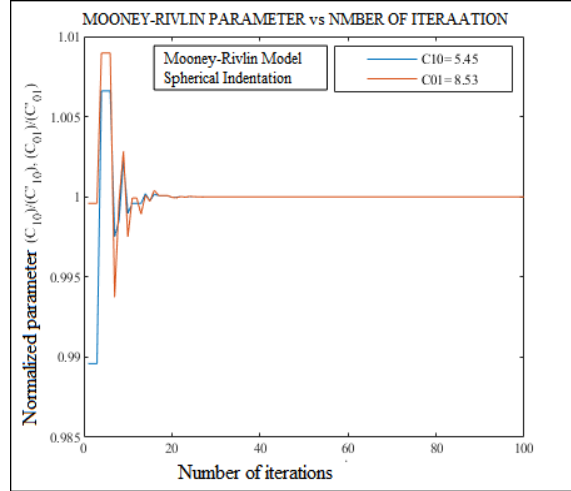
Figure 5.18: Graph of convergence between normalized C_{10} and C_{01} and number of iterations for spherical indentation of PVA-C 5%. [38]

FE simulated load-displacement contours and convergence analysis for cylindrical indentation are shown in Figure: 5.19 and Figure:5.20.
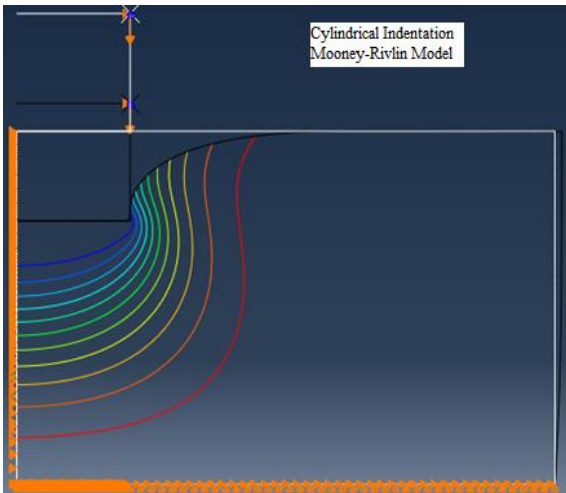
Figure 5.19: Force-displacement contours with optimal C_{10} and C_{01} values obtained from the FE inverse algorithm
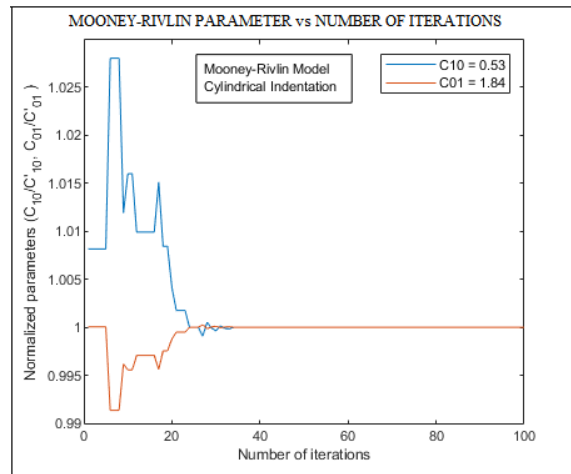
Figure 5.20: Graph of convergence between normalized C_{10} and C_{01} and number of iterations for spherical indentation of PVA-C 5% [38].

Chapter 5: Soft Tissue Characterization using Inverse Finite Element Techniques

A set of simulated force-displacement data inserted in the optimization algorithm for identifying unknown Mooney-Rivlin material parameters. Fine mesh for uniaxial testing and the convergence analysis for PVA 5% 2FTC are shown in Figure: 5.21 and Figure:5.22.
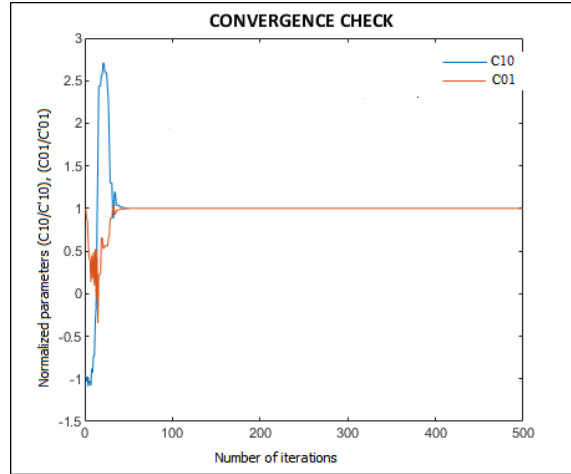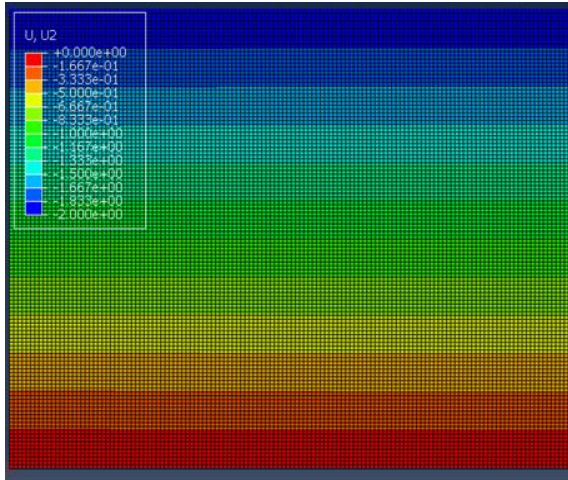
Figure 5.21: Force displacement contours for uniaxial testing is shown. The date was used for identifying unknown Mooney-Rivlin parameters.

Figure 5.22: Graph of convergence between normalized C_{10} and C_{01} and number of iterations for uniaxial indentation of PVA-C 5%. [38]

Force-displacement graph is compared through optimization algorithm. The simulated force-displacement data was used as input parameter for the inverse optimization algorithm. PVA-C at a concentration of 5% and 15% rest results used as an input parameter for Ogden model shown in Figure: 5.23 and Figure:5.24.
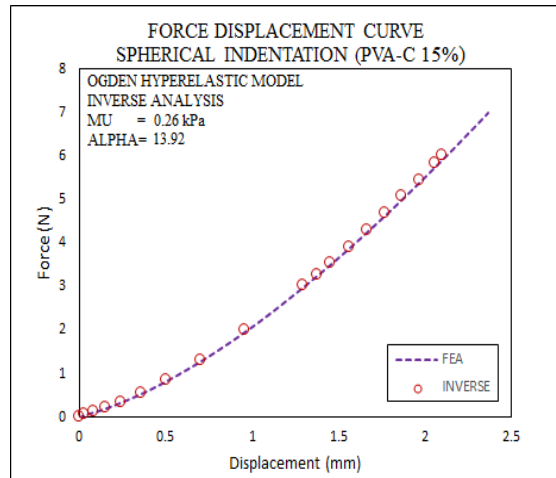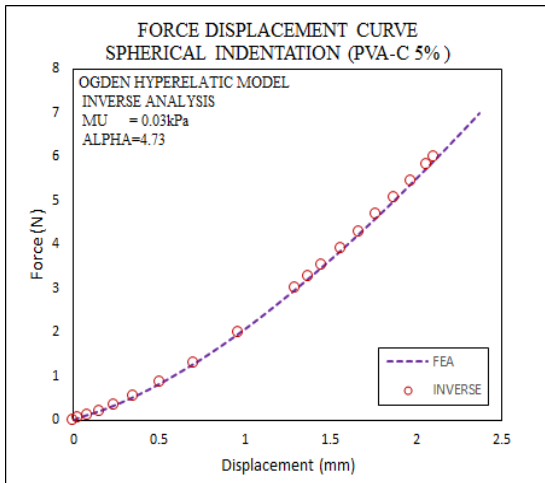
Chapter 5: Soft Tissue Characterization using Inverse Finite Element Techniques

Figure 5.23: Force-displacement graph with fitted graph with optimal (μ,α) values obtained from the FE inverse algorithm.

Figure 5.24: Force-displacement graph with fit- ted graph with optimal (μ,α) values obtained from the FE inverse algorithm

Graph of convergence for uniaxial testing and residuals for PVA-C at a concentration of 5% shown in Figure: 5.25 and Figure:5.26.
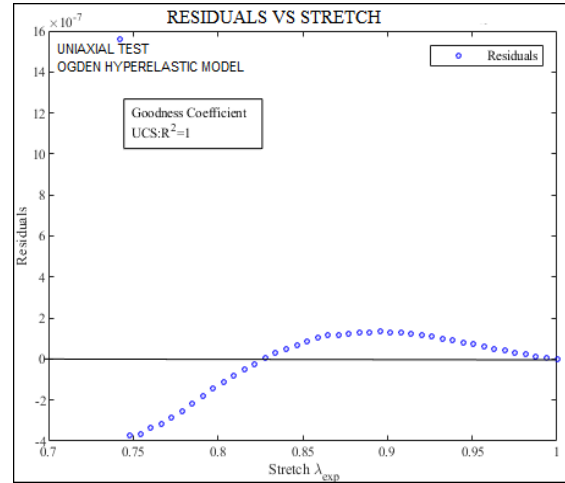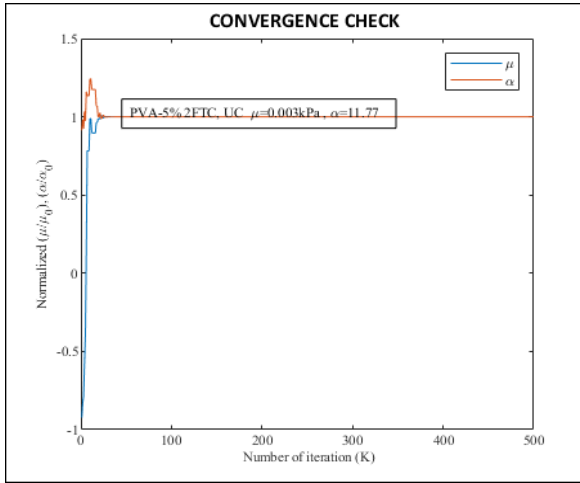
Figure 5.25: Graph of convergence between normalized (μ/μ_0), (α/α_0) and number of iterations for UCS of PVA-C 5%.

Figure 5.26: Residuals vs stretch graph for uniaxial testing of PVA-C 5%, 2FTC. Results shows R^2=1.

Stress-strain and stress-stretch graph of uniaxial testing for PVA-C at a concentration of 5% shown in Figure: 5.27 and Figure:5.28.
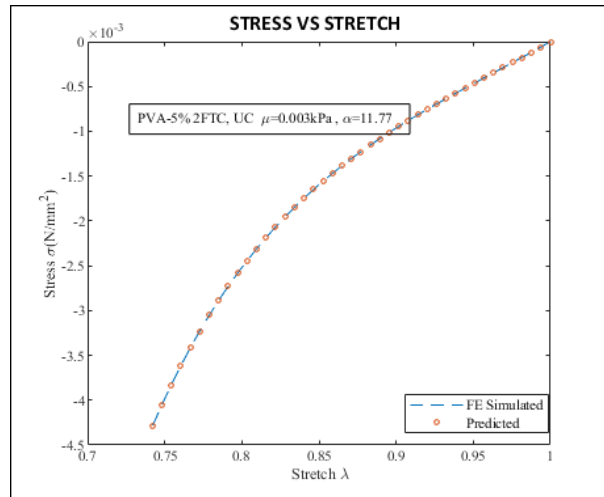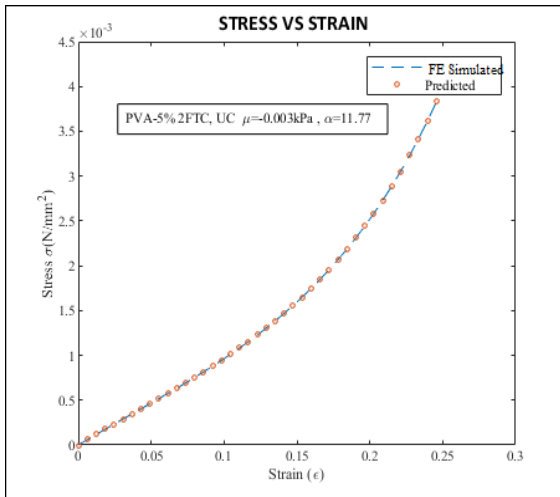
Figure 5.27: Stress-strain curve for uniaxial testing of PVA-C 5%, 2FTC. Experimental data was provided by [38].

Figure 5.28: Stress-stretch curve for uniaxial testing of PVA-C 5%, 2FTC. Experimental data was provided by [38].

Chapter 5: Soft Tissue Characterization using Inverse Finite Element Techniques

5.6.2 Effect of μ and α on Thickness

FE software Abaqus simulated force-displacement data are used as input parameter for inverse optimization algorithm using MATLAB for the determination of Ogden parameters which are plotted against various concentration of PVA-C 5%, 2FTC and PVA-C 15%, 2FTC shown in Figure: 5.29, Figure: 5.30 and Figure:5.31, Figure:5.32.
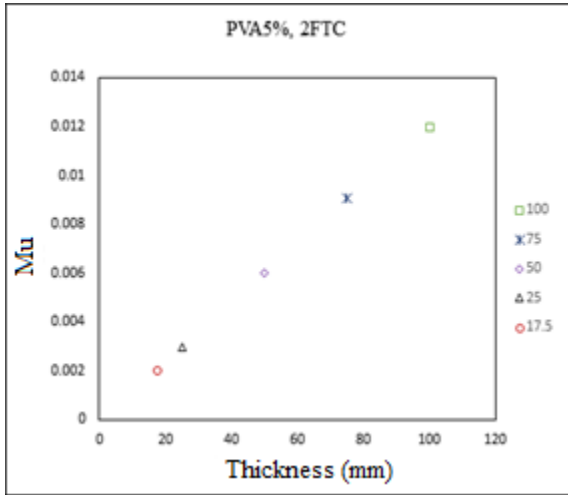
Figure 5.29: Graph of μ vs various thickness for PVA-C 5%, 2FTC.
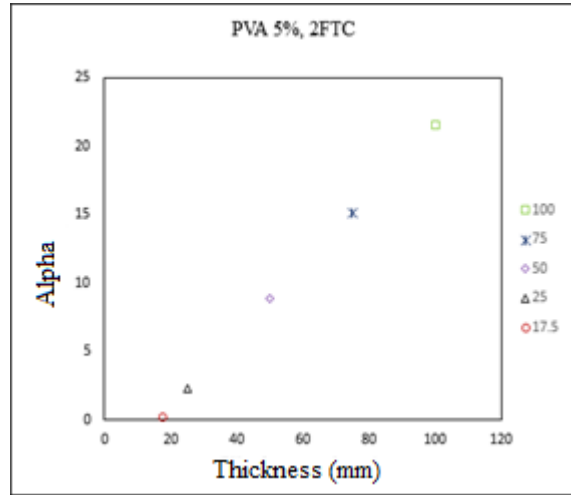
Figure 5.30: Graph of α vs various thickness for PVA-C 5%, 2FTC
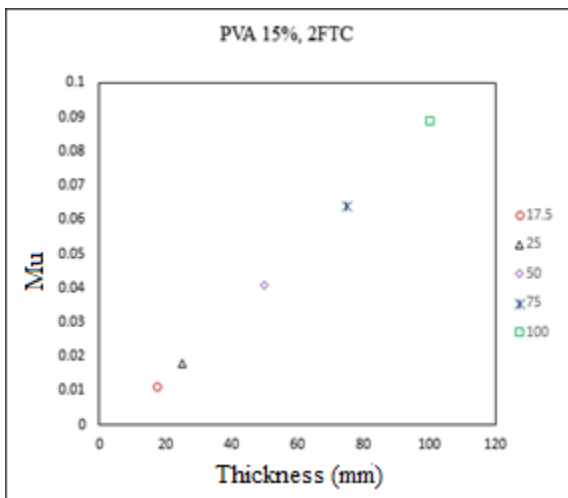
Graph of μ vs various thickness for PVA-C 15%, 2FTC.
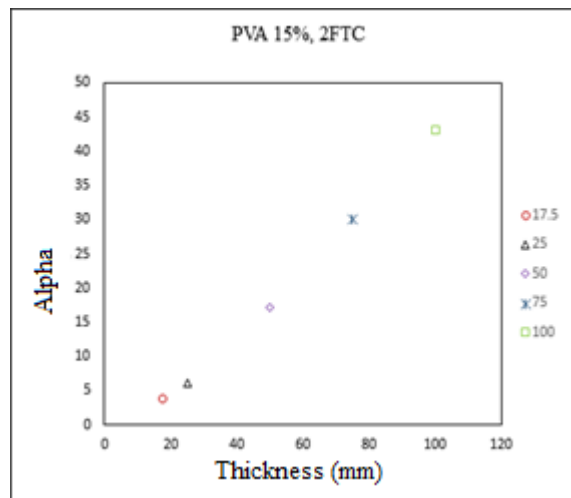
Figure 5.32: Graph of α vs various thickness for PVA-C 15%, 2FTC.

Chapter 5: Soft Tissue Characterization using Inverse Finite Element Techniques

It can be hypothesized that (μ, α) values has a greater dependency on thickness. As the thickness increases both (μ, α) increases

5.6.3 Effect of Concentration and Freeze Thaw Cycle on μ and α

The extracted Ogden parameters from inverse optimization algorithm are plotted against concentration and freeze thaw cycles shown in Figure: 5.33, Figure: 5.34, Figure:5.35 and Figure:5.36.
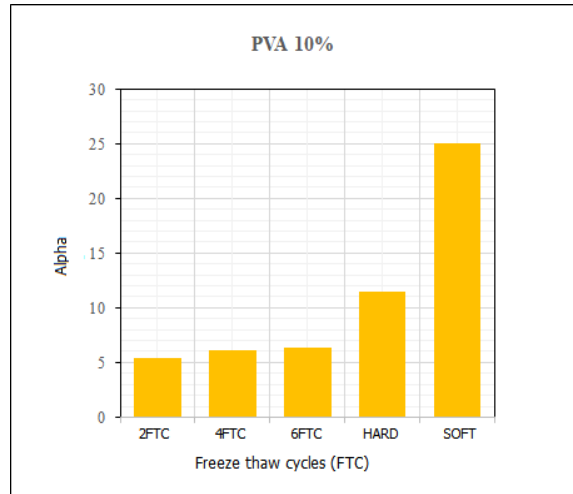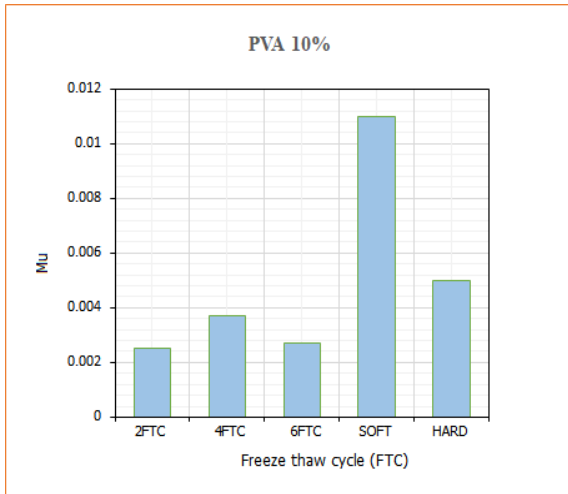
Figure 5.33: Graph of μ vs various number of PVA-C concentrations.

Figure 5.34: Graph of α vs various number of PVA-C concentrations.
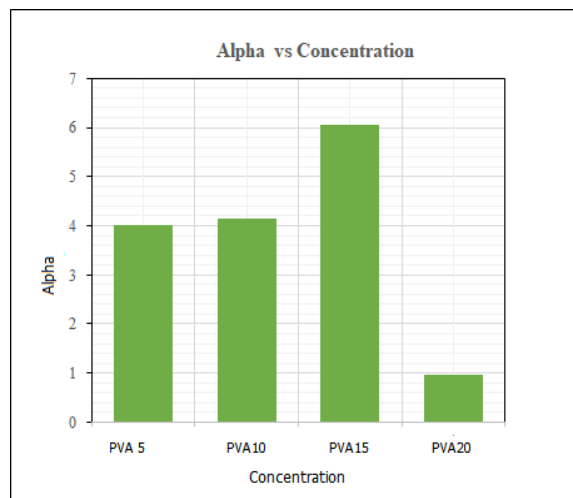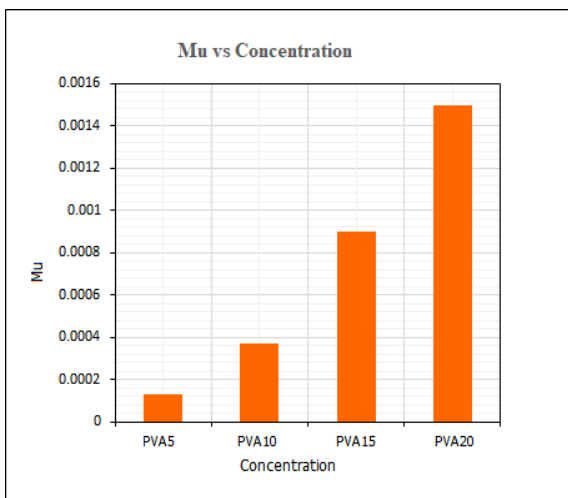
Figure 5.35: Graph of μ vs various number of PVA-C concentrations.

Figure 5.36: Graph of α vs various number of PVA-C concentrations.

Chapter 5: Soft Tissue Characterization using Inverse Finite Element Techniques

This result led us to the conclusion that, there is a proportional relationship between (μ, α) values and PVA-C concentration also freeze-thaw cycles. With the increase of PVA-C concentration (μ, α) increases also, Also, with the increase of freeze-thaw cycle time (FTC) the values of (μ, α) increases.

5.7   Sensitivity Analysis: Cylindrical Indentation

In order to overcome stability problem sensitivity analysis was conducted by adding (± 1%) and ±2 %) noise to the solutions. This noise modulation with the input data will enable us to investigate whether there is any extraneous influence on material, equipment etc. Fellay et al. considered this problem as another minimization approach.

After determining optimal material parameters, sensitivity analysis of the solution was analyzed by adding (±1% and ± 2%) noise to the iterative solutions. A typical sensitivity plot of soft tissue mic (PVA-C 5%) is shown in Figure: 5.37 and Figure: 5.38.
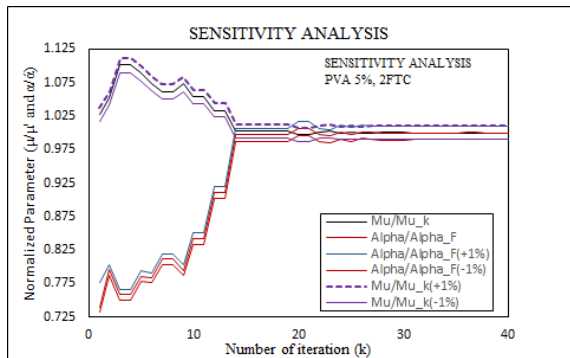
Figure 5.37: Normalized parameters (μ, α) of 15% PVA-C with respect to the number of iterations. Two levels ((+1%) and (-1%)) of noise were added to Ogden parameters.
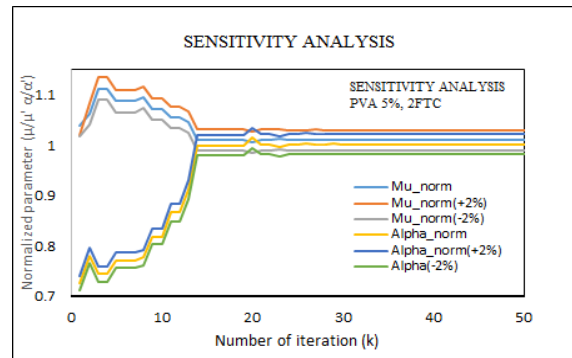
Figure 5.38: Shows normalized parameter (μ, α) with respect to the number of iterations. Two levels ((+2%) and (-2%)) of noise were added to Ogden parameters.

Based on Hadamard's [167] paper solution of any inverse problem continuously depends on the stability of the data [118]. The sensitivity of the solution indicates that, there was no external influence in the solution. Which also again proved the uniqueness of the solution.

Chapter 5: Soft Tissue Characterization using Inverse Finite Element Techniques

5.8 Sensitivity Analysis: Spherical Indentation

Sensitivity analysis of the solution was performed by adding ($\pm 2\%$) noise to the iterative solutions. A typical sensitivity plot soft tissue mic (PVA-C 5%) is shown in Figure: 5.39 and Figure: 5.40.
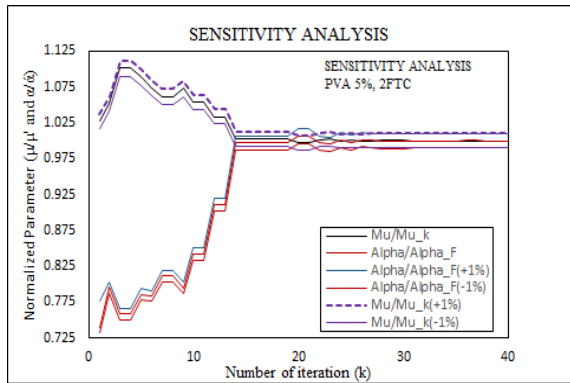
Figure 5.39: Normalized parameter (μ, α) with respect to the number of iterations. Two levels ((+2%) and (-2%)) of noise were added to Ogden parameters.
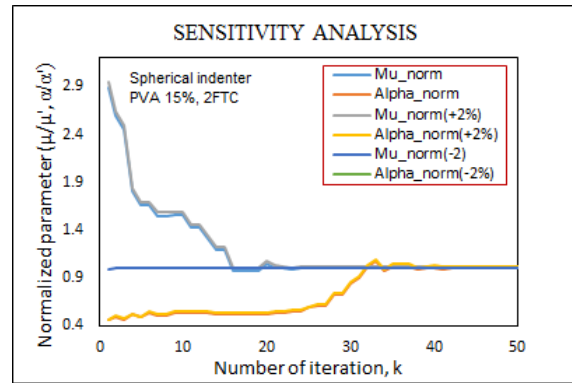
Figure 5.40: Normalized parameter (μ, α) with respect to the number of iterations. Two levels ($\pm 2\%$) of noise were added to Ogden parameters.

Based on Hadamard's [167] paper solution of any inverse problem continuously depends on the stability of the data [118]. The sensitivity solution indicates that the current solution table under reasonable amount of noise.

Chapter 5: Soft Tissue Characterization using Inverse Finite Element Techniques

5.9 Summary

Before conducting any surgical procedures, planning for bio-material research or any other field where applicable, unique identification of material properties essential. The accuracy, effectiveness and robustness of such procedures needs verification [11] with FE simulated data.

The objective of the study was to characterize non-linear behaver of soft tissue phantom. The combination of the inverse method in conjunction with the finite element method enables identification of unknown material parameters. The Levenberg-Marquardt optimization algorithm was used to optimize material properties and minimize the sum of squared differences between the model predicted and experimentally measured load-displacement data and provide bench- marks for accurate Ogden parameters (μ, α). The accuracy, effectiveness and robustness of such procedures were validated through FE simulated data and cross checked by the robust technique and compared with published results.

The simulated data were used as an input parameter for MATLAB optimization algorithm. The robust optimization technique performed as expected, which conformed the uniqueness of the solution. Secondly, the Ogden parameters were plotted at various thicknesses. This proved that, μ, and α has a significant effect on specimen thickness. Also, μ, and α were plotted against concentration and freeze thaw cycles. Simulated result confirmed the dependency of μ, and α on PVA concentration and freeze thaw cycles. Which means the value of μ, and α increases with the increase of concentration and freeze thaw cycles with little exception of PVA at higher concentration.

R-squared values for 5% and 15% PVA-C, 2FTC were obtained through parameter estimation technique. Their fitness coefficient was 0.99999 and 0.9998. This led us to conclude that, the optimization algorithm provided accurate results in the determination of Ogden parameter and Mooney-Rivlin parameters. Finally, PVA-C of 5%, 15% has undergone sensitivity test by adding y $\pm1\%$, $\pm 2\%$ noise to the solution. No extraneous effect was observed. Thus, the solution proved the uniqueness.

Chapter 5: Soft Tissue Characterization using Inverse Finite Element Techniques

The novel algorithm provided in Appendix A.8 provides an opportunity to validate results and estimate optimized (μ,α) parameters for Ogden and (C_{10}. C_{01}) parameters for Mooney-Rivlin hyperelastic material model. These extracted parameters were assessed with FE software Abaqus for the numerical accuracy. It can be concluded that the proposed technique can be used effectively to estimate and validate Ogden and Mooney-Rivlin parameters for numerical accuracy.

Chapter 6

6.1 Contribution and Conclusions

This chapter presents a discussion on the findings of the research presented in this dissertation. It will conclude with the contributions of this research and propose recommendations for future research.

A numerical study was conducted to characterize non-linear mechanical properties of polyvinyl alcohol cryogel (PVA-C). A range of PVA-C phantom data was analyzed in the numerical study. The force-displacement data were recorded and used in FEA studies for experimental data validations and material characterizations.

1. The developed finite element model (FE) can be utilized to determine the distribution of resulting stresses of linear and nonlinear elastic thin-structured materials for a given load. Since this FE model incorporates influence factor (I_F), the stress distribution could be computed up to 36% (with $I_F = 1$, and $I_F = 0.637$) more reliably.

2. Introduction of friction coefficient (Ω) in the developed analytical model provides up to 23% difference in magnitude of the functional parameter k used in different standard models such as Zhang's, Cao's and Hayes' model. Thus, the proposed analytical solution can potentially provide an improved understanding of the indentation response of soft tissues.

3. The developed inverse algorithm is suitable to identify few biomechanical properties (e.g. Ogden and Mooney-Rivlin parameters) for new development of artificial materials (e.g. scaffolding, tissue generation, phantoms for surgical training etc.).

4. Overall, the finite element model, the analytical model and the inverse algorithm developed in this study would provide an important tool in the design and characterization of soft tissue materials.

Chapter 6: Contribution and Conclusions

The central aim of this research project was to develop robust methods to identify nonlinear elastic material properties of PVA-C and other soft materials using hyperelastic models as discussed in chapter 4 and 5. To address each of those objectives, indentation responses from cylindrical, spherical and uniaxial testing were investigated. As well as a robust technique was developed for optimizing and characterizing nonlinear material properties using an Ogden and Mooney-Rivlin hyperelastic material model for a range of soft, artificial, and natural materials.

In chapter 3, an axisymmetric numerical model was developed for the cylindrical indentation in order to study material characterization of soft biological tissues. Mesh optimization technique was introduced for optimal numerical accuracy. The effect of the coefficient of friction was investigated. Validation of Hertz, Boussinesq's, Sneddon's analytical solutions were conducted using numerical analysis. Distribution of stress of different specimen thickness were investigated. The effect of influence factor I_F for a range of parameters was discussed.

Chapter 4 discussed about the indentation responses from non-linear materials. A numerical analysis (FEM) for finite and infinite thick, soft tissues were presented. This analysis examined the uniqueness of Sneddon's, Cao's, Zhang's model and presented our FE simulated results by comparing with their published results. Thus, providing a more precise result which was determined by the R-square analysis. A novel analytical approach was developed by adding a new parameter called friction coefficient Ω as a function of k in Zhang's solution [25]. This new approach showed a great potential to investigate the mechanical responses of finite thick biological tissues.

Chapter 5 focused on developing numerical models that incorporates finite thick biological soft tissues and phantoms with cylindrical, spherical and uniaxial indenters. Inverse analysis was used to extract unknown material properties. Since, there was no straightforward method available to extract unknown material properties from experimental data, a robust technique was developed by using "optimization algorithm". This robust method is capable of extracting unknown parameter with maximum numerical accuracy and least computational time. This method also examines (i) convergence (ii) experimental vs model predicted data (iii) optimized and provide Ogden, Mooney-Rivlin parameters, and (iv) stability analysis. The extracted

Chapter 6: Contribution and Conclusions

parameters are readily available to use in FEA simulation to verify and validate the uniqueness and stability of the solution.

6.2 Future Research Recommendations

The current work can be expanded in future in several ways.

- The experimental data [38] used in two-dimensional indentation test using finite element method (Abaqus) can be used as standard case. The novel analytical technique can be utilized to investigate the effect of friction in tissue mechanics.

- A new technique has been developed to characterize the bio-mechanical properties of non-linear material using Ogden and Mooney-Rivlin hyperelastic model. In the future, this technique can be further investigated to develop patient specific artificial organs.

- This study was conducted using cylindrical, spherical and uniaxial indentation. Since indenter shape plays an important role in stress distribution, other types of indenters including, conical and nano indentation test could be used for future research.

- The current research conducted can be expanded in the future in various ways. This includes the experimental data used in two-dimensional indentation test using finite element method (Abaqus) which can be used as benchmark analysis. The novel analytical technique can also be exercised to investigate the effect of friction in biological materials.

- A new technique has been developed to characterize the biomechanical properties of nonlinear material using Ogden and Mooney-Rivlin hyperelastic model. In future research, this technique can be further explored to help develop patient specific artificial organs, which can replace the need for human organ transplantations.

It is hoped that, the present research will help to improve material characterization accuracy through indentation tests.

Chapter 7

Appendixes

Chapter 7: Appendix

Appendix A.1

z/b	s/b								
	0	0.2	0.4	0.6	0.8	1	1.2	1.5	2
0	0	0	0	0	0	0	0	0	0
0.1	.09852	.10140	.11138	.13424	.18796	.05388	-.07899	-.02672	-.00845
0.2	.18857	.19306	.20772	.23524	.25983	.08513	-.07759	-.04448	-.01593
0.3	.26362	.26787	.28018	.29483	.27257	.10757	-.04316	-.04999	-.02166
0.4	.32016	.32259	.32748	.32273	.26925	.12404	-.00766	-.04535	-.02522
0.5	.35777	.35752	.35323	.33106	.26236	.13591	.02165	-.03455	-.02651
0.6	.37831	.37531	.36308	.32822	.25411	.14440	.04457	-.02101	
0.7	.38487	.37962	.36072	.31929	.24638	.14986	.06209	-.000702	-.02329
0.8	.38091	.37408	.35133	.30699	.23779	.15292	.07530	.00614	
0.9	.36962	.36275	.33734	.29299	.22891	.15404	.8507	.01795	
1	.35355	.34553	.32075	.27819	.21978	.15355	.09210	.02814	-.01005

z/b	s/b								
	3	4	5	6	7	8	10	12	14
0	0	0	0	0	0	0	0	0	0
0.1	.00211	.00084	.00042						
0.2	.00419	.00167	.00083	.00048	.00030	.00020			
0.3	.00622	.00250							
0.4									
0.5	.01013	.00407	.00209	.00118	.00071	.00053	.00025	.00014	.00009
0.6									
0.7									
0.8									
0.9									
1	.01742	.00761	.00393	.00226	.00143	.00097	.00050	.00029	.00018
1.2	.01935	.00871	.00459	.00269	.00171	.00115			
1.5	.02142	.01013	.00548	.00325	.00210	.00141	.00073	.00043	.00027
2	.02221	.01160	.00659	.00399	.00264	.00180	.00094	.00056	.00036
2.5	.02143	.01221	.00732	.00463	.00308	.00214	.00115	.00068	.00043
3	.01980	.01220	.00770	.00505	.00346	.00242	.00132	.00079	.00051
4	.01592	.01109	.00768	.00536	.00384	.00282	.00160	.00099	.00065
5	.01249	.00949	.00708	.00527	.00394	.00298	.00179	.00113	.00075
6	.00983	.00795	.00628	.00492	.00384	.00299	.00188	.00124	.00084
7	.00784	.00661	.00548	.00445	.00360	.00291	.00193	.00130	.00091
8	.00635	.00554	.00472	.00398	.00332	.00276	.00189	.00134	.00094
9	.00520	.00466	.00409	.00353	.00301	.00256	.00184	.00133	.00096
10	.00438	.00397	.00352	.00326	.00273	.00241			

z/b	s/b								
	3	4	5	6	7	8	10	12	14
0	0	0	0	0	0	0	0	0	0
0.1	-.00210	-.00084	-.00042						
0.2	-.00412	-.00166	-.00083	-.00024	-.00015	-.00010			
0.3	-.00599	-.00245							
0.4									
0.5	-.00991	-.00388	-.00199	-.00116	-.00073	-.00049	-.00025	-.00014	-.00009
0.6									
0.7									
0.8									
0.9									
1	-.01115	-.00608	-.00344	-.00210	-.00135	-.00092	-.00048	-.00028	-.00018

z/b	s/b								
	0	0.2	0.4	0.6	0.8	1	1.2	1.5	2
1.2	.31485	.30730	.28481	.24836	.20113	.14915	.10002	.04378	.00023
1.5	.25602	.25025	.23338	.20694	.17368	.13732	.10193	.05745	.01385
2	.19889	.18144	.16644	.15198	.13375	.11331	.09254	.06371	.02836
2.5	.12807	.12633	.12126	.11327	.10298	.09130	.07869	.06022	.03429
3	.09487	.09394	.09099	.08635	.08033	.07325	.06551	.05354	.03511
4	.05707	.05666	.05562	.05383	.05145	.04773	.04532	.03995	.03066
5	.03772	.037760				.03384			.02474
6	.02666					.02468			.01968
7	.01980					.01868			.01577
8	.01526					.01459			.01279
9	.01212								.01054
10								.00924	.00879

Chapter 7: Appendix

Appendix A.2

Table 2: Indentation Factor and Aspect Ratio at Friction coefficient (Ω) =1

	Poisson's ratio , v=0.3					Poisson's ratio , v=0.35			
a/h	A=w1/h	μ1a²2	B= P/˝μa²2	C=A/B	a/h	A=w1/h	μ1a²2	B= P/˝μa²2	C=A/B
0	0			0	0	0			0
0.2	0.0286565	0.615384615	0.975	0.029391282	0.2	0.027229	0.592592593	1.0125	0.02689284
0.4	0.0473934	0.615384615	0.975	0.048608615	0.4	0.0447232	0.592592593	1.0125	0.044171062
0.59970015	0.057131634	0.615384615	0.975	0.058596548	0.59970015	0.053743628	0.592592593	1.0125	0.053080127
1	0.0705355	0.615384615	0.975	0.072344103	1	0.06463375	0.592592593	1.0125	0.063835802
1.500375094	0.075579895	0.615384615	0.975	0.077517841	1.500375094	0.067752813	0.592592593	1.0125	0.066916359
2	0.0783	0.615384615	0.975	0.080307692	2	0.0695	0.592592593	1.0125	0.068641975
4	0.0934	0.615384615	0.975	0.095794872	4	0.08374	0.592592593	1.0125	0.082706173
8	0.08804	0.615384615	0.975	0.090297436	8	0.07618	0.592592593	1.0125	0.075239506
10	0.11005	0.5552	1.080691643	0.101832933	10	0.07475	0.592592593	1.0125	0.07382716

	Poisson's ratio , v=0.4					Poisson's ratio , v=0.45			
a/h	A=w1/h	μ1a²2	B= P/˝μa²2	C=A/B	a/h	A=w1/h	μ1a²2	B= P/˝μa²2	C=A/B
0	0			0	0	0			0
0.2	0.0254415	0.571428571	1.05	0.02423	0.2	0.0231575	0.551724138	1.0875	0.021294253
0.4	0.0414992	0.571428571	1.05	0.039523048	0.4	0.037612	0.551724138	1.0875	0.034585747
0.59970015	0.049311094	0.571428571	1.05	0.046962947	0.59970015	0.043576912	0.551724138	1.0875	0.040070723
1	0.05723375	0.571428571	1.05	0.054508333	1	0.04794175	0.551724138	1.0875	0.044084368
1.500375094	0.058246062	0.571428571	1.05	0.05547244	1.500375094	0.046893848	0.551724138	1.0875	0.04312078
2	0.05885	0.571428571	1.05	0.056047619	2	0.045615	0.551724138	1.0875	0.041944828
4	0.06886	0.571428571	1.05	0.065580952	4	0.04912	0.551724138	1.0875	0.045167816
8	0.06014	0.571428571	1.05	0.05727619	8	0.03822	0.551724138	1.0875	0.035144828
10	0.0586	0.571428571	1.05	0.055809524	10	0.036675	0.551724138	1.0875	0.033724138

	Poisson's ratio , v=0.5			
a/h	A=w1/h	μ1a²2	B= P/˝μa²2	C=A/B
0	0			0
0.2	0.0200805	0.533333333	1.125	0.017849333
0.4	0.0322954	0.533333333	1.125	0.028707022
0.59970015	0.036236582	0.533333333	1.125	0.032210295
1	0.03689775	0.533333333	1.125	0.032798
1.500375094	0.032763691	0.533333333	1.125	0.029123281
2	0.02889	0.533333333	1.125	0.02568
4	0.02325	0.533333333	1.125	0.020666667
8	0.008064	0.533333333	1.125	0.007168
10	0.0057725	0.533333333	1.125	0.005131111

Chapter 7: Appendix

Appendix A.3

Friction Coefficient =0 and w/h=0.1 Percent

a/h	v=0.30 We	Ming	Hayes	v=0.35 We	Ming	Hayes	v=0.40 We	Ming	Hayes
0.2	1.187266243	1.218	1.207	1.206028631	1.222	1.218	1.236744261	1.227	1.232
0.4	1.435965411	1.513	1.472	1.469029018	1.54	1.502	1.51709623	1.575	1.542
0.6	1.766761584	1.82	1.784	1.808035714	1.87	1.839	1.881995872	1.937	1.917
1	2.360611511	2.52	2.48	2.486774986	2.2616	2.603	2.682997462	2.777	2.789
1.5	3.311676023	3.479	3.4	3.546237822	3.712	3.629	3.927460429	4.082	3.996
2	4.202793241	4.429	4.335	4.556043226	4.782	4.685	5.158648925	5.368	5.271

Friction Coefficient =0 and w/h=0.1 Percent

a/h	v=0.45 We	Ming	Hayes	v=0.50 We	Ming	Hayes
0.2	1.291001785	1.233	1.252	1.400629972	1.244	1.281
0.4	1.590377303	1.625	1.599	1.711807669	1.698	1.698
0.6	2.014099115	2.035	2.031	2.262507139	2.183	2.211
1	3.011873769	3.064	3.085	3.622955043	3.59	3.609
1.5	4.612243796	4.734	4.734	6.082067362	6.078	5.97
2	6.330778618	6.478	6.38	9.310447564	9.11	9.069

Friction Coefficient =0 and w/h=10 Percent

a/h	v=0.30 We	Ming	v=0.35 We	Ming	v=0.40 We	Ming	v=0.45 We	Ming	v=0.50 We	Ming
0.2	1.187260047	1.224	1.206028631	1.242	1.236744261	1.268	1.291001785	1.304	1.402515802	1.356
0.4	1.436176929	1.52	1.469029018	1.565	1.51709623	1.626	1.590377303	1.706	1.711807669	1.845
0.6	1.768134715	1.837	1.808035714	1.914	1.881995872	2.025	2.014099115	2.181	2.262507139	2.45
1	2.360611511	2.604	2.486774986	2.759	2.682997462	2.99	3.011873769	3.362	3.622955043	4.106
1.5	3.311676023	3.616	3.546237822	3.908	3.927460429	4.596	4.612243796	5.317	6.082067362	7.509
2	4.202793241	4.625	4.556043226	5.054	5.158648925	5.8	6.330778618	7.307	9.310447564	11.555

Friction Coefficient =0 and w/h=15 Percent

a/h	v=0.30 We	Ming	v=0.35 We	Ming	v=0.40 We	Ming	v=0.45 We	Ming	v=0.50 We	Ming
0.2	1.187399818	1.224	1.20612883	0.255	1.236802532	1.281	1.291019433	1.334	1.40062881	1.42
0.4	1.43631999	1.521	1.469247656	1.572	1.51712911	1.635	1.590363208	1.751	1.713545898	1.932
0.6	1.768745681	1.839	1.810356684	1.929	1.884057682	2.05	2.016650183	2.26	2.266828938	2.606
1	2.364045722	2.618	2.490243982	2.798	2.687017865	3.075	3.017683563	3.522	3.633658335	4.381
1.5	3.315789474	3.699	3.551685741	4.025	3.935007828	4.577	4.623390912	5.632	6.103029996	8.396
2	4.209082985	4.738	4.563868149	5.208	5.168905614	6.04	6.345749873	7.761	9.342198503	13.052

Chapter 7: Appendix

Appendix A.4

Table 4 : Data obtained at different Poisson's and Aspect ratios compared k values with Zhang and Hayes model at Zero Friction Coefficient.

	Friction Coefficent =0 and Relative indentation depth (w/h) =0.1 Percent									
	v=0.30		v=0.35		v=0.40		v=0.45		v=0.50	
a/h	We	Ming	We	Ming	We	Ming	We	Ming	We	Ming
0.2	1.187266243	1.218	1.206028631	1.222	1.236744261	1.227	1.291001785	1.233	1.400629972	1.244
0.4	1.435965411	1.513	1.469029018	1.54	1.51709623	1.575	1.590377303	1.625	1.711807669	1.698
0.6	1.766761584	1.82	1.808035714	1.87	1.881995872	1.937	2.014099115	2.035	2.262507139	2.183
1	2.360611511	2.52	2.486774986	2.2616	2.682997462	2.777	3.011873769	3.064	3.622955043	3.59
1.5	3.311676023	3.479	3.546237822	3.712	3.927460429	4.082	4.612243796	4.734	6.082067362	6.078
2	4.202793241	4.429	4.556043226	4.782	5.158648925	5.368	6.330778618	6.478	9.310447564	9.11
	Friction Coefficent =0 and Relative indentation depth (w/h) =10 Percent									
	v=0.30		v=0.35		v=0.40		v=0.45		v=0.50	
a/h	We	Ming	We	Ming	We	Ming	We	Ming	We	Ming
0.2	1.187260047	1.224	1.206028631	1.242	1.236744261	1.268	1.291001785	1.304	1.402515802	1.356
0.4	1.436176929	1.52	1.469029018	1.565	1.51709623	1.626	1.590377303	1.706	1.711807669	1.845
0.6	1.768134715	1.837	1.808035714	1.914	1.881995872	2.025	2.014099115	2.181	2.262507139	2.45
1	2.360611511	2.604	2.486774986	2.759	2.682997462	2.99	3.011873769	3.362	3.622955043	4.106
1.5	3.311676023	3.616	3.546237822	3.908	3.927460429	4.596	4.612243796	5.317	6.082067362	7.509
2	4.202793241	4.625	4.556043226	5.054	5.158648925	5.8	6.330778618	7.307	9.310447564	11.555
	Friction Coefficent =0 andRelative indentation depth (w/h) =15 Percent									
	v=0.30		v=0.35		v=0.40		v=0.45		v=0.50	
a/h	We	Ming	We	Ming	We	Ming	We	Ming	We	Ming
0.2	1.187399818	1.224	1.20612883	0.255	1.236802532	1.281	1.291019433	1.334	1.40062881	1.42
0.4	1.43631999	1.521	1.469247656	1.572	1.51712911	1.635	1.590363208	1.751	1.713545898	1.932
0.6	1.768745681	1.839	1.810356684	1.929	1.884057682	2.05	2.016650183	2.26	2.266828938	2.606
1	2.364045722	2.618	2.490243982	2.798	2.687017865	3.075	3.017683563	3.522	3.633658335	4.381
1.5	3.315789474	3.699	3.551685741	4.025	3.935007828	4.577	4.623390912	5.632	6.103029996	8.396
2	4.209082985	4.738	4.563868149	5.208	5.168905614	6.04	6.345749873	7.761	9.342198503	13.052

Chapter 7: Appendix

Appendix A.5

Table 5: For Cylindrical and Uniaxial indentation (μ, α) obtained from inverse analysis. For 5% and 15% PVA-C, 2FTC specimen

Method	Material	Radius(B/2)	Depth(L)	Experimental	Inverse	Experimental	Inverse
	PVA (%) 2FTC	(mm)	(mm)	Mu (kPa)	Alpha	Mu (kPa)	Alpha
UCS	5	19	12	0.0025	10.749	0.0026	10.965
Cylindrical	5	19	12	0.00249	10.76	0.0025	11.8
Cylindrical	10	19	12	0.004	4.67	0.004	4.84
UCS	15	19	12	0.01	25	0.011	24.93
Cylindrical	15	19	12	0.011	25	0.016	25.43
Cylindrical	20	19	12	0.0213	25	0.02	25.4

Chapter 7: Appendix

Appendix A.6

Table 1: Friction coefficient (Ω) = 0 and (a/h)=0.2

				Element Mesh=582						
a	h	a/h	w/h(Percent)	w	E	P	v	1-v^2	Formula	k1=P(1-v^2)/2Eaw
4	20	0.2	0.1	0.1 4.02E-04	0.1	0.0006	0.5	0.75	2	1.40029873
4	20	0.2	10	10 4.01E-02	0.1	0.06	0.5	0.75	2	1.401345291
4	20	0.2	15	15 0.0602	0.1	0.09	0.5	0.75	2	1.401578073
4	20	0.2	100	100 0.4012	0.1	0.6	0.5	0.75	2	1.402043868
				Element Mesh = 869						
a	h	a/h	w/h(Percent)	w	E	P	v	1-v^2	Formula	k2=P(1-v^2)/2Eaw
4	20	0.2	0.1	4.02E-04	0.1	0.0006	0.5	0.75	2	1.399950224
4	20	0.2	10	4.02E-02	0.1	0.06	0.5	0.75	2	1.400996264
4	20	0.2	15	6.02E-02	0.1	0.09	0.5	0.75	2	1.401345291
4	20	0.2	100	0.4013	0.1	0.6	0.5	0.75	2	1.401694493
				Element Mesh= 1383						
a	h	a/h	w/h(Percent)	w	E	P	v	1-v^2	Formula	k3=P(1-v^2)/2Eaw
4	20	0.2	0.1	4.02E-04	0.1	0.0006	0.5	0.75	2	1.399950224
4	20	0.2	10	4.01E-02	0.1	0.06	0.5	0.75	2	1.402743142
4	20	0.2	15	6.02E-02	0.1	0.09	0.5	0.75	2	1.40087996
4	20	0.2	100	0.4014	0.1	0.6	0.5	0.75	2	1.401345291
				Element Mesh = 2351						
a	h	a/h	w/h(Percent)	w	E	P	v	1-v^2	Formula	k4=P(1-v^2)/2Eaw
4	20	0.2	0.1	4.02E-04	0.1	0.0006	0.5	0.75	2	1.399253731
4	20	0.2	10	4.02E-02	0.1	0.06	0.5	0.75	2	1.40029873
4	20	0.2	15	6.03E-02	0.1	0.09	0.5	0.75	2	1.400414938
4	20	0.2	100	0.4016	0.1	0.6	0.5	0.75	2	1.40064741
				Element Mesh=3647						
a	h	a/h	w/h(Percent)	w	E	P	v	1-v^2	Formula	k1=P(1-v^2)/2Eaw
4	20	0.2	0.1	4.02E-04	0.1	0.0006	0.5	0.75	2	1.399601891
4	20	0.2	10	4.02E-02	0.1	0.06	0.5	0.75	2	1.40064741
4	20	0.2	15	6.02E-02	0.1	0.09	0.5	0.75	2	1.40087996
4	20	0.2	100	0.4016	0.1	0.6	0.5	0.75	2	1.40064741
				Element Mesh= 5458						
a	h	a/h	w/h(Percent)	w	E	P	v	1-v^2	Formula	k1=P(1-v^2)/2Eaw
4	20	0.2	0.1	0.1 4.02E-04	0.1	0.0006	0.5	0.75	2	1.399253731
4	20	0.2	10	10 4.02E-02	0.1	0.06	0.5	0.75	2	1.40029873
4	20	0.2	15	15 6.03E-02	0.1	0.09	0.5	0.75	2	1.400414938
4	20	0.2	100	100 0.4019	0.1	0.6	0.5	0.75	2	1.399601891
				Element Mesh= 7833						
a	h	a/h	w/h(Percent)	w	E	P	v	1-v^2	Formula	k1=P(1-v^2)/2Eaw
4	20	0.2	0.1	0.1 4.02E-04	0.1	0.0006	0.5	0.75	2	1.399253731
4	20	0.2	10	10 4.02E-02	0.1	0.06	0.5	0.75	2	1.40029873
4	20	0.2	15	15 6.03E-02	0.1	0.09	0.5	0.75	2	1.400414938
4	20	0.2	100	100 0.4018	0.1	0.6	0.5	0.75	2	1.399950224
				Element Mesh= 9542						
a	h	a/ h	w/h(Percent)	w	E	P	v	1-v^2	Formula	k1=P(1-v^2)/2Eaw
4	20	0.2	0.1	4.02E-04	0.1	0.0006	0.5	0.75	2	1.399601891
4	20	0.2	10	4.02E-02	0.1	0.06	0.5	0.75	2	1.40064741
4	20	0.2	15	6.02E-02	0.1	0.09	0.5	0.75	2	1.40087996
4	20	0.2	100	0.4019	0.1	0.6	0.5	0.75	2	1.399601891

Chapter 7: Appendix

Appendix A.6

CYLINDRICAL INDENTATION, INVERSE ANALYSIS
OGDEN HYPERELASTIC MODEL

```
%----------------------------------------------------
function [f] = fssr_2(a,XM,YM)
%YP = 2*(a(1)./a(2)).*(XM.^(a(2)-1))%-XM.^(a(2)/2-1));
%YP = 2*(a(1)/a(2))*(XM.^a(2)-XM.^(-a(2)/2));
% YP=a(1)*XM.^(a(2))+a(3)*XM.^(a(4));
c1=2*a(1)./a(2);
YP=c1*XM.^(a(2)-1)-c1*XM.^(-a(2)./2-1);
%YP=c1*stretch.^(a(2)-1)-c1*stretch.^(-a(2)./2-1);
f=sum((YP-YM).^2)
%f=min(abs(YP-YM))
end
%----------------------------------------------------
clc; clear all; close all;
%using Mojdeh PVA-C 5% Cyl data for Input and simulated F-D data for unknown
%parameter
length0=12;
radius=19;
YM=[
];
XM=[
];
XM=XM./length0; % now XM means strain
stretch=1-XM;%./length0; Means stretch
stress=YM./(pi*radius*radius); %now YM means nominal stress
alpha_m_all=[]; beta_m_all=[]; %for 15 Dec 2018 modification
MAx_iter=500
for ii=1:MAx_iter
%options=optimset('Display','iter','MaxIter',ii)
options=optimset('MaxIter',ii)
[a, FVAL] = fminsearch(@fssr_2,[0.00249 10.766], options, stretch, stress);
```

Chapter 7: Appendix

```
                  Mu(ii) =|a(1).
                  Alpha(ii) = a(2).
                  c1=2*a(1)./a(2);
         YP=c1*stretch.^(a(2)-1)-c1*stretch.^(-a(2)./2-1);
                %-----15 Dec 2018-----------
                  alpha_m=2*a(1)/a(2)
                    beta_m=a(2)
            alpha_m_all=[alpha_m_all;alpha_m];
              beta_m_all=[beta_m_all;beta_m];
                  %-------------------
         % YP=a(1)*XM.^(a(2))+a(3)*XM.^(a(4))
                       end
                lamda_exp=stretch;
              lamda_Predicted=stretch;
                sigma_exp=-stress;
               sigma_Predicted=-YP;
                     figure(1)
               plot(1:ii,Mu/Mu(end));
                  legend('¥mu')
                     figure(2)
             plot(1:ii,Alpha/Alpha(end));
                 legend('¥alpha')

%------------------------------------------------------------
                     figure(3)
        plot(1:ii,Mu/Mu(end),1:ii,Alpha/Alpha(end));
                %legend('¥mu','¥alpha')
    title(['¥fontname{calibri}¥fontsize{12}CONVERGENCE CHECK ']);
xlabel(' Number of iteration (K)'); ylabel('Normalized (¥mu/¥mu_0), (¥alpha/¥alpha_0)');
      legend({'¥mu','¥alpha'},'FontSize',8,'TextColor','black');
               dim = [0.2 0.3 0.4 0.5];
    str = {'PVA-5% 2FTC, uc ¥mu=-0.0026kPa , ¥alpha=10.9654'};
     annotation('textbox',dim,'String',str,'FitBoxToText','on');
```

Chapter 7: Appendix

```
set(gca,'fontsize', 8);
%-------------------------------------------------------------------
figure(4)
plot (XM,-sigma_exp,'--',XM, -sigma_Predicted,'o','Markersize',3);
xlabel('Strain (¥epsilon)'); ylabel('Stress ¥sigma(N/mm^2)')

title(['¥fontname{calibri}¥fontsize{12}STRESS VS STRAIN ']);

%xlabel(' Stretch ¥lambda'); ylabel('Stress  ¥sigma(nN/mm^2)');
legend({'Experimental','Predicted'},'FontSize',8,'TextColor','black');
set(gca,'fontsize', 10);
dim = [0.2 0.3 0.4 0.5];
str = {'PVA-5% 2FTC, uc ¥mu=-0.0026kPa , ¥alpha=10.9654'};

annotation('textbox',dim,'String',str,'FitBoxToText','on');
set(gca,'fontsize', 10);
%-----------------------------------------------------
figure(5);
plot (lamda_exp,sigma_exp,'--',lamda_Predicted,sigma_Predicted,'o','MarkerSize',3);
RESIDUAL=sigma_exp-sigma_Predicted;
%xlim([0 1]);
%xlabel('¥lambda'); ylabel('¥sigma(MPa)');
set(gca,'fontsize', 12);
title(['¥fontname{calibri}¥fontsize{12}STRESS VS STRETCH ']);

xlabel(' Stretch ¥lambda'); ylabel('Stress ¥sigma(N/mm^2)');

legend({'Experimental','Predicted'},'FontSize',8,'TextColor','black')

; dim = [0.2 0.3 0.4 0.5];

str = {'PVA-5% 2FTC, uc ¥mu=-0.0026kPa , ¥alpha=10.9654'};

annotation('textbox',dim,'String',str,'FitBoxToText','on');
set(gca,'fontsize', 10);
%-----------------------------------------------------------
figure(6);
plot (lamda_exp, RESIDUAL,'o','MarkerSize',3
```

Chapter 7: Appendix

Appendix A.8

MOONEY RILVIN HYPERELASTIC MODEL
CYLINDRICAL INDENTATION
INVERSE ANALYSIS

```
%--------------------------------------------------
function [f] = fssr_MR(a,XM,YM)
%YP = 2*(a(1)./a(2)).*(XM.^(a(2)-1))%-XM.^(a(2)/2-1);
%YP = 2*(a(1)/a(2))*(XM.^a(2)-XM.^(-a(2)/2));
%YP=a(1)*XM.^(a(2))-a(1)*XM.^(a(3));
%c1=2*a(1)./a(2);
A=1-1./(XM.*XM.*XM)
YP=2*a(1).*A + 2*a(2).*A./XM;
f=sum((YP-YM).^2);
%f=min(abs(YP-YM))
end
%--------------------------------------------------
clc; clear all; close all;
%length0=12;
%radius=4;
YM=[
];
XM=1+XM%/length0; % now XM means strain
YM=YM%/(pi*radius*radius); %now YM means nominal stress
%
MAx_iter=500
for ii=1:MAx_iter
%options=optimset('Display','iter','MaxIter',ii)
options=optimset('MaxIter',ii)
%options=optimset('Display','iter')
a = fminsearch(@fssr_MR, [1 1], options, XM, YM);
C10(ii) = a(1);
C01(ii) = a(2);
A=1-1./(XM.*XM.*XM);
```

Chapter 7: Appendix

```
YP=2*a(1)*A+2*a(2)*A./XM;
%YP=a(1)*XM.^(a(2))+a(3)*XM.^(a(4));
%YP=2*a(1)*A+2*a(2)*A./XM+2*a(3)*A./XM
                end
              figure(1)
          plot(1:ii,C10/C10(end));
              legend('C10')
              figure(2)
          plot(1:ii,C01/C01(end));
              legend('C01')
              figure(3)
   plot(1:ii,C10/C10(end),1:ii,C01/C01(end));
            legend('C10','C01')
              figure(4)
      plot (XM,YM,'o',XM,YP,'-');
      xlabel('Strain'); ylabel('Stress')
              figure(5);
            lamda_exp=XM;
            radius=4; %mm
            sigma_exp=-YM;
          lamda_Predicted=XM;
            radius=4; %mm
          sigma_Predicted=-YP;
 plot (lamda_exp,sigma_exp,'o',lamda_Predicted,sigma_Predicted,'--');
        xlabel('¥lambda'); ylabel('¥sigma(MPa)')
            set(gca,'fontsize', 15);
```

Bibliography

[1] V. Alastrué, J. F. Rodríguez, B. Calvo, and M. Doblaré. Structural damage models for fibrous biological soft tissues. *International Journal of Solids and Structures*, 44(18- 19):5894–5911, 2007.

[2] Jung Kim, Bummo Ahn, Suvranu De, and Mandayam A. Srinivasan. An efficient soft tissue characterization algorithm from in vivo indentation experiments for medical simulation. *International Journal of Medical Robotics and Computer Assisted Surgery*, 4(3):277–285, 2008.

[3] Guidelines for safe work practices in human and animal medical diagnostic laboratories. Recommendations of a CDC-convened, Biosafety Blue-Ribbon Panel. *Center for Dis- ease Control and Prevention: Morbidity and Mortality Weekly Report*, 61 Supplem:13– 33, 2012.

[4] Y. Zheng, Y. J. Wang, X. Chen, L. Qing, and H. Yang. Preparation and Characterization of Poly(vinyl alcohol)/Hydroxylapatite Hybrid Hydrogels. *Journal of Composite Materials*, 41(17):2071–2082, 2007.

[5] A Matthews, C Hutnik, K Hill, T Newson, T Chan, and G Campbell. Indentation and needle insertion properties of the human eye. *Eye*, 28(7):880–887, 2014.

[6] C M Hassan, J H Ward, and N a Peppas. Modeling of crystal dissolution of poly (vinyl alcohol) gels produced by freezing / thawing processes. 41:6729–6739, 2000.

[7] Nilza G Ramião, Pedro S Martins, Rita Rynkevic, António A Fernandes, Maria Barroso, and Diana C Santos. Biomechanical properties of breast tissue, a state-of-the-art review. *Biomechanics and Modeling in Mechanobiology*, 15(5):1307–1323, 2016.

[8] T. Wierzbicki and P. Thomas. Closed-form solution for wedge cutting force through thin metal

Bibliography

sheets. *International Journal of Mechanical Sciences*, 35(3-4):209–229, 1993.

[9] John D. Finan, Patrick M. Fox, and Barclay Morrison. Non-ideal effects in Indentation testing of soft tissues. *Biomechanics and Modeling in Mechanobiology*, 13(3):573–584, 2014.

[10] Martijn A J Cox, Niels J B Driessen, Ralf A. Boerboom, Carlijn V C Bouten, and Frank P T Baaijens. Mechanical characterization of anisotropic planar biological soft tissues using finite indentation: Experimental feasibility. *Journal of Biomechanics*, 41(2):422– 429, 2008.

[11] C. Gamonpilas, M. N. Charalambides, J. G. Williams, P. J. Dooling, and S. R. Gibbon. Predicting the mechanical behavior of starch gels through inverse analysis of indentation data. *Applied Rheology*, 20(3):1–9, 2010.

[12] Fuqian Yang. Thickness effect on the indentation of an elastic layer. *Materials Science and Engineering A*, 358(1-2):226–232, 2003.

[13] Hongjun Jiang, Gord Campbell, Derek Boughner, Wan-Kei Wan, and Mackenzie Quantz. Design and manufacture of a polyvinyl alcohol (PVA) cryogel tri-leaflet heart valve prosthesis. *Medical Engineering & Physics*, 26(4):269–277, May 2004.

[14] Ali Sadeghi Naini, Rajni V. Patel, and Abbas Samani. Measurement of lung hyperelastic properties using inverse finite element approach. *IEEE Transactions on Biomedical Engineering*, 58(10 PART 1):2852–2859, 2011.

[15] Abbas Samani and Donald Plewes. A method to measure the hyperelastic parameters of ex vivo breast tissue samples. *Physics in medicine and biology*, 49(18):4395–4405, 2004.

[16] Kiattisak Sangpradit, Hongbin Liu, Lakmal D. Seneviratne, and Kaspar Althoefer. Tis- sue identification using inverse finite element analysis of rolling indentation. *Proceedings- IEEE International Conference on Robotics and Automation*, pages 1250–1255, 2009.

[17] John Z. Wu, Ren G. Dong, and Aaron W. Schopper. Analysis of effects of friction on the deformation behavior of soft tissues in unconfined compression tests. *Journal of Biomechanics*, 37(1):147–155, 2004.

Bibliography

[18] Anthony Atala. Tissue engineering of human bladder. *British Medical Bulletin*, 97(1):81– 104, 2011.

[19] William C. Carson, Gregory J. Gerling, Tracey L. Krupski, Casey G. Kowalik, Jeffrey C. Harper, and Christopher A. Moskaluk. Material characterization of ex vivo prostate tis- sue via spherical indentation in the clinic. *Medical Engineering and Physics*, 33(3):302– 309, 2011.

[20] Won C. Bae, Chad W. Lewis, Marc E. Levenston, and Robert L. Sah. Indentation testing of human articular cartilage: Effects of probe tip geometry and indentation depth on intra-tissue strain. *Journal of Biomechanics*, 39(6):1039–1047, 2006.

[21] Clayton T McKee, Julie a Last, Paul Russell, and Christopher J Murphy. Indentation versus tensile measurements of Young's modulus for soft biological tissues. *Tissue engineering. Part B, Reviews*, 17(3):155–164, 2011.

[22] Anne L. Coleman and Stefano Miglior. Risk Factors for Glaucoma Onset and Progression. *Survey of Ophthalmology*, 53(6 SUPPL.), 2008.

[23] Maren Freutel, Hendrik Schmidt, Lutz Dürselen, Anita Ignatius, and Fabio Galbusera. Finite element modeling of soft tissues: Material models, tissue interaction and challenges, 2014.

[24] G A Holzapfel. Biomechanics of soft tissue. *Handbook of Material Behavior*, (7):1–15, 2000.

[25] Ming Zhang, Y.P. Zheng, and Arthur F.T. Mak. Estimating the effective Young's mod- ulus of soft tissues from indentation tests—nonlinear finite element analysis of effects of friction and large deformation. *Medical Engineering & Physics*, 19(6):512–517, Sep 1997.

[26] L. Sanchez Fellay, L. A. Fasce, M. Czerner, E. Pardo, and P. M. Frontini. On the Feasibility of Identifying First Order Ogden Constitutive Parameters of Gelatin Gels from Flat Punch Indentation Tests. *Soft Materials*, 13(4):188–200, 2015.

[27] M.J. Boussinesq. Paris: Gauthier-Villard imprimeur libraire. 1885.

Bibliography

[28] Ian N. Sneddon. The relation between load and penetration in the axisymmetric Boussinesq problem for a punch of arbitrary profile. *International Journal of Engineering Science*, 3(1):47–57, 1965.

[29] W. C. Hayes, L. M. Keer, G. Herrmann, and L. F. Mockros. A mathematical analysis for indentation tests of articular cartilage. *Journal of Biomechanics*, 5(5):541–551, 1972.

[30] Yanping Cao, Duancheng Ma, and Dierk Raabe. The use of flat punch indentation to determine the viscoelastic properties in the time and frequency domains of a soft layer bonded to a rigid substrate. *Acta Biomaterialia*, 5(1):240–248, 2009.

[31] K L Johnson. *Contact Mechanics*, volume 37. 1985.

[32] M. J. Jaffar. *Journal of the Mechanics and Physics of Solids*, (4).

[33] W. T. Koiter. On the principle of stationary complementary energy in the nonlinear theory of elasticity. *SIAM Journal on Applied Mathematics*, 25(3):424–434, 1973.

[34] Campbell. G Mathew. A. Tissue-mimicking Construct of the Human Eye PART II Suitability of Tissue-mimicking Construct as a Human Eye Model. (September), 2011.

[35] Olek C. Zienkiewicz, R. L. Taylor, and P. Nithiarasu. The finite element method for fluid dynamics, 2014.

[36] Hongjian Shi. Finite element modeling of soft tissue deformation . (December), 2007.

[37] R. G. Ahlvin and H. H. Ulery. Tabulated Values for Determining the Complete Pattern of Stresses, Strains, and Deflections Beneath a Uniform Circular Load on a Homogeneous Half Space. *Highway Research Board Bulletin*, (342):1–13, 1962.

[38] Mojdeh Zakeri. Assessment of the Non-linear Stress-strain Characteristics of Poly (vinyl alcohol) Cryogel.

[39] Y. C. Fung and S. C. Cowin. Biomechanics: Mechanical Properties of Living Tissues, 2nd ed., 1994.

Bibliography

[40] B Riccardi and R Montanari. Indentation of metals by a flat-ended cylindrical punch. *Materials Science and Engineering: A*, 381(1-2):281–291, Sep 2004.

[41] I. I. Argatov, G. S. Mishuris, and M. V. Paukshto. Cylindrical lateral depth-sensing indentation testing of thin anisotropic elastic films. *European Journal of Mechanics, A/Solids*, 49:299–307, 2015.

[42] Lior Kogut and Kyriakos Komvopoulos. Analysis of the spherical indentation cycle for elastic–perfectly plastic solids. *Journal of Materials Research*, 19(12):3641–3653, 2004.

[43] Gladwell G. M. L. *Contact problems in the classical theory of elasticity*. 1980.

[44] Guanghui Fu. An Extension of Hertz's Theory in Contact Mechanics. *Journal of Applied Mechanics*, 74(2):373–374, 01 2006.

[45] *Journal of Reine Angew. Math.*, 92:156–171, 1882.

[46] M. T. Huber. Zur theorie der berührung fester elastischer körper. *Annalen der Physik*, 319(6):153–163, 1904.

[47] *Elastic Indentation Stress Fields*, pages 77–100. Springer US, Boston, MA, 2007.

[48] A. E H Love. Boussinesq's problem for a rigid cone. *Quarterly Journal of Mathematics*, os-10(1):161–175, 1939.

[49] Ian N. Sneddon. Boussinesq's problem for a flat-ended cylinder. *Mathematical Proceedings of the Cambridge Philosophical Society*, 42(1):29–39, 1946.

[50] Makoto Sakamoto, Guoan Li, Toshiaki Hara, and Edmund Y S Chao. A new method for theoretical analysis of static indentation test. *Journal of Biomechanics*, 29(5):679–685, 1996.

[51] M Wo, A Hummel, and V J Pauk. Axisymmetric contact problems for an elastic layer resting

Bibliography

on a rigid base with a Winkler type excavation. 39:4117–4131, 2002.

[52] P. K. Chaudhuri and Subhankar Ray. Effects of an axisymmetric rigid punch on a nonhomogeneous transversely isotropic half-space. *The ANZIAM Journal*, 44(03):461, 2003.

[53] K. L. Johnson. The correlation of indentation experiments. *Journal of the Mechanics and Physics of Solids*, 18(2):115–126, 1970.

[54] A.H. Burstein. Elastic analysis of condylar structures,1968.

[55] S. D. Mesarovic and N. a. Fleck. Spherical indentation of elastic-plastic solids. *Proceedings of the Royal Society A: Mathematical, Physical and Engineering Sciences*, 455(January 1998):2707–2728, 1999.

[56] Y Charles Lu, Siva N V R K Koraput, and Fuqian Yang. Finite element analysis of cylindrical indentation for determining plastic properties of materials in small volumes. *Journal of Physics D: Applied Physics*, 41(11):115415, 2008.

[57] J. J. Kang, A. A. Becker, and W. Sun. Determining elastic-plastic properties from indentation data obtained from finite element simulations and experimental results. *International Journal of Mechanical Sciences*, 62(1):34–46, 2012.

[58] A S T Badrick and K E Puttick. Surface tensile stresses around indentations in NaCl. *Journal of Physics D: Applied Physics*, 19(1):51–56, Jan 1986.

[59] F. J. Carter, T. G. Frank, P. J. Davies, D. McLean, and A. Cuschieri. Measurements and modelling of the compliance of human and porcine organs. *Medical Image Analysis*, 5(4):231–236, 2001.

[60] R. M. Delaine-Smith, S. Burney, F. R. Balkwill, and M. M. Knight. Experimental validation of a flat punch indentation methodology calibrated against unconfined compression tests for determination of soft tissue biomechanics. *Journal of the Mechanical Behavior of Biomedical Materials*, 60:401–415, 2016.

Bibliography

[61] Andrew R. Karduna, Henry R. Halperin, and Frank C P Yin. Experimental and numerical analyses of indentation in finite-sized isotropic and anisotropic rubber-like materials. *Annals of Biomedical Engineering*, 25(6):1009–1016, 1997.

[62] Christopher W. Macminn, Eric R. Dufresne, and John S. Wettlaufer. Large Deformations of a Soft Porous Material. *Physical Review Applied*, 5(4):1–28, 2016.

[63] Amy E. Kerdok, Mark P. Ottensmeyer, and Robert D. Howe. Effects of perfusion on the viscoelastic characteristics of liver. *Journal of Biomechanics*, 39(12):2221–2231, 2006.

[64] Sergio Casciaro, Francesco Conversano, Stefano Musio, Ernesto Casciaro, Christian Demitri, and Alessandro Sannino. Full experimental modelling of a liver tissue mimicking phantom for medical ultrasound studies employing different hydrogels. *Journal of Materials Science: Materials in Medicine*, 20(4):983–989, 2009.

[65] Shan Jiang, Sha Liu, and Wenhao Feng. PVA hydrogel properties for biomedical application. *Journal of the Mechanical Behavior of Biomedical Materials*, 4(7):1228–1233, 2011.

[66] Brian G Bush, Jenna M Shapiro, Frank W DelRio, Robert F Cook, and Michelle L Oyen. Mechanical measurements of heterogeneity and length scale effects in PEG-based hydrogels. *Soft Matter*, 11(36):7191–7200, 2015.

[67] S.P. Marra, K.T. Ramesh, and A.S. Douglas. Mechanical characterization of active poly(vinyl alcohol)–poly(acrylic acid) gel. *Materials Science and Engineering: C*, 14(1-2):25–34, 2001.

[68] Colin Grant, Pete Twigg, Alex Egan, Alexandra Moody, Annie Smith, Donald Eagland, Nicholas Crowther, and Steve Britland. Poly(vinyl alcohol) hydrogel as a biocompatible viscoelastic mimetic for articular cartilage. *Biotechnology Progress*, 22(5):1400–1406, 2006.

[69] Hydrogels for biomedical applications. *Advanced Drug Delivery Reviews*, 64(SUPPL.):18–23, 2012.

Bibliography

[70] Gaio Paradossi, Francesca Cavalieri, Ester Chiessi, Chiara Spagnoli, and Mary K. Cowman. Poly(vinyl alcohol) as versatile biomaterial for potential biomedical applications. *Journal of Materials Science: Materials in Medicine*, 14(8):687–691, 2003.

[71] Ahmed Elsheikh, Defu Wang, Michael Brown, Paolo Rama, Marino Campanelli, and David Pye. Assessment of corneal biomechanical properties and their variation with age. *Current eye research*, 32(1):11–19, 2007.

[72] Campbel. G. Tissue-mimicking Construct of the Human Eye. 2012.

[73] W. Huang. Convergence analysis of finite element solution of one-dimensional singularly perturbed differential equations on equidistributing meshes. *International Journal of Numerical Analysis and Modeling*, 2(1):57–74, 2005.

[74] Jason A. Stammen, Stephen Williams, David N. Ku, and Robert E. Guldberg. Mechanical properties of a novel PVA hydrogel in shear and unconfined compression. *Biomaterials*, 22(8):799–806, 2001.

[75] Abhijeet Joshi, Garland Fusel, Jonathan Thomas, Andrew Hsian, Anthony Lowman, Andrew Karduna, Ed Vresilovic, and Michele Marcolongo. Functional compressive mechanics of a PVA/PVP nucleus pulposus replacement. *Biomaterials*, 27(2):176–184, 2006.

[76] Bill Hao Wang and Gord Campbell. Formulations of polyvinyl alcohol cryogel that mimic the biomechanical properties of soft tissues in the natural lumbar intervertebral disc. *Spine*, 34(25):2745–2753, 2009.

[77] M A Adams, D W McMillan, T P Green, and P Dolan. Sustained loading generates stress concentrations in lumbar intervertebral discs., 1996.

[78] Helena N. Chia and M. L. Hull. Compressive moduli of the human medial meniscus in the axial and radial directions at equilibrium and at a physiological strain rate. *Journal of Orthopaedic Research*, 26(7):951–956, 2008.

Bibliography

[79] Mihori Kita, Yuichiro Ogura, Yoshihito Honda, and Suong-Hyu Hyon. Evaluation of polyvinyl alcohol hydrogel as a soft contact lens material. *Graefes Arch Clin Exp Ophtalmol*, 228:533–537, 1990.

[80] Pan Li, Shan Jiang, Yan Yu, Jun Yang, and Zhiyong Yang. Biomaterial characteristics and application of silicone rubber and PVA hydrogels mimicked in organ groups for prostate brachytherapy. *Journal of the Mechanical Behavior of Biomedical Materials*, 49:220–234, sept 2015.

[81] Meirigeng Qi, Yuanjun Gu, Naoaki Sakata, Dohoon Kim, Yasumasa Shirouzu, Chizuru Yamamoto, Akihito Hiura, Shoichiro Sumi, and Kazutomo Inoue. PVA hydrogel sheet macro encapsulation for the bioartificial pancreas. *Biomaterials*, 25(27):5885–5892, 2004.

[82] Jeffrey D. Brown, Jacob Rosen, Yoon Sang Kim, Lily Chang, Mika N. Sinanan, and Blake Hannaford. In-vivo and in-situ compressive properties of porcine abdominal soft tissues. In *Studies in Health Technology and Informatics*, volume 94, pages 26–32, 2003.

[83] On a nonlinear inverse problem in viscoelasticity. *Vietnam Journal of Mechanics*, 31(3):211–219, 2009.

[84] Theo Z Pavan, Ernest L Madsen, Gary R Frank, Antonio Adilton O Carneiro, and Timothy J Hall. Nonlinear elastic behavior of phantom materials for elastography. *Physics in medicine and biology*, 55(9):2679–92, 2010.

[85] R. W. Ogden. Volume changes associated with the deformation of rubber-like solids. *Journal of the Mechanics and Physics of Solids*, 24(6):323–338, 1976.

[86] B. Fereidoonnezhad, R. Naghdabadi, and J. Arghavani. A hyperelastic constitutive model for fiber-reinforced rubber-like materials. *International Journal of Engineering Science*, 71:36–44, 2013.

[87] Yu Yun Lin and Bao Wun Hu. Load relaxation of a flat rigid circular indenter on a gel half space. *Journal of Non-Crystalline Solids*, 352(38-39):4034–4040, 2006.

Bibliography

[88] W H Li and X. Z. Zhang. The effect of friction on magnetorheological fluids. *Korea-Australia Rheology Journal*, 20(2):45–50, 2008.

[89] Aidy Ali, Mohammad Hosseini Fouladi, and Barkawi Sahari. A Review of Constitutive Models for Rubber-Like Materials. *American Journal of Engineering and Applied Sciences*, 3(1):232–239, 2010.

[90] Elizabeth Mesamúnera, Juan F Ramírez-salazar, Pierre Boulanger, and John W Branch. No Title. 2012.

[91] Vara Isvilanonda, Joseph M. Iaquinto, Shruti Pai, Peter Mackenzie-Helnwein, and William R. Ledoux. Hyperelastic compressive mechanical properties of the subcalcaneal soft tissue: An inverse finite element analysis. *Journal of Biomechanics*, 49(7):1186– 1191, 2016.

[92] A. P C Choi and Yong Ping Zheng. Estimation of Young's modulus and Poisson's ratio of soft tissue from indentation using two different-sized indenters: Finite element analysis of the finite deformation effect. *Medical and Biological Engineering and Computing*, 43(2):258–264, 2005.

[93] T Al-ja'afreh, Y Zweiri, L Seneviratne, and K Althoefer. A new soft-tissue indentation model for estimating circular indenter 'force-displacement' characteristics. *Proceedings of the Institution of Mechanical Engineers. Part H, Journal of engineering in medicine*, 222(5):805–815, 2008.

[94] Bummo Ahn and Jung Kim. Measurement and characterization of soft tissue behavior with surface deformation and force response under large deformations. *Medical Image Analysis*, 14(2):138–148, 2010.

[95] R Namani and N Simha. Inverse finite element analysis of indentation tests to deter- mine hyperelastic parameters of soft-tissue layers. *The Journal of Strain Analysis for Engineering Design*, 44(5):347–362, 2009.

[96] W.C. Oliver and G.M. Pharr. Measurement of hardness and elastic modulus by instrumented

Bibliography

indentation: Advances in understanding and refinements to methodology. *Journal of Materials Research*, 19(01):3–20, 2004.

[97] L. Cheng, X. Xia, W. Yu, L. E. Scriven, and W. W. Gerberich. Flat-punch indentation of viscoelastic material. *Journal of Polymer Science, Part B: Polymer Physics*, 38(1):10– 22, 2000.

[98] M. J. Jaffar. Frictionless contact between an elastic layer on a rigid base and a circular flat-ended punch with rounded edge or a conical punch with rounded tip. *International Journal of Mechanical Sciences*, 44(3):545–560, 2002.

[99] J. Marteau, S. Bouvier, and M. Bigerelle. Review on Numerical Modeling of Instrumented Indentation Tests for Elastoplastic Material Behavior Identification. *Archives of Computational Methods in Engineering*, 22(4):577–593, 2014.

[100] C. Gamonpilas and E.P. Busso. Characterization of elastoplastic properties based on inverse analysis and finite element modeling of two separate indenters. *Journal of Engineering Materials and Technology, Transactions of the ASME*, 129(4):603–608, 2007.

[101] Adonias Ribeiro Franco Jr., Giuseppe Pintaúde, Amilton Sinatora, Carlos Eduardo Pinedo, and André Paulo Tschiptschin. The use of a vickers indenter in depth sensing indentation for measuring elastic modulus and vickers hardness. *Materials Research*, 7(3):483–491, 2004.

[102] A. K. Bhattacharya and W. D. Nix. Analysis of elastic and plastic deformation associated with indentation testing of thin films on substrates. *International Journal of Solids and Structures*, 24(12):1287–1298, 1988.

[103] S M Walley. Historical origins of indentation hardness testing. 28(9), 2012.

[104] Seung-Kyun Kang, Ju-Young Kim, Chan-Pyoung Park, Hyun-Uk Kim, and Dongil Kwon. Conventional Vickers and true instrumented indentation hardness determined by instrumented indentation tests. *Journal of Materials Research*, 25(02):337–343, 2010.

Bibliography

[105] W. Rostoker and J. O. Galante. Indentation creep of polymers for human joint applications, 1979.

[106] P. K. Zysset. Indentation of bone tissue: A short review. *Osteoporosis International*, 20(6):1049–1055, 2009.

[107] Fuqian Yang. Axisymmetric indentation of an incompressible elastic thin film. *Mechanics of Materials*, 30:275–286, 1998.

[108] D. A. Spence. The hertz contact problem with finite friction. *Journal of Elasticity*, 5(3-4):297–319, 1975.

[109] David Louapre and Kristin Breder. Hertzian Indentation Stress Field Equations. *International Journal of Applied Ceramic Technology*, 12(5):1071–1079, 2015.

[110] A. E. H. Love. The Stress Produced in a Semi-Infinite Solid by Pressure on Part of the Boundary. *Philosophical Transactions of the Royal Society A: Mathematical, Physical and Engineering Sciences*, 228(659-669):377–420, 1929.

[111] V. M. Aleksandrov. Axisymmetric contact problems for a prestressed incompressible elastic layer. *Journal of Applied Mathematics and Mechanics*, 76(1):120–124, 2012.

[112] Christopher A. Schuh. Nanoindentation studies of materials. *Materials Today*, 9(5):32–40, 2006.

[113] Pierre Emmanuel Mazeran, Moez Beyaoui, Maxence Bigerelle, and Michèle Guigon. Determination of mechanical properties by nanoindentation in the case of viscous materials. *International Journal of Materials Research*, 103(6):715–722, 2012.

[114] G Odegard, T S Gates, and H B T Experimental Mechanics Herring. Characterization of viscoelastic properties of polymeric materials through nanoindentation. *Experimental Mechanics*, 45(2):130–136, 2005.

Bibliography

[115] J. D. Humphrey. Review Paper: Continuum biomechanics of soft biological tissues. *Proceedings of the Royal Society A: Mathematical, Physical and Engineering Sciences*, 459(2029):3–46, 2003.

[116] D.X. Liu, Z.D. Zhang, and L.Z. Sun. Nonlinear elastic load–displacement relation for spherical indentation on rubberlike materials. *Journal of Materials Research*, 25(11):2197–2202, 2010.

[117] Man Gong Zhang, Yan Ping Cao, Guo Yang Li, and Xi Qiao Feng. Spherical indentation method for determining the constitutive parameters of hyperelastic soft materials. *Biomechanics and Modeling in Mechanobiology*, 13(1):1–11, 2014.

[118] Elizabeth Mesa Múnera. Characterization of brain tissue phantom using an indentation device and inverse finite element parameter estimation algorithm. page 99, 2011.

[119] R S Rivlin and D W Saunders. Large Elastic Deformations of Isotropic Materials. VII. Experiments on the Deformation of Rubber. *Philosophical Transactions of the Royal Society of London. Series A, Mathematical and Physical Sciences*, 243(865):251 LP – 288, Apr 1951.

[120] R. W. Ogden, G. Saccomandi, and I. Sgura. Fitting hyperelastic models to experimental data. *Computational Mechanics*, 34(6):484–502, 2004.

[121] J. Yan, A. M. Karlsson, and X. Chen. Determining plastic properties of a material with residual stress by using conical indentation. *International Journal of Solids and Structures*, 44(11-12):3720–3737, 2007.

[122] L M Farrissey and P E McHugh. Determination of elastic and plastic material properties using indentation: Development of method and application to a thin surface coating. *Materials Science and Engineering a-Structural Materials Properties Microstructure and Processing*, 399(1-2):254–266, 2005.

Bibliography

[123] B Taljat, T Zacharia, and F Kosel. New analytical procedure to determine stress-strain curve from spherical indentation data. *International Journal of Solids and Structures*, 35(33):4411–4426, 1998.

[124] Evren Samur, Mert Sedef, Cagatay Basdogan, Levent Avtan, and Oktay Duzgun. A robotic indenter for minimally invasive measurement and characterization of soft tissue response. *Medical Image Analysis*, 11(4):361–373, 2007.

[125] N Famaey and J V Sloten. Soft tissue modelling for applications in virtual surgery and surgical robotics. *Computer Methods in Biomechanics and Biomedical Engineering*, 11(4):351–366, 2008.

[126] M A Myers, P Chen, Y L Albert, and Y Seki. Biological materials: Structure and mechanical properties. *Progress in Materials Science*, 53:1–206, 2008.

[127] H Mohammadi, D Boughner, L E Millon, and W K Wan. Design and simulation of a poly(vinyl alcohol)-bacterial cellulose nanocomposite mechanical aortic heart valve prosthesis. *Proceedings of the Institution of Mechanical Engineers. Part H, Journal of engineering in medicine*, 223(6):697–711, 2009.

[128] Martin Kauer and Diss E T H No. Inverse Finite Element Characterization of Soft Tissues with Aspiration Experiments Inverse Finite Element Characterization of Soft Tissues with Aspiration. *Medical Image Analysis*, (14233):4–15, 2001.

[129] S P DiMaio and S E Salcudean. Needle insertion modeling and simulation. *Ieee Transactions on Robotics and Automation*, 19(5):864–875, 2003.

[130] Sangita P Patel and Arthur J Sit. A practice model for trabecular meshwork surgery. *Archives of ophthalmology*, 127(3):311–313, 2009.

[131] F Lim and a. Sun. Microencapsulated islets as bioartificial endocrine pancreas. *Science*, 210(4472):908–910, 1980.

[132] T Tanabe and M Nambu. Medical material of polyvinyl alcohol and process of making,

Bibliography

1988.

[133] Shauna R. Stauffer and Nikolaos A. Peppast. Poly(vinyl alcohol) hydrogels prepared by freezing-thawing cyclic processing. *Polymer*, 33(18):3932–3936, 1992.

[134] Alexandre Delalleau, Gwendal Josse, Jean Michel Lagarde, Hassan Zahouani, and Jean Michel Bergheau. Characterization of the mechanical properties of skin by inverse analysis combined with the indentation test. *Journal of Biomechanics*, 39(9):1603–1610, 2006.

[135] Mark R. DiSilvestro and Jun Kyo Francis Suh. A cross-validation of the biphasic poro-viscoelastic model of articular cartilage in unconfined compression, indentation, and confined compression. *Journal of Biomechanics*, 34(4):519–525, 2001.

[136] A Samani, J Bishop, C Luginbuhl, and D B Plewes. Measuring the elastic modulus of ex vivo small tissue samples. *Physics in Medicine and Biology*, 48(14):2183–2198, 2003.

[137] N.N. Lebedev and Ia.S. Ufliand. Axisymmetric contact problem for an elastic layer. *Journal of Applied Mathematics and Mechanics*, 22(3):442–450, Jan 1958.

[138] Y.B. Fu, C.K. Chui, C.L. Teo, and E. Kobayashi. Elasticity imaging of biological soft tissue using a combined finite element and non-linear optimization method. *Inverse Problems in Science and Engineering*, 23(2):179–196, 2015.

[139] Y Mei, B Stover, N Afsar Kazerooni, A Srinivasa, M Hajhashemkhani, MR Hematiyan, and S Goenezen. A comparative study of two constitutive models within an inverse approach to determine the spatial stiffness distribution in soft materials. *International journal of mechanical sciences*, 140:446–454, 2018.

[140] Shruti Pai and William R. Ledoux. The shear mechanical properties of diabetic and non-diabetic plantar soft tissue. *Journal of Biomechanics*, 45(2):364–370, 2012.

[141] I Levental, K R Levental, E A Klein, R Assoian, R T Miller, R G Wells, and P A Janmey. A simple indentation device for measuring micrometer-scale tissue stiffness. *Journal of Physics: Condensed Matter*, 22(19):194120, 2010.

Bibliography

[142] N K Simha, H Jin, M L Hall, S Chiravarambath, and J L Lewis. Effect of indenter size on elastic modulus of cartilage measured by indentation. *J Biomech Eng*, 129(5):767–775, 2007.

[143] Parris S Wellman, Robert D Howe, Edward Dalton, and Kenneth a Kern. Breast Tissue Stiffness in Compression is Correlated to Histological Diagnosis. *Technical Report. Harvard BioRobotics Laboratory*, pages 1–15, 1999.

[144] Kevin Anderson, Ahmed El-Sheikh, and Timothy Newson. Application of structural analysis to the mechanical behavior of the cornea. *Journal of The Royal Society Inter- face*, 1(1):3–15, nov 2004.

[145] M. Danielsson, D. M. Parks, and M. C. Boyce. Constitutive modeling of porous hyper-elastic materials. *Mechanics of Materials*, 36(4):347–358, 2004.

[146] Aidy Ali, Mohammad Hosseini Fouladi, and Barkawi Sahari. A Review of Constitutive Models for Rubber-Like Materials. *American Journal of Engineering and Applied Sciences*, 3(1):232–239, 2010.

[147] AFM indentation study of breast cancer cells. 374(4):609–613, 2008.

[148] J. E. Bischoff, E. a. Arruda, and K. Grosh. A Microstructurally Based Orthotropic Hyperelastic Constitutive Law. *Journal of Applied Mechanics*, 69(5):570, 2002.

[149] R W Ogden. Volume changes associated with the deformation of rubber-like solids. *Journal of the Mechanics and Physics of Solids*, 24(6):323–338, 1976.

[150] R. W. Ogden. Nearly isochoric elastic deformations: Application to rubberlike solids. *Journal of the Mechanics and Physics of Solids*, 26(1):37–57, 1978.

[151] H. Khajehsaeid, J. Arghavani, and R. Naghdabadi. A hyperelastic constitutive model for rubber-like materials. *European Journal of Mechanics, A/Solids*, 38:144–151, 2013.

Bibliography

[152] Beomkeun Kim, Seong Beom Lee, Jayone Lee, Sehyun Cho, Hyungmin Park, Sanghoon Yeom, and Sung Han Park. A comparison among Neo-Hookean model, Mooney-Rivlin model, and Ogden model for Chloroprene rubber. *International Journal of Precision Engineering and Manufacturing*, 13(5):759–764, 2012.

[153] M. Böl and S. Reese. Finite element modelling of rubber-like polymers based on chain statistics, 2006.

[154] Majid Shahzad, Ali Kamran, Muhammad Zeeshan Siddiqui, and Muhammad Farhan. Mechanical Characterization and FE Modelling of a Hyperelastic Material. *Materials Research*, 18:918 – 924, 10 2015.

[155] M.R. Mansouri and H. Darijani. Constitutive modeling of isotropic hyperelastic materials in an exponential framework using a self-contained approach. *International Journal of Solids and Structures*, 51(25):4316 – 4326, 2014.

[156] Martin Kroon and Gerhard A. Holzapfel. Elastic properties of anisotropic vascular membranes examined by inverse analysis. *Computer Methods in Applied Mechanics and Engineering*, 198(45-46):3622–3632, 2009.

[157] Ziheng Yao, Bruce Kang, Chair J Ever Barbero, Co-Chair Xingbo Liu, Julio F Davalos, and Robert C Creese. Development of an Indentation Method for Material Surface Mechanical Properties Measurement. 2005.

[158] W. Huang. Convergence analysis of finite element solution of one-dimensional singularly perturbed differential equations on equidistributing meshes. *International Journal of Numerical Analysis and Modeling*, 2(1):57–74, 2005.

[159] Yutiwadee Pinyochotiwong, Jaroon Rungamornrat, and Teerapong Senjuntichai. Rigid frictionless indentation on elastic half space with influence of surface stresses. *International Journal of Engineering Science*, 71:15–35, 2013.

[160] H. J. Qi, K. Joyce, and M. C. Boyce. Durometer hardness and the stress-strain behavior of

Bibliography

elastomeric materials. *Rubber Chemistry and Technology*, 76(2):419–435, 2003.

[161] Wen Chun Yeh, Pai Chi Li, Yung Ming Jeng, Hey Chi Hsu, Po Ling Kuo, Meng Lin Li, Pei Ming Yang, and Huang Lee Po. Elastic modulus measurements of human liver and correlation with pathology. *Ultrasound in Medicine and Biology*, 28(4):467–474, 2002.

[162] Masahiko Bessho, Isao Ohnishi, Takuya Matsumoto, Satoru Ohashi, Juntaro Mat- suyama, Kenji Tobita, Masako Kaneko, and Kozo Nakamura. Prediction of proximal femur strength using a CT-based nonlinear finite element method: Differences in predicted fracture load and site with changing load and boundary conditions. *Bone*, 45(2):226– 231, 2009.

[163] Kaifeng Liu, Mark R. VanLandingham, and Timothy C. Ovaert. Mechanical characterization of soft viscoelastic gels via indentation and optimization-based inverse finite element analysis. *Journal of the Mechanical Behavior of Biomedical Materials*, 2(4):355–363, 2009.

[164] K D Costa and F C Yin. Analysis of indentation: implications for measuring mechanical properties with atomic force microscopy. *Journal of biomechanical engineering*, 121(5):462–471, 1999.

[165] Martin Kroon. A numerical framework for material characterization of inhomogeneous hyperelastic membranes by inverse analysis. *Journal of Computational and Applied Mathematics*, 234(2):563–578, 2010.

[166] J Hadamard. Lectures on Cauchy's problem in linear partial differential equations. *Physiology*, page 334, 1923.

Curriculum Vitae

Curriculum Vitae

Name: **Md. Mansur ul Mulk**

Post-secondary   University of Western Ontario
Education and   London, Ontario, Canada
Degrees: 2013 – 2020 Ph.D. Candidate

                    The University of Western Ontario
                    London, Ontario, Canada
                    2011 – 2012 M.Eng. (Chemical and Biochemical Engineering)

                    The University of Western Ontario
                    London, Ontario, Canada
                    2009 – 2011 B.Sc. (Medical Biophysics, Honors Specialization)

                    Jahangirnagar University
                     Savar, Dhaka, Bangladesh
                    1988 – 1990 M.Sc. (Physics).

                    Jahangirnagar University
                    Savar, Dhaka, Bangladesh
                    1984 – 1988 B.Sc.(Physics).

Honours and Western Graduate Scholarship
Awards: 2013–2016

Related Work   Teaching Assistant
Experience   The University of Western Ontario
                    2013–2016

Related Work   Professor
Experience   Mohawk College
                    2019-Present